

AFRL-ML-WP-TR-2005-4094

**TECHNICAL OPERATIONS
SUPPORT – I**

**Delivery Order 0033: Structural Monitoring
with Piezoelectric Wafer Active Sensors**



**Victor Giurgiutiu, JingJing Bao, Joel Bost, Adrian Cuc,
James Doane, Christopher Jenkins, Bin Lin, Buli Xu, and
Lingyu Yu**

**University of South Carolina
Department of Mechanical Engineering
Laboratory for Active Materials and Smart Structures (LAMSS)
300 S. Main Street
Columbia, SC 29208**

JULY 2004

Final Report for 25 April 2003 – 24 July 2004

Approved for public release; distribution is unlimited.

STINFO FINAL REPORT

**MATERIALS AND MANUFACTURING DIRECTORATE
AIR FORCE RESEARCH LABORATORY
AIR FORCE MATERIEL COMMAND
WRIGHT-PATTERSON AIR FORCE BASE, OH 45433-7750**

NOTICE

Using Government drawings, specifications, or other data included in this document for any purpose other than Government procurement does not in any way obligate the U.S. Government. The fact that the Government formulated or supplied the drawings, specifications, or other data does not license the holder or any other person or corporation; or convey any rights or permission to manufacture, use, or sell any patented invention that may relate to them.

This report was cleared for public release by the Air Force Research Laboratory Wright Site Public Affairs Office (AFRL/WS) and is releasable to the National Technical Information Service (NTIS). It will be available to the general public, including foreign nationals.

THIS TECHNICAL REPORT IS APPROVED FOR PUBLICATION.

/s/

WILLIAM FREEMANTLE, Lt. USAF
Project Engineer
Nondestructive Evaluation Branch
Metals, Ceramics & NDE Division

/s/

JAMES C. MALAS, Chief
Branch Chief
Nondestructive Evaluation Branch
Metals, Ceramics & NDE Division

/s/

GERALD J. PETRAK
Assistant Chief
Metals, Ceramics & NDE Division
Materials & Manufacturing Directorate

This report is published in the interest of scientific and technical information exchange and its publication does not constitute approval or disapproval of its ideas or findings.

| REPORT DOCUMENTATION PAGE | | | | Form Approved OMB No. 0704-0188 | |
|---|-----------------------------|------------------------------|---------------------------------------|---|--|
| <p>The public reporting burden for this collection of information is estimated to average 1 hour per response, including the time for reviewing instructions, searching existing data sources, gathering and maintaining the data needed, and completing and reviewing the collection of information. Send comments regarding this burden estimate or any other aspect of this collection of information, including suggestions for reducing this burden, to Department of Defense, Washington Headquarters Services, Directorate for Information Operations and Reports (0704-0188), 1215 Jefferson Davis Highway, Suite 1204, Arlington, VA 22202-4302. Respondents should be aware that notwithstanding any other provision of law, no person shall be subject to any penalty for failing to comply with a collection of information if it does not display a currently valid OMB control number. PLEASE DO NOT RETURN YOUR FORM TO THE ABOVE ADDRESS.</p> | | | | | |
| 1. REPORT DATE (DD-MM-YY) July 2004 | | 2. REPORT TYPE Final | | 3. DATES COVERED (From - To) 04/25/2003 – 07/24/2004 | |
| 4. TITLE AND SUBTITLE TECHNICAL OPERATIONS SUPPORT – I Delivery Order 0033: Structural Monitoring with Piezoelectric Wafer Active Sensors | | | | 5a. CONTRACT NUMBER F33615-01-D-5801-0033 | |
| | | | | 5b. GRANT NUMBER | |
| | | | | 5c. PROGRAM ELEMENT NUMBER 63112F | |
| 6. AUTHOR(S) Victor Giurgiutiu, JingJing Bao, Joel Bost, Adrian Cuc, James Doane, Christopher Jenkins, Bin Lin, Buli Xu, and Lingyu Yu | | | | 5d. PROJECT NUMBER 4349 | |
| | | | | 5e. TASK NUMBER L0 | |
| | | | | 5f. WORK UNIT NUMBER T2 | |
| 7. PERFORMING ORGANIZATION NAME(S) AND ADDRESS(ES) University of South Carolina Department of Mechanical Engineering Laboratory for Active Materials and Smart Structures (LAMSS) 300 S. Main Street Columbia, SC 29208 | | | | 8. PERFORMING ORGANIZATION REPORT NUMBER USC-ME-LAMSS-2003-101 | |
| 9. SPONSORING/MONITORING AGENCY NAME(S) AND ADDRESS(ES) Materials and Manufacturing Directorate Air Force Research Laboratory Air Force Materiel Command Wright-Patterson AFB, OH 45433-7750 | | | | 10. SPONSORING/MONITORING AGENCY ACRONYM(S) AFRL/MLLP | |
| | | | | 11. SPONSORING/MONITORING AGENCY REPORT NUMBER(S) AFRL-ML-WP-TR-2005-4094 | |
| 12. DISTRIBUTION/AVAILABILITY STATEMENT Approved for public release; distribution is unlimited. | | | | | |
| 13. SUPPLEMENTARY NOTES Report contains color. | | | | | |
| 14. ABSTRACT <p>The use of piezoelectric wafer active sensor (PWAS) for structural health monitoring (SHM) has developed into a promising tool for real-time structural damage assessment. The 1-year research work described in this report addresses the following issues: (i) PWAS durability and survivability; (ii) optimum PWAS design; (iii) steering beam large-area coverage (embedded ultrasonic structural radar – EUSR); and (iv) probability of detection (POD) with PWAS probes (an initial investigation).</p> <p>The durability and survivability of the PWAS transducers has been confirmed under various environmental exposures for the duration covered in this one-year effort. These results give confidence in this new technology for installation on realistic structures. The report presents analytical methods and experimental results that can be successfully used in the design of active SHM systems. The EUSR steering beam PWAS phased-arrays method has been refined to increase its power of detection for various structural defects. It has been also proved that EUSR performance is not affected by typical structural curvature. The initial PWAS POD investigation has indicated that crack as small as 1.57 mm can be detected and imaged relatively easily. Overall, the results confirm that PWAS transducers are a technology with good potential for implementation in active SHM systems.</p> | | | | | |
| 15. SUBJECT TERMS Structural health monitoring, piezoelectric, piezoelectric wafer active sensor, PWAS, Lamb waves, E/M impedance, defects, NDE | | | | | |
| 16. SECURITY CLASSIFICATION OF: | | | 17. LIMITATION OF ABSTRACT: SAR | 18. NUMBER OF PAGES 84 | 19a. NAME OF RESPONSIBLE PERSON (Monitor) Lt. William Freemantle 19b. TELEPHONE NUMBER (Include Area Code) (937) 255-2229 |
| a. REPORT Unclassified | b. ABSTRACT Unclassified | c. THIS PAGE Unclassified | | | |

TABLE OF CONTENTS

| | |
|---|-----------|
| 1. LIST OF FIGURES AND TABLES | 1 |
| 2. SUMMARY | 5 |
| 3. INTRODUCTION | 5 |
| 4. TASK 1: PWAS DURABILITY AND SURVIVABILITY | 6 |
| 4.1. SUBTASK 1.1 – OVEN TEST | 6 |
| 4.1.1. <i>Methods, Assumptions, and Procedures</i> | 6 |
| 4.1.2. <i>Results and Discussions</i> | 8 |
| 4.2. SUBTASK 1.2 – OUTDOORS TEST | 9 |
| 4.2.1. <i>Methods, Assumptions, and Procedures</i> | 9 |
| 4.2.2. <i>Specimens and Equipments</i> | 9 |
| 4.2.3. <i>Results and Discussions</i> | 11 |
| 4.3. SUBTASK 1.3 – SUBMERSION TEST | 13 |
| 4.3.1. <i>Methods, Assumptions, and Procedures</i> | 13 |
| 4.3.2. <i>Results and Discussions</i> | 13 |
| 4.4. SUBTASK 1.4 – TENSILE TESTS | 14 |
| 4.4.1. <i>Methods, Assumptions, and Procedures</i> | 14 |
| 4.4.2. <i>Results and Discussions</i> | 15 |
| 4.5. TASK 1 – CONCLUSIONS | 21 |
| 5. TASK 2: OPTIMUM PWAS DESIGN | 22 |
| 5.1. SUBTASK 2.1 –DEVELOPMENT OF SOFTWARE PACKAGES FOR LAMB WAVE SIMULATION IN VARIOUS MATERIAL SYSTEMS | 23 |
| 5.1.1. <i>Methods, Assumptions, and Procedures</i> | 23 |
| 5.1.2. <i>Results and Discussions</i> | 26 |
| 5.2. SUBTASK 2.2 LAMB-WAVE MODES TUNING WITH PWAS TRANSDUCERS | 26 |
| 5.2.1. <i>Methods, Assumptions, and Procedures</i> | 26 |
| 5.2.2. <i>Results and Discussions</i> | 28 |
| 5.3. SUBTASK 2.3 –MODELING AND DESIGN FOR RECIPROCITY OF PWAS LAMB WAVE TRANSMISSION-RECEPTION | 32 |
| 5.3.1. <i>Methods, Assumptions, and Procedures</i> | 32 |
| 5.3.2. <i>Results and Discussions</i> | 34 |
| 5.4. SUBTASK 2.4 – MODELING AND SIMULATION FOR DETECTION OF CORROSION USING LAMB WAVES | 38 |
| 5.4.1. <i>Methods, Assumptions, and Procedures</i> | 38 |
| 5.4.2. <i>Results and Discussions</i> | 39 |
| 5.5. TASK 2 - CONCLUSIONS | 41 |
| 6. TASK 3: STEERING-BEAM LARGE AREA COVERAGE | 43 |
| 6.1. SUBTASK 3.1 – EUSR WITH CURVATURE | 43 |
| 6.1.1. <i>Methods, Assumptions, and Procedures</i> | 43 |
| 6.1.2. <i>Results and Discussions</i> | 44 |
| 6.2. SUBTASK 3.2 – THE EFFECTS OF CRACK ORIENTATION AND MULTIPLE TARGETS ON EUSR | 54 |
| 6.2.1. <i>Methods, Assumptions, and Procedures</i> | 54 |
| 6.2.2. <i>Results and Discussions</i> | 59 |
| 6.3. SUBTASK 3.3 – AUTOMATIC SIGNAL ACQUISITION | 61 |
| 6.3.1. <i>Methods, Assumptions, and Procedures</i> | 61 |
| 6.4. TASK 3 – CONCLUSIONS | 62 |
| 7. TASK 4: PROBABILITY OF DETECTION (POD) WITH PWAS PROBES (AN INITIAL ANALYSIS) | 63 |
| 7.1. METHODS, ASSUMPTIONS, AND PROCEDURES | 63 |
| 7.1.1. <i>Planning the POD Experiment</i> | 63 |
| 7.1.2. <i>PWAS POD Experimental Planning</i> | 65 |
| 7.2. RESULTS AND DISCUSSIONS | 66 |
| 7.3. TASK 4 – CONCLUSIONS | 67 |
| 8. REFERENCES | 68 |
| 9. LIST OF SYMBOLS, ABBREVIATIONS, AND ACRONYMS | 69 |

1. LIST OF FIGURES AND TABLES

| | | |
|-----------|--|----|
| Figure 1 | (a) Blue M Electric Oven (Max Temperature: 704°C), (b) HP 4194 Impedance Analyzer..... | 7 |
| Figure 2 | Specimens, (a) Schematic free PWAS and PWAS attached to metallic plate specimen, (b) Free PWAS and PWAS attached to metallic plate specimen..... | 7 |
| Figure 3 | Temperature cycles graph..... | 8 |
| Figure 4 | Comparison of PWAS #01 with polyurethane coating spectra. After a 1200-cycle oven exposure, no significant change is recorded: (a) narrow-band spectrum showing only the first two resonance frequencies; (b) broadband spectrum showing several resonance frequencies..... | 8 |
| Figure 5 | Comparison of PWAS #02 with polyurethane coating spectra. After a 1200-cycle oven exposure, no significant change is recorded: (a) narrow-band spectrum showing only the first four resonance frequencies; (b) broadband spectrum showing several resonance frequencies..... | 9 |
| Figure 6 | Fixtures for testing the PWAS specimens: (a) specimens in a cage placed outdoors; (b) specimens stand that fits inside the cage..... | 10 |
| Figure 7 | M-LINE Three Conductor Cables | 11 |
| Figure 8 | Samples after 20-weeks outdoors. (a) Free PWAS, (b) Bonded PWAS..... | 11 |
| Figure 9 | Comparison of PWAS #43 with polyurethane coating spectra. After a 20-week outdoor exposure no significant change is recorded: (a) narrow-band spectrum showing only the first two resonance frequencies; (b) broadband spectrum showing several resonance frequencies..... | 11 |
| Figure 10 | Comparison of PWAS #23 with polyurethane coating spectra. After a 20-week outdoor exposure no significant change is recorded: narrow-band spectrum showing only the first four resonance frequencies; | 12 |
| Figure 11 | Weather is recorded from NOAA website, plots from these data: (a) Temperature, showing high, low and average temperature of days from initial measurement; (b) Rainfall, showing rainfall of days from initial measurement..... | 12 |
| Figure 12 | Submersion test samples. | 13 |
| Figure 13 | PWAS impedance spectra collected over 85 days of submergence in various fluids associated with Air Force usage..... | 13 |
| Figure 14 | Specimen Mounted in the MTS 810 Material Testing System..... | 14 |
| Figure 15 | Tensile Specimen Stress-Strain Curve | 14 |
| Figure 16 | Baseline Impedance for PWAS 01 | 15 |
| Figure 17 | Impedance Signature Comparisons for PWAS 01 for 0 $\mu\epsilon$ to 3000 $\mu\epsilon$ | 16 |
| Figure 18 | Impedance Signature Comparisons for PWAS 01 for 3000 $\mu\epsilon$ to 5000 $\mu\epsilon$ | 16 |
| Figure 19 | Comparison of Initial Baseline Impedance to Final Unloaded Impedance for PWAS 01..... | 17 |
| Figure 20 | Baseline Impedance for PWAS 02 | 17 |
| Figure 21 | Impedance Signature Comparisons for PWAS 02 for 0 $\mu\epsilon$ to 3000 $\mu\epsilon$ | 18 |
| Figure 22 | Impedance Signature Comparisons for PWAS 02 for 3000 $\mu\epsilon$ to 6000 $\mu\epsilon$ | 18 |
| Figure 23 | Impedance Signature Comparisons for PWAS 02 for 6000 $\mu\epsilon$ to 7200 $\mu\epsilon$ | 19 |

| | |
|--|----|
| Figure 24 Comparison of Initial Baseline to Unloaded Impedance up to 4000 $\mu\epsilon$ for PWAS 02 | 19 |
| Figure 25 Comparison of Unloaded Impedance from 4000 up to 7000 $\mu\epsilon$ for PWAS 02..... | 20 |
| Figure 26 Imaginary Impedance Comparisons for PWAS 02 for 0 $\mu\epsilon$ to 4000 $\mu\epsilon$ | 20 |
| Figure 27 Imaginary Impedance Comparisons for PWAS 02 for 4000 $\mu\epsilon$ to 7000 $\mu\epsilon$ | 21 |
| Figure 28 PWAS interaction with Lamb modes: (a) symmetric Lamb mode S_0 ; (b) anti-symmetric Lamb mode A_0 | 22 |
| Figure 29 – Lamb mode wave speed, mode shape, and stress distribution simulation program (MODE_SHAPE_V2)..... | 23 |
| Figure 30 – (Lamb wave speed and group velocity simulation program (WAVESCOPE)..... | 24 |
| Figure 31 – Software simulation programs for signal analysis using short time Fourier transform (STFT) | 25 |
| Figure 32 – Software simulation programs for signal analysis using wavelets (WAVELETS). | 25 |
| Figure 33 Shear layer interaction between the PWAS and the structure: (a) micrograph; (b) modeling | 26 |
| Figure 34 Symmetric and antisymmetric loading from a PWAS of width $2a$ mounted on the plate upper surface: (a) symmetric loading and (b) anti-symmetric loading | 28 |
| Figure 35 – (a) Predicted Lamb-wave response a 1-mm aluminum plate under a 7-mm PWAS excitation: (a) strain response; (b) displacement response..... | 32 |
| Figure 36 – Plots to the modeling (a) and experiment (b). | 33 |
| Figure 37 The instrumentation setup: (a) schematic of the location of the PWAS sensors on the Aluminum plate as well as the equipment necessary to generate and capture the signals; (b) picture of the actual equipment and location of sensors | 33 |
| Figure 38 Excitation signal..... | 34 |
| Figure 39 Transmitted and received S_0 mode Lamb wave: (a) PWAS #1 was used as a transmitter and PWAS #7 was the receiver; (b) PWAS #7 was used as a transmitter and PWAS #1 was the receiver | 35 |
| Figure 40 Transmitted and received S_0 mode Lamb wave: (a) PWAS #8 was used as a transmitter and PWAS #11 was the receiver; (b) PWAS #11 was used as a transmitter and PWAS #8 was the receiver | 35 |
| Figure 41 Transmitted and received S_0 mode Lamb wave: (a) PWAS #1 was used as a transmitter and PWAS #11 was the receiver; (b) PWAS #11 was used as a transmitter and PWAS #1 was the receiver | 36 |
| Figure 42 Transmitted and received A_0 mode Lamb wave: (a) PWAS #1 was used as a transmitter and PWAS #7 was the receiver; (b) PWAS #7 was used as a transmitter and PWAS #1 was the receiver | 36 |
| Figure 43 Transmitted and received A_0 mode Lamb wave: (a) PWAS #8 was used as a transmitter and PWAS #11 was the receiver; (b) PWAS #11 was used as a transmitter and PWAS #8 was the receiver | 37 |
| Figure 44 Transmitted and received A_0 mode Lamb wave: (a) PWAS #1 was used as a transmitter and PWAS #11 was the receiver; (b) PWAS #11 was used as a transmitter and PWAS #1 was the receiver | 37 |

| | | |
|-----------|---|----|
| Figure 45 | Dispersion characteristics of A_0 Lamb wave mode in 1-mm 2024-T3 aluminum plate: (a) A_0 wave speed vs. frequency; (b) A_0 wavelength vs. frequency | 38 |
| Figure 46 | Variation of tuned excitation frequency with PWAS diameter for A_0 Lamb wave mode | 38 |
| Figure 47 | Simulation of A_0 mode Lamb wave response at $x = 250\sqrt{2}$ and $500\sqrt{2}$ mm from the PWAS source placed at $x = 0$ mm (3.5-count smoothed tone burst of 31.5 kHz, plate thickness $h = 1$ mm) | 40 |
| Figure 48 | Simulation of A_0 Lamb wave mode response at $250\sqrt{2}$ mm from the PWAS source for two plate thickness values: (a) $h = 1$ mm; (b) $h_{75\%} = 0.75$ mm (3.5-count smoothed tone burst of 31.5 kHz) | 40 |
| Figure 49 | Cross plot between the pristine and corroded signals: (a) 0.5% total material loss; (b) 1% total material loss | 41 |
| Figure 50 | Curvature of the specimen | 43 |
| Figure 51 | Two types of curvature: a) direction 1, parallel to the PWAS array; b) direction 2, perpendicular to the PWAS array. | 44 |
| Figure 52 | Experiment with 0 curvature | 45 |
| Figure 53 | EUSR analysis for 0 curvature | 45 |
| Figure 54 | Experiment with 5mm curvature at direction 1 | 46 |
| Figure 55 | EUSR analysis for 5mm curvature at direction 1 | 46 |
| Figure 56 | Experiment with 10mm curvature at direction 1 | 47 |
| Figure 57 | EUSR analysis for 10mm curvature at direction 1 | 47 |
| Figure 58 | Experiment with 15mm curvature at direction 1 | 48 |
| Figure 59 | EUSR analysis for 15mm curvature at direction 1 | 48 |
| Figure 60 | Experiment with 20mm curvature at direction 1 | 49 |
| Figure 61 | EUSR analysis for 20mm curvature at direction 1 | 49 |
| Figure 62 | Experiment with 5mm curvature at direction 2 | 50 |
| Figure 63 | EUSR analysis for 5mm curvature at direction 2 | 50 |
| Figure 64 | Experiment with 10mm curvature at direction 2 | 51 |
| Figure 65 | EUSR analysis for 10mm curvature at direction 2 | 51 |
| Figure 66 | Experiment with 15mm curvature at direction 2 | 52 |
| Figure 67 | EUSR analysis for 15mm curvature at direction 2 | 52 |
| Figure 68 | Experiment with 20mm curvature at direction 2 | 53 |
| Figure 69 | EUSR analysis for 20mm curvature at direction 2 | 53 |
| Figure 70 | the transmitted signal and the received signal | 55 |
| Figure 71 | EUSR experiment with the 8 element PWAS array: (a) specimen layout; (b) experiment setup | 56 |
| Figure 72 | single broadside crack detection with previous EUSR: (a) schematic; (b) EUSR GUI mapped image | 56 |

| | |
|---|----|
| Figure 73 single offside crack detection with previous EUSR: (a) schematic; (b) EUSR GUI mapped image..... | 57 |
| Figure 74 a tone-burst signal and its envelope extracted by using Hilbert transform..... | 58 |
| Figure 75 – single crack detection with the improved EUSR: (a) broadside crack detection; (b) offside crack detection | 58 |
| Figure 76 – data flow of the damage detection by using the improved EUSR algorithm | 59 |
| Figure 77 – the broadside crack having 30° slope: (a) schematic; (b) EUSR ‘GUI mapped image | 59 |
| Figure 78 – the two symmetrical offside cracks at 63° and 137°, respectively: (a) schematic; (b) EUSR GUI mapped image..... | 60 |
| Figure 79 – three aligned cracks: (a) schematic of the horizontal broadside crack; (b) schematic of the vertical broadside crack | 60 |
| Figure 80 Experimental setup..... | 61 |
| Figure 81 Autoswitch device for automated signal acquisition in the steering beam experiments: (a) experimental setup; (b) graphical user interface of the controlling LabVIEW program | 62 |
| Figure 82 Typical POD Curves (Grills, 2001)..... | 63 |
| Figure 83 Damage location;(a) Phase one, damage is located perpendicular to the PWAS array; (b) Phase two, damage is located at an angle | 64 |
| Figure 84 Experimental setup for the POD experiment | 65 |
| Figure 85 Tools for the PWAS POD experiment: (a) aluminum plate with a PWAS array and a pin-hole damage of increasing size; (b) set of small drill bits in the size range 0.5mm, 1mm, 1.57mm and 2mm..... | 66 |
| Figure 86 – pin-holes: (a) schematic; (b) EUSR GUI mapped image of the minimum detectable pin-hole with 1.57mm diameter; (c) EUSR GUI mapped image of pin-hole with 2mm diameter | 66 |
| Table 1 Free PWAS | 10 |
| Table 2 Circular plate specimen with PWAS | 10 |
| Table 3 Location of PWAS sensors on the Aluminum plate | 34 |

2. SUMMARY

This report consists of four unique tasks that serve to evaluate the piezoelectric wafer active sensors' (PWAS) performance, durability, design, and reliability. Task 1: PWAS Durability and Survivability showed how temperature, weather, liquids, and strain affect the performance of the PWAS. Minimal changes were caused by temperature, weather, and liquids, but it was discovered that large changes in impedance can be caused by strain. Task 2: Optimum PWAS Design uses theoretical model and real tests to design a PWAS layout that will detect cracks and corrosion. MathCAD and MatLAB were used to create models of Lambs in a structure and experiments were done to verify the results. Task 3: Steering-Beam Large Area Coverage examined what affect multiple cracks, crack orientation, and curvature has on PWAS. New techniques like the Hilbert transformation and the autoswitch device helped to improve the scanning and detection methods. The last task, Task 4: Probability of Detection (POD), uses pin holes to test the smallest amount of damage the PWAS can detect which was about 1.57 mm.

3. INTRODUCTION

Structural health monitoring (SHM) is a method of determining the health of a structure from the readings of an array of permanently-attached sensors that are embedded into the structure and monitored over time. SHM can be performed in basically two ways, passive and active. Passive SHM consists of monitoring a number of parameters (loading stress, environment action, performance indicators, acoustic emission from cracks, etc.) and inferring the state of structural health from a structural model. In contrast, active SHM performs proactive interrogation of the structure, detects damage, and determines the state of structural health from the evaluation of damage extend and intensity. Both approaches aim at performing a diagnosis of the structural safety and health, to be followed by a prognosis of the remaining life. Passive SHM uses passive sensors which only “listen” but do not interact with the structure. Therefore, they do not provide direct measurement of the damage presence and intensity. Active SHM uses active sensors that interact with the structure and thus determine the presence or absence of damage. The methods used for active SHM resemble the methods of nondestructive evaluation (NDE), e.g., ultrasonics, eddy currents, etc., only that they are used with embedded sensors. Hence, the active SHM could be seen as “embedded NDE”. One widely used active SHM method employs piezoelectric wafer active sensors (PWAS), which send and receive Lamb waves and determine the presence of cracks, delaminations, disbonds, and corrosions. Due to its similarities to NDE ultrasonics, this approach is also known as “embedded ultrasonics”.

Using Lamb waves (guided waves) is much more efficient for inspecting thin-wall structures than using conventional pressure waves. Lamb waves remain guided between two parallel free surfaces, such as the upper and lower surfaces of a plate or shell and can propagate along the mid-surface of thin-wall plates and shallow shells. They can travel at relatively large distances with very little amplitude loss and offer the advantage of large-area coverage with a minimum of installed sensors. In Lamb-waves applications, PWAS couple their in-plane motion, excited through the piezoelectric effect, with the Lamb-waves particle motion on the material surface. Thus, PWAS can be both exciters and detectors of elastic Lamb waves traveling in the material. Damage is detected if the exciter and detector signals are different.

The electromechanical (E/M) impedance method is an embedded ultrasonic method that is emerging as an effective and powerful technique for SHM. The impedance method provides several advantages over traditional NDE approaches. Through PWAS permanently attached to the structure, the E/M impedance method is able to measure directly the high-frequency local impedance spectrum of the structure. Because the high-frequency local impedance spectrum is much more sensitive to incipient damage than the low-frequency global impedance, the E/M impedance method is better suited for applications in structural health monitoring than other more conventional methods. The PWAS health monitoring technique has been successfully applied to various structures ranging from aerospace to civil structures.

4. TASK 1: PWAS DURABILITY AND SURVIVABILITY

The purpose of this task is to explore the durability and survivability issues associated with various environmental conditions on PWAS for impedance-based structural health monitoring. Our approach consists of several stages. First, we put the PWAS into oven to determine how it behaves in the temperature range associated with operational usage. Free PWAS and bonded PWAS were placed in an oven and exposed to a certain temperature and a heating cycle. Second, we put the free PWAS and bonded PWAS with different adhesives and coatings in the outdoor environment to determine how it behaves in different weather conditions (sun, rain, etc.). Third, we determine how PWAS behaves when exposed to water and various maintenance fluids (hydraulic fluids and lubrication oils). Forth, determine how the piezoelectric material behaves when exposed to tension stresses associated with Air Force usage.

Task Overview

- Environmental Conditions Tests
 - Subtask 1.1 – Oven Test
 - Heat cycling
 - Subtask 1.2 – Outdoor Test
 - Real World Climate and Environmental Changes
 - Subtask 1.3 – Submersion Test
 - Distilled water
 - Saline water
 - Hydraulic fluid MIL-PRF- 83282 Synthetic hydrocarbon
 - Hydraulic fluid MIL-PRF- 87257 Synthetic hydrocarbon
 - Hydraulic fluid MIL-PRF- 5606 Mineral
 - Aircraft cube oil MIL-PRF-7808L Grade 3 Turbine engine synthetic
 - Kerosene Hydraulic Fluid
- Physical Properties Tests
 - Subtask 1.4 – Tensile Test

4.1. *SUBTASK 1.1 – OVEN TEST*

4.1.1. **Methods, Assumptions, and Procedures**

Oven test is a part of tests of durability and Survivability of Piezoelectric Wafer Active Sensor (PWAS). The objective of this test is to determine how the piezoelectric material behaves in the temperature range associated with SHM usage. The test consist of exposing PWAS in an oven to the given temperature range for the specified period of time. The functionality of the PWAS has been tested before and after temperature exposure via impedance spectra measured using the Hewlett Packard 4194 Electromechanical Impedance Analyzer.

The impedance of free PWAS has been measured on the following frequency ranges: R1-R2: 100-900 kHz (in plane vibrations narrow), R1-R#: 100-3100 kHz (in plane vibrations wide), and T1: 10.5-12.5MHz (thickness vibrations). Additionally, PWAS bonded to metallic plate will be tested on the range P1-P6: 1-40 kHz (plate flexural modes).

Equipment/Apparatus and Specimens

The major equipment that was used was the Blue M Electric Oven and Hewlett Packard 4194 Electro-Mechanical Impedance Analyzer Figure 1.

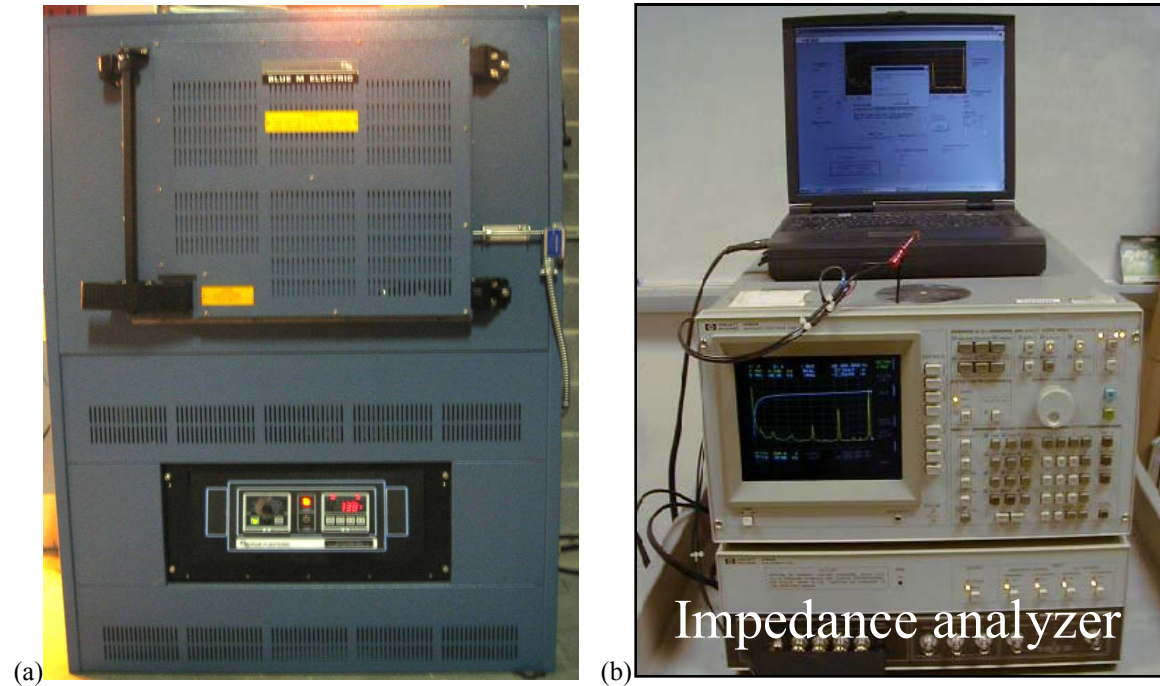


Figure 1 (a) Blue M Electric Oven (Max Temperature: 704°C), (b) HP 4194 Impedance Analyzer

Two types of specimens have been used (Figure 2). The bond adhesive is M Bond 200. The connection wire is AWG 38. The diameter of wire is 0.1mm.

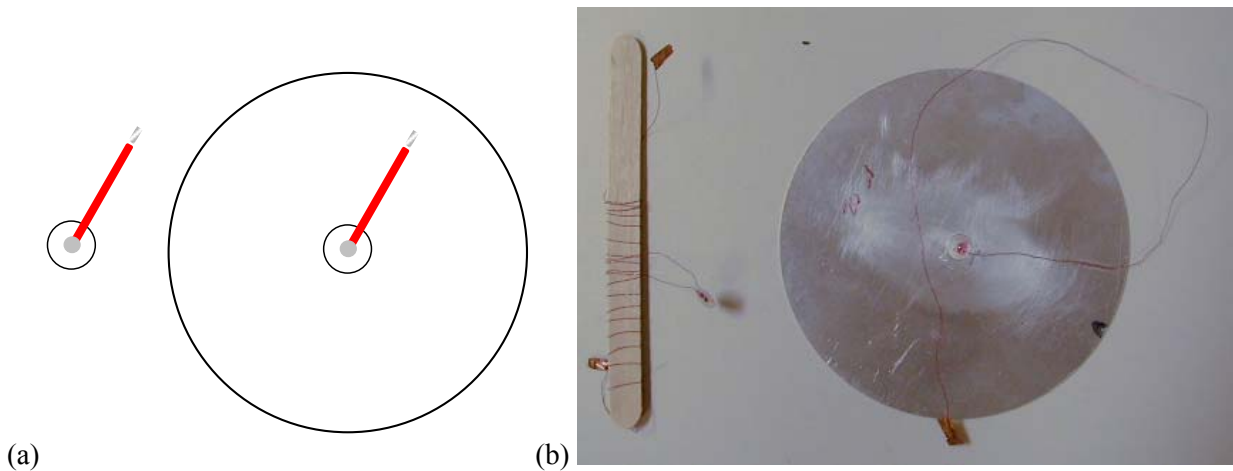


Figure 2 Specimens, (a) Schematic free PWAS and PWAS attached to metallic plate specimen, (b) Free PWAS and PWAS attached to metallic plate specimen

Heating Procedure

The heating tests consist of two parts: the first part is placing PWAS in an oven and exposing them to 175F for an hour and cool down to room temperature five times. The other part is placing PWAS in an oven and exposing them to an automatic cycling temperature for a given amount of time.

One Cycle consists of two segments. Segment 1: Rise from 100F to 175F for an hour and last for 5 minutes in 175F. Segment 2: Fall from 175F to 100F for an hour and last for 5 minutes in 100F (Figure 3).

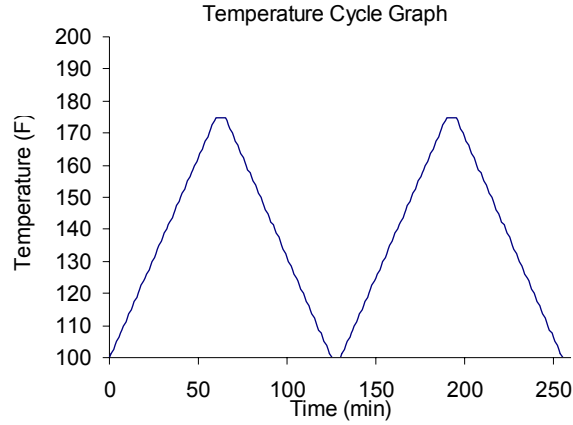


Figure 3 Temperature cycles graph

4.1.2. Results and Discussions

4.1.2.1. Free PWAS

The graphs below show the behavior of the free PWAS #1. After a 1200-cycle oven exposure, no significant change was observed in the PWAS spectrum (Figure 4).

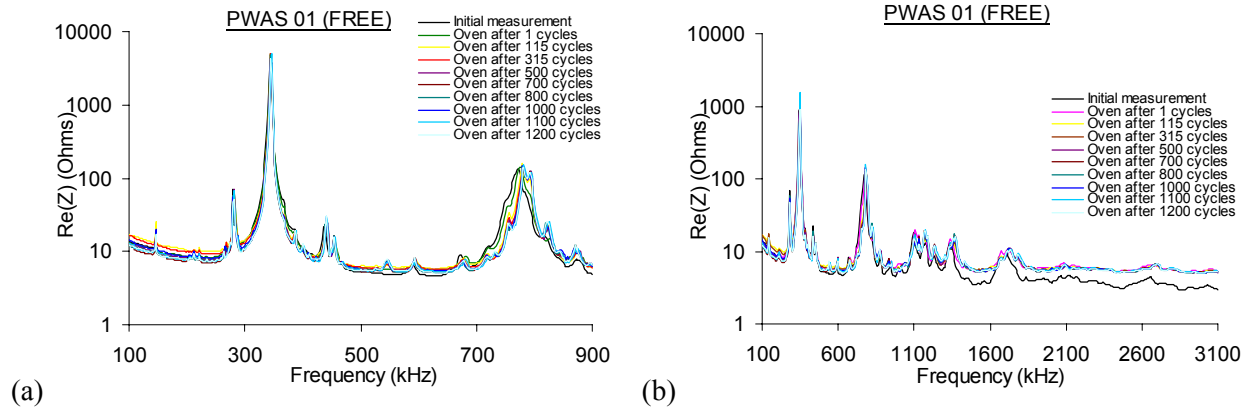


Figure 4 Comparison of PWAS #01 with polyurethane coating spectra. After a 1200-cycle oven exposure, no significant change is recorded: (a) narrow-band spectrum showing only the first two resonance frequencies; (b) broadband spectrum showing several resonance frequencies

4.1.2.2. Bonded PWAS

The graphs below show the behavior of the bonded PWAS #2. After a 1200-cycle oven exposure, no significant change was observed in the PWAS spectrum (Figure 5).

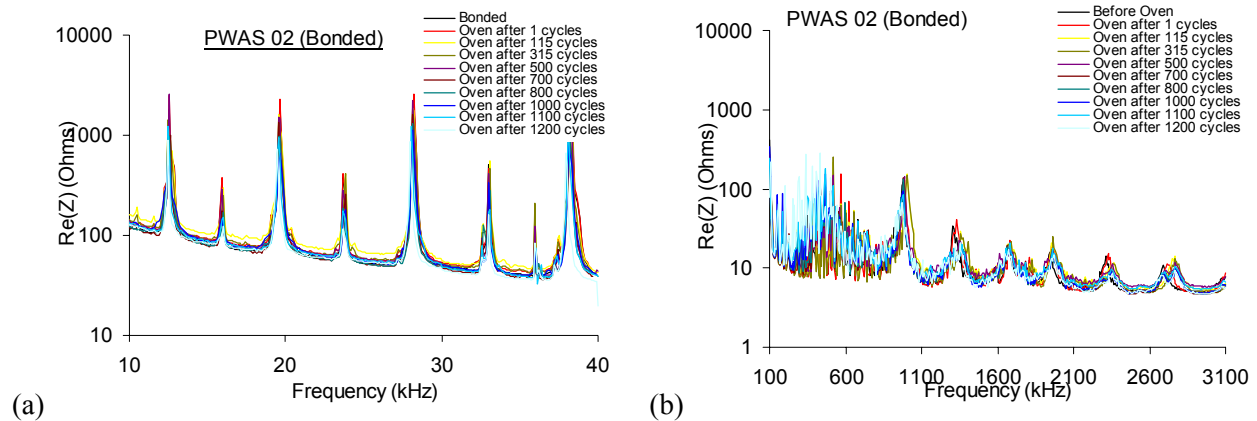


Figure 5 Comparison of PWAS #02 with polyurethane coating spectra. After a 1200-cycle oven exposure, no significant change is recorded: (a) narrow-band spectrum showing only the first four resonance frequencies; (b) broadband spectrum showing several resonance frequencies

4.2. SUBTASK 1.2 – OUTDOORS TEST

4.2.1. Methods, Assumptions, and Procedures

The objective of outdoors test is to determine how the piezoelectric material behaves in the different weather conditions (sun, rain ...) associated with SHM usage. The test consists of placing Piezoelectric Wafer Active Sensors (PWAS) in a cage and exposing them to the outdoor environment in the parking lot. The intended duration of the test is one year. The functionality of the PWAS was tested before and after environment exposure via impedance spectra measured using the Hewlett Packard 4194 Electromechanical Impedance Analyzer. The periodicity of measurements will be one per week.

The impedance of free PWAS will be measured on the following frequency ranges: R1-R2: 100-900 kHz (in plane vibrations narrow), R1-R#:100-3100 kHz (in plane vibrations wide), and T1:10.5-12.5 MHz (thickness vibrations). Additionally, PWAS bonded to metallic plate will be tested on the range P1-P6: 1-40 kHz (plate flexural modes).

4.2.2. Specimens and Equipments

Sixteen specimens were fixed with a stand which was put into a cage (Figure 6). Types and numbers are listed in Table 1 and Table 2. The cage is made by hand and the Hewlett Packard 4194 Electro-Mechanical Impedance Analyzer was used to record the data.

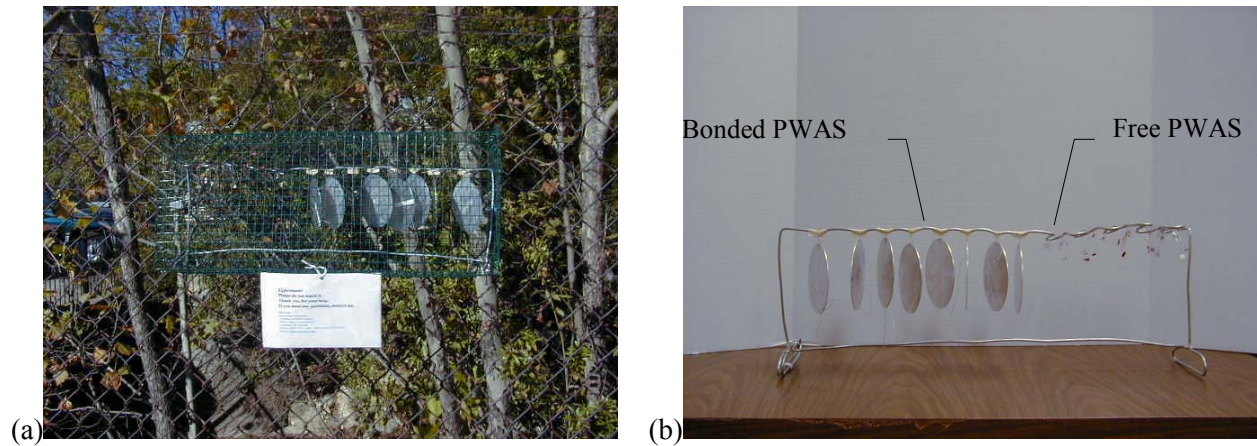


Figure 6 Fixtures for testing the PWAS specimens: (a) specimens in a cage placed outdoors; (b) specimens stand that fits inside the cage

Table 1 Free PWAS

| | | AWG 38 | M-LINE three conductor Cables |
|--------------------|-----------------------|-----------|-------------------------------|
| Protection coating | No coating | 1 (No.40) | 1 (No.42) |
| | M-Coat A-Polyurethane | 1 (No.41) | 1 (No.43) |
| | M-Coat C-Silicon | 1 (No.46) | 1 (No.44) |
| | M-Coat D-Acrylic | 1 (No.48) | 1 (No.45) |

Table 2 Circular plate specimen with PWAS

| | | Adhesive | |
|--------------------|-----------------------|-------------------------------------|---|
| | | M-Bond 200-Cyanoacrylate w/Catalyst | M-Bond AE10-2-part,100% Solids Epoxy System |
| Protection coating | No coating | 1 (No.22) | 1 (No.33) |
| | M-Coat A-Polyurethane | 1 (No.23) | 1 (No.34) |
| | M-Coat C-Silicon | 1 (No.27) | 1 (No.35) |
| | M-Coat D-Acrylic | 1 (No.28) | 1 (No.36) |

Two kinds of connection wire were used - one was AWG 38 and the other was Micro-Measurements Strain Gage Accessories: M-LINE Three Conductor Cables.(Figure 7) Stranded silver-plated copper wire, 3-conductor twisted cable, etched Teflon insulation Small, flexible cable. For use from -452° to +500°F (-269° to +260°C) with color-coded red/white/black. The insulation was treated for bonding.

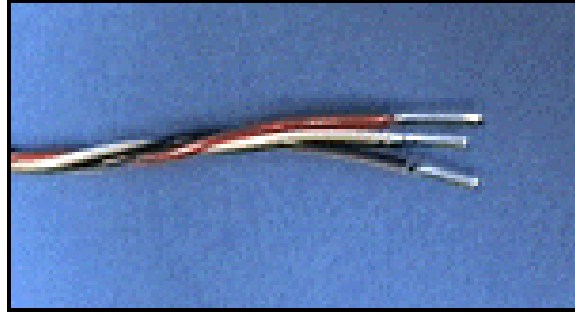


Figure 7 M-LINE Three Conductor Cables

4.2.3. Results and Discussions

There were not any significant changes after 20-week test except there is a lot of dust deposit on the surface of PWAS (Figure 8).

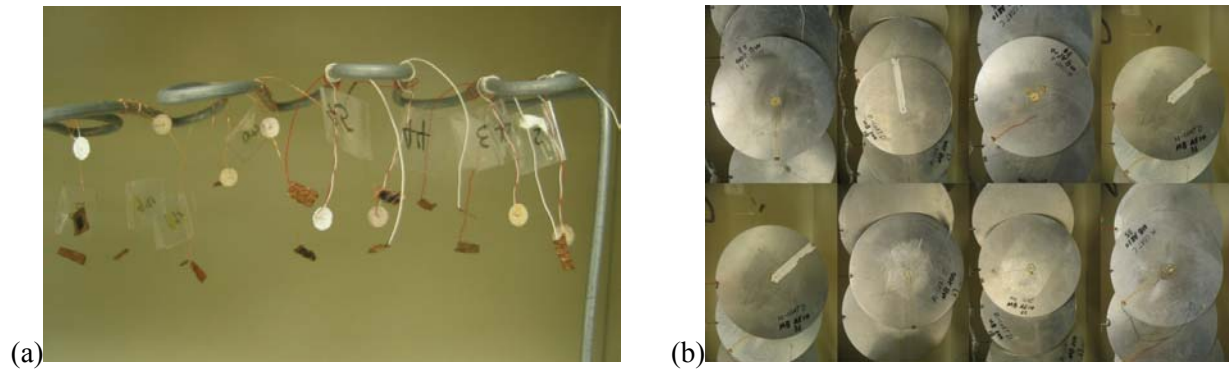


Figure 8 Samples after 20-weeks outdoors. (a) Free PWAS, (b) Bonded PWAS

4.2.3.1. Free PWAS

The graphs below show the behavior of the free PWAS #43. After a 20-week outdoor exposure, no significant change was observed in the PWAS spectrum (Figure 9).

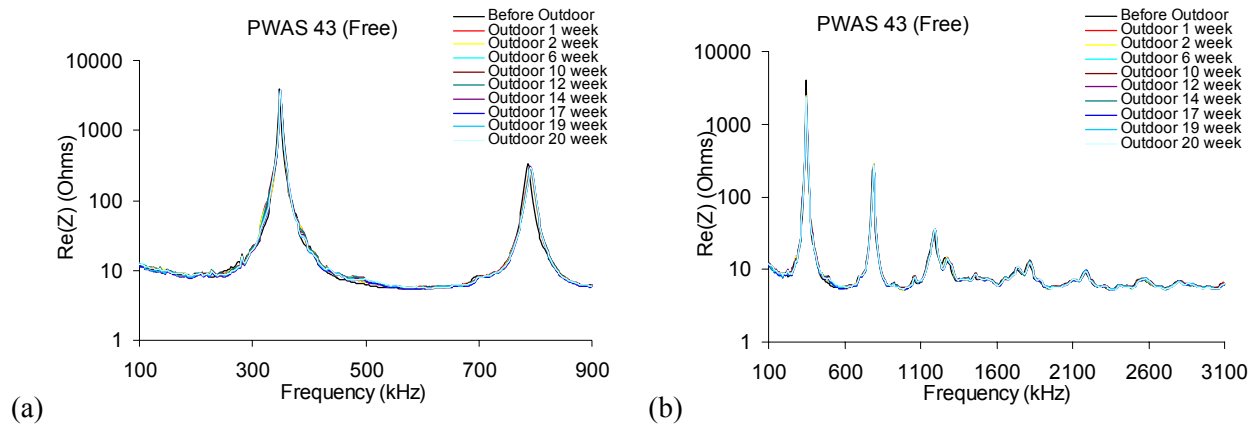


Figure 9 Comparison of PWAS #43 with polyurethane coating spectra. After a 20-week outdoor exposure no significant change is recorded: (a) narrow-band spectrum showing only the first two resonance frequencies; (b) broadband spectrum showing several resonance frequencies

4.2.3.2. Bonded PWAS

The graphs below show the behavior of the PWAS #23 bonded to a circular plate. After a 20-week outdoor exposure, no significant change was observed in the PWAS spectrum (Figure 10).

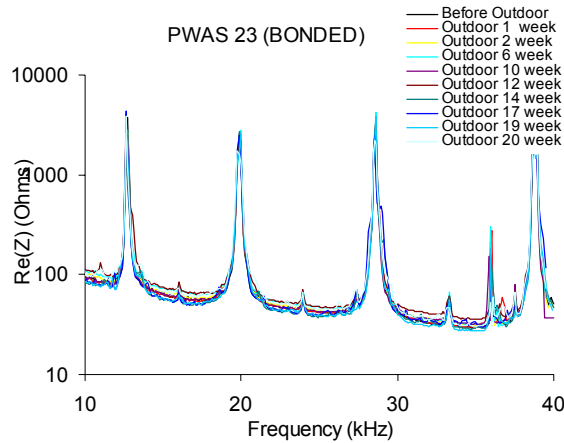


Figure 10 Comparison of PWAS #23 with polyurethane coating spectra. After a 20-week outdoor exposure no significant change is recorded: narrow-band spectrum showing only the first four resonance frequencies;

4.2.3.3. Weather Conditions during Test

The weather conditions during the exposure are recorded from the NOAA website (<http://www.erh.noaa.gov/cae/climate/>). Plots of temperature and rain over the testing period can be extracted from these plots (Figure 11).

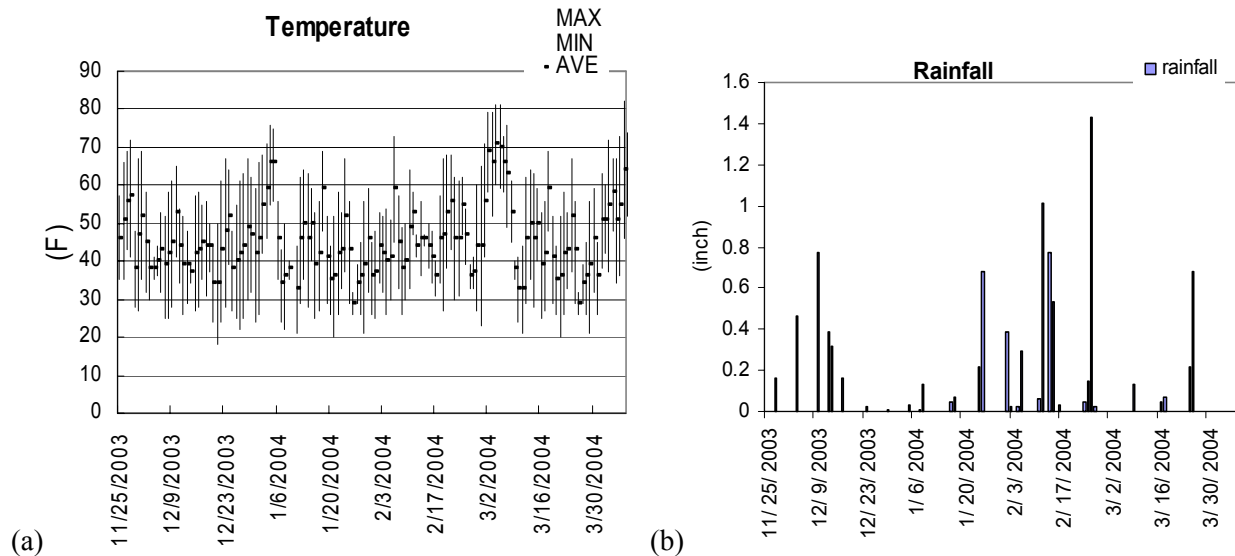


Figure 11 Weather is recorded from NOAA website, plots from these data: (a) Temperature, showing high, low and average temperature of days from initial measurement; (b) Rainfall, showing rainfall of days from initial measurement

4.3. SUBTASK 1.3 – SUBMERSION TEST

4.3.1. Methods, Assumptions, and Procedures

The objective of this test is to determine how the piezoelectric material behaves when exposed to various liquid substances associated with SHM usage. The test consists of placing PWAS in containers and submerging them in the substance for a specified period of time. The PWAS are tested intermittently to monitor effects from submersion in the various fluids (Figure 12). Solvent from left to right: (0) Distilled water; (1) Saline water; (2) Hydraulic fluid MIL-PRF- 83282 Synthetic hydrocarbon ;(3) Hydraulic fluid MIL-PRF- 87257 Synthetic hydrocarbon; (4) Hydraulic fluid MIL-PRF- 5606 Mineral; (5) Aircraft cube oil MIL-PRF-7808L Grade 3 Turbine engine synthetic; (6)Kerosene. Impedance spectra acquired over 85 days for each PWAS are shown in Figure 11, below. Note that the impedance spectra of PWAS 01, submerged in saline water, show more change than the other PWAS spectra. Generally, the spectra for PWAS 01 show the only significant change over 85 days (Figure 13).



Figure 12 Submersion test samples.

4.3.2. Results and Discussions

Figure 13 shows the PWAS impedance spectra collected over 85 days of submergence in various fluids associated with Air Force usage. There are not any significant changes in the plots for the synthetic hydraulic fluid and kerosene. On the saline water plot, there is a significant change on day 85.

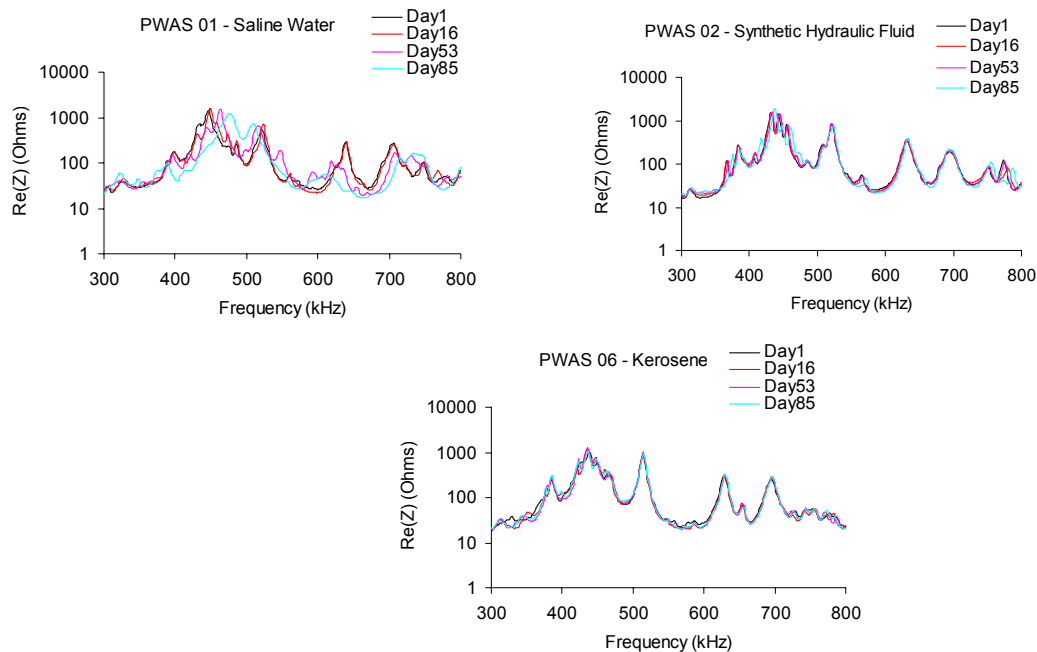


Figure 13 PWAS impedance spectra collected over 85 days of submergence in various fluids associated with Air Force usage

4.4. SUBTASK 1.4 – TENSILE TESTS

4.4.1. Methods, Assumptions, and Procedures

The initial step was to perform a tensile test to failure of one specimen without sensors in order to develop a stress-strain curve for the material. The specimen was placed in a MTS 810 Material Testing System, as shown in Figure 14 and a clip-on displacement transducer was mounted to the specimen (1 mm 2024 AL) to measure the displacement.

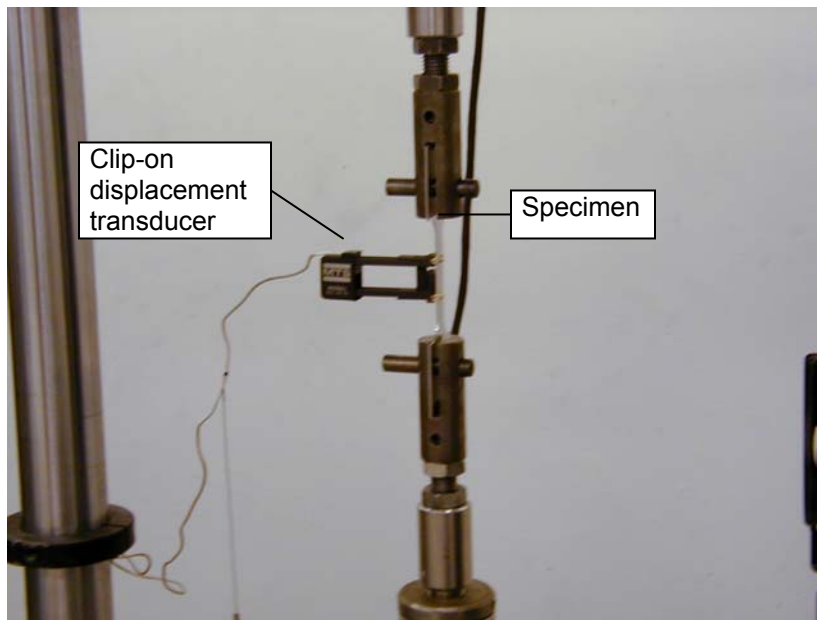


Figure 14 Specimen Mounted in the MTS 810 Material Testing System

The stress-strain curve shown in Figure 15 compares the percent strain to the stress in MPa.

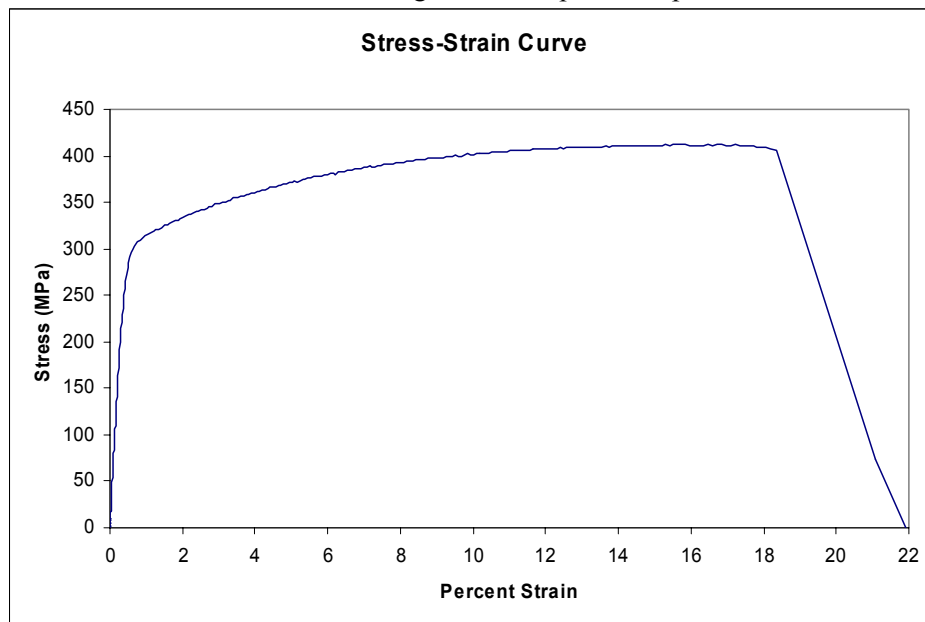


Figure 15 Tensile Specimen Stress-Strain Curve

From the test data the material properties were determined. The Young's Modulus (E) was given by the slope of the straight line region of the graph where stress is proportional to strain, yield stress (Y) was determined by the 0.2% offset method, and the ultimate tensile stress (σ_u) is the maximum stress attained in the engineering stress-strain diagram. These values were determined to be $E \approx 72.5 \text{ GPa}$, $Y \approx 310 \text{ MPa}$ and $\sigma_u \approx 422 \text{ MPa}$.

Two AL specimens were then tested with one PWAS attached to them to determine how the PWAS and the structure interact under stress. PWAS 01 was attached to the first AL specimen and PWAS 02 was attached to the second.

4.4.2. Results and Discussions

4.4.2.1. Experimental Results for PWAS 01

PWAS number 01 was bonded using M-bond 200 cyanoacrylate with catalyst. The specimen was installed into the testing machine without any load applied and the baseline impedance was recorded. The real part of the baseline impedance for the frequency range of 100-200 kHz is shown in Figure 16. The specimen was then loaded in tension until a strain of $200 \mu\epsilon$ was obtained and the new impedance was then recorded. This process was continued at intervals of $200 \mu\epsilon$ until $5000 \mu\epsilon$ was achieved.

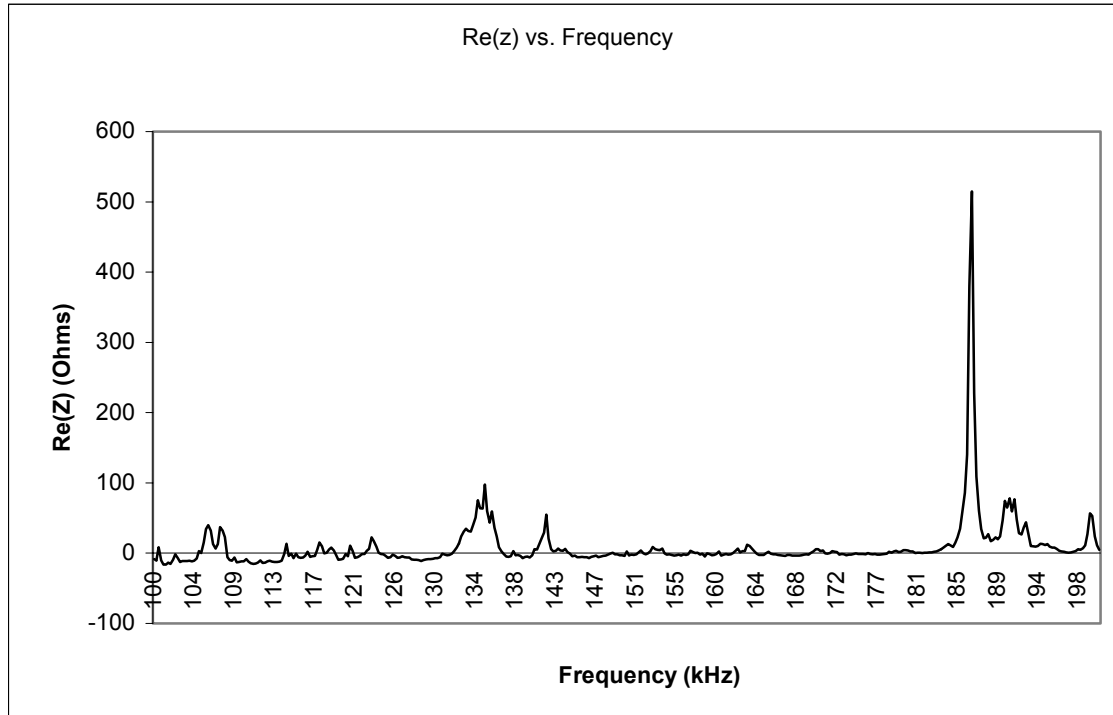


Figure 16 Baseline Impedance for PWAS 01

Figure 17 shows a comparison of the impedance measurements from 0 to $3000 \mu\epsilon$. Minimal changes occurred in that region. Figure 18 shows the comparison from 3000 to $5000 \mu\epsilon$. Significant changes occurred above $3000 \mu\epsilon$. The specimen was then unloaded and the new free impedance was measured and compared to the initial baseline impedance. This comparison is shown in Figure 19. It can be seen that after being loaded to a strain level of $5000 \mu\epsilon$ and then returned to the unloaded state, the impedance signature does not return to its baseline impedance signature.

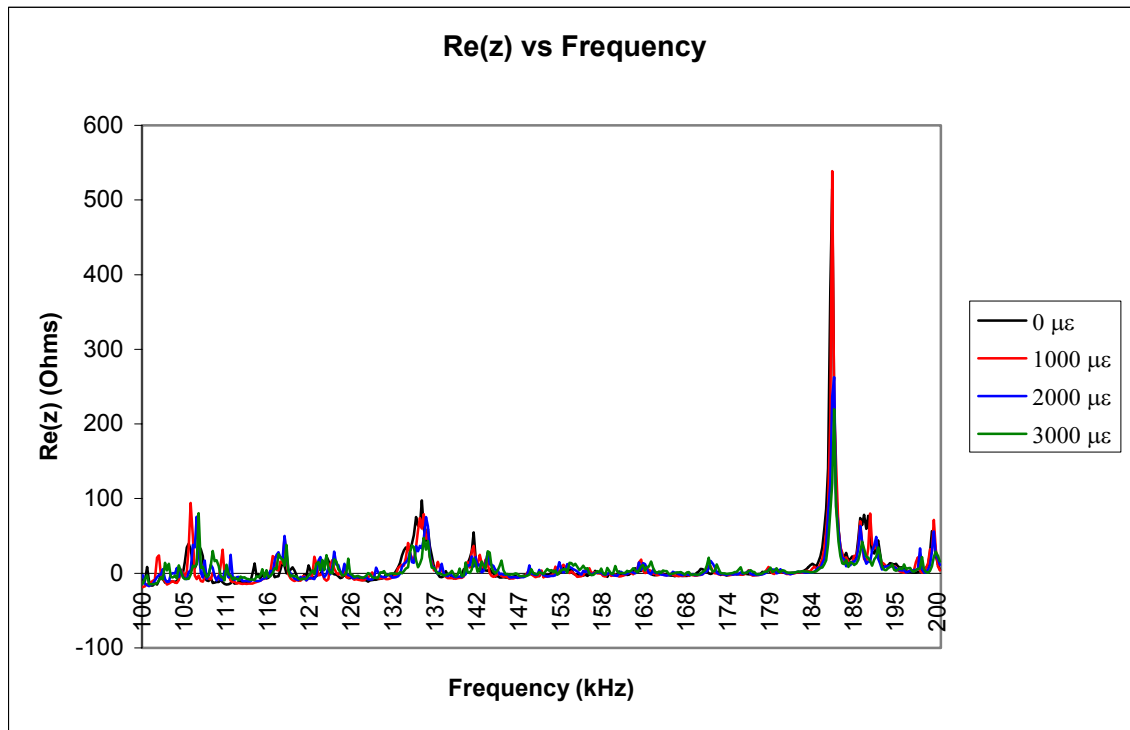


Figure 17 Impedance Signature Comparisons for PWAS 01 for 0 $\mu\epsilon$ to 3000 $\mu\epsilon$

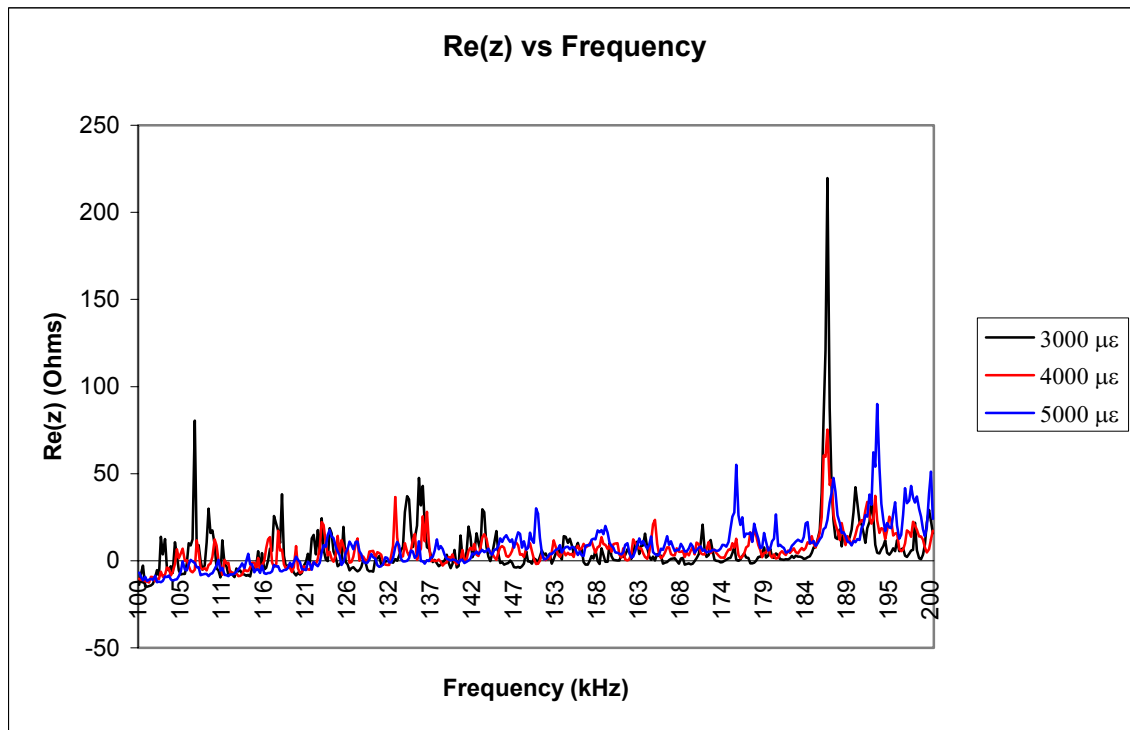


Figure 18 Impedance Signature Comparisons for PWAS 01 for 3000 $\mu\epsilon$ to 5000 $\mu\epsilon$

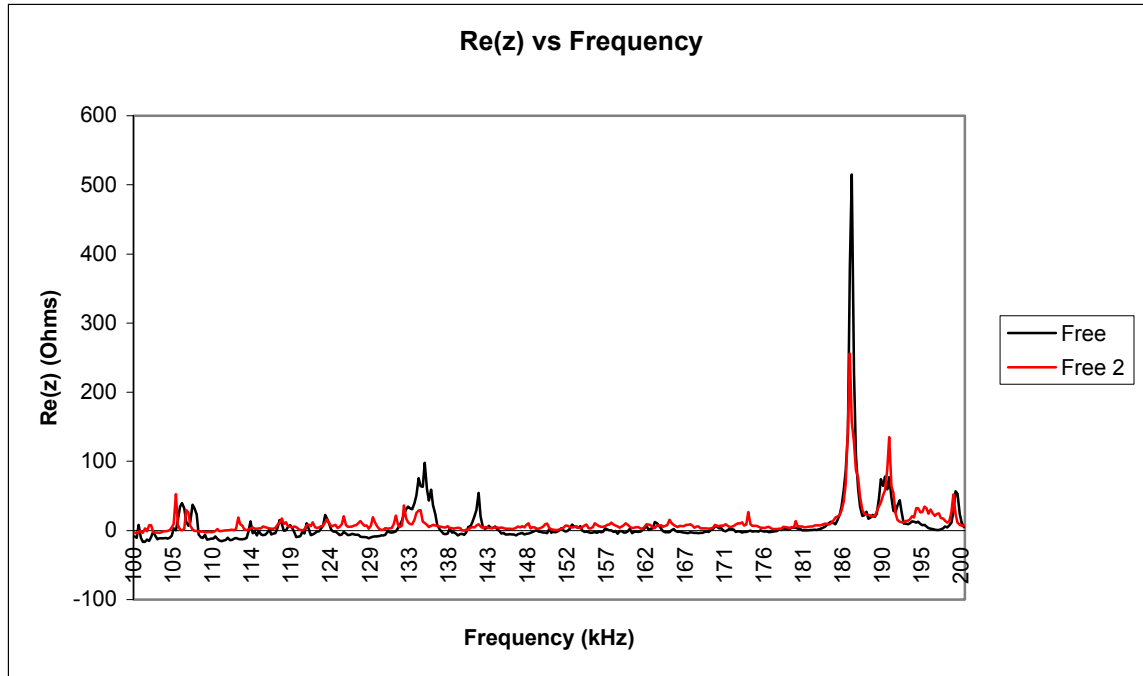


Figure 19 Comparison of Initial Baseline Impedance to Final Unloaded Impedance for PWAS 01

4.4.2.2. Experimental Results for PWAS 02

PWAS number 02 was bonded using M-bond 200 cyanoacrylate with catalyst. Similar to the specimen for PWAS 01 this specimen was installed in the testing machine and the baseline impedance was recorded under zero tension load condition. The specimen was then loaded and impedance readings were made at 200 $\mu\epsilon$ intervals until failure of the PWAS occurred. The baseline impedance for PWAS 02 for a frequency range of 100 to 200 kHz is shown in Figure 20.

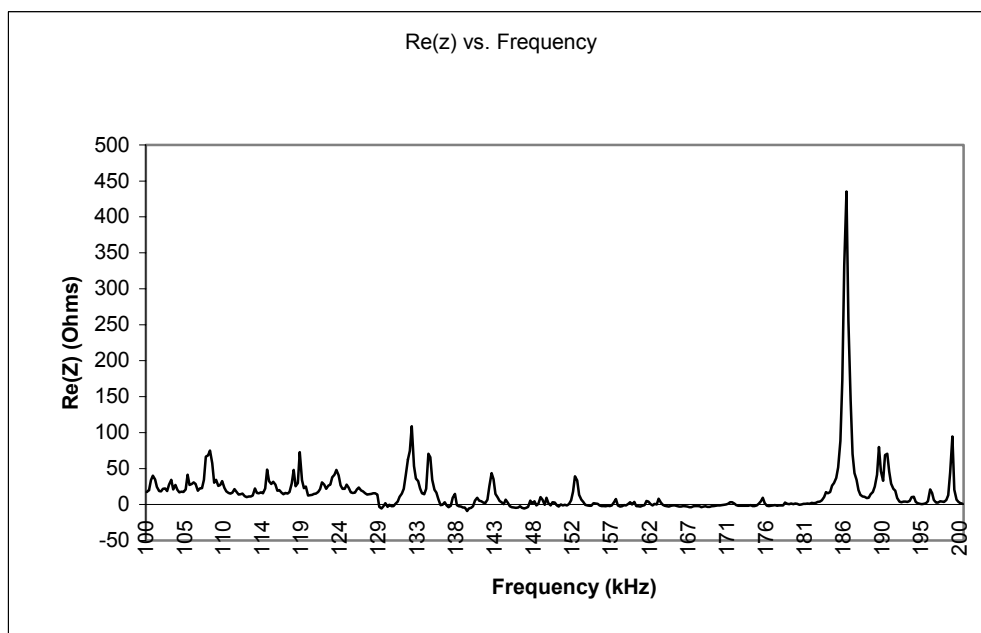


Figure 20 Baseline Impedance for PWAS 02

The specimen was then loaded and new readings were taken at intervals of $200\mu\epsilon$. Figure 21 compares the impedance readings for the baseline up to $3000\mu\epsilon$. As with PWAS 01, no significant changes occurred up to the $3000\mu\epsilon$ level with exception of the peak amplitude decreasing with increasing strain. The comparison from $3000\mu\epsilon$ up to $6000\mu\epsilon$ can be seen in Figure 22. Significant changes begin to happen after $3000\mu\epsilon$ which was also the case for PWAS 01. The peak amplitude continually drops with increased strain. Figure 23 compares impedance readings from $6000\mu\epsilon$ up to $7200\mu\epsilon$. The last reading that could be taken from the PWAS was at $7200\mu\epsilon$. Failure of the PWAS occurred slightly above that strain level and no further measurements could be recorded.

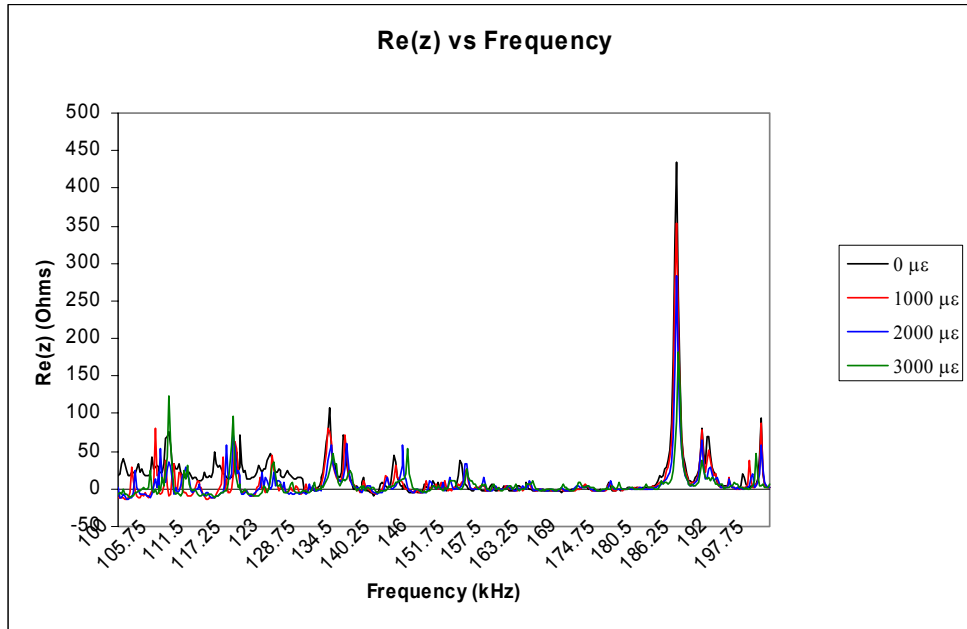


Figure 21 Impedance Signature Comparisons for PWAS 02 for $0\mu\epsilon$ to $3000\mu\epsilon$

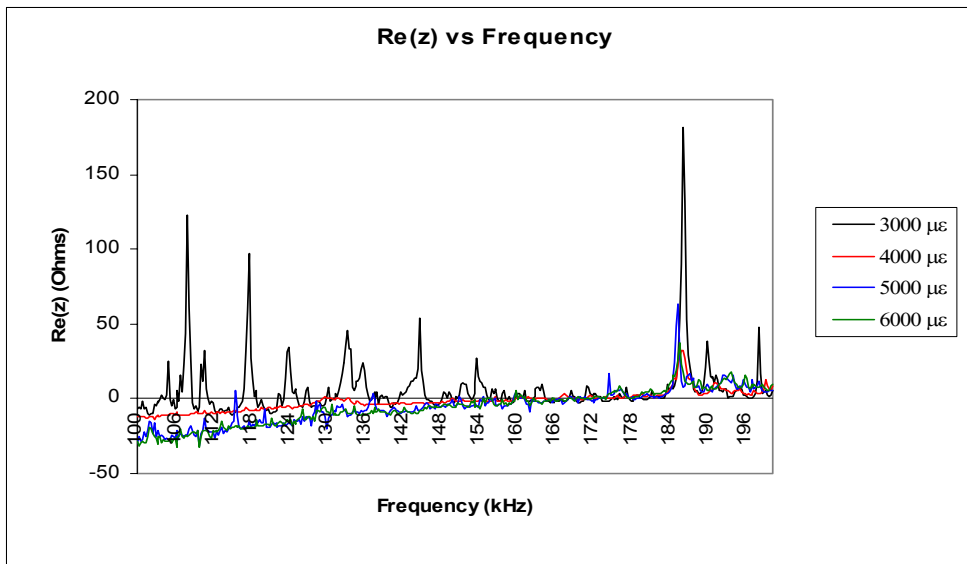


Figure 22 Impedance Signature Comparisons for PWAS 02 for $3000\mu\epsilon$ to $6000\mu\epsilon$

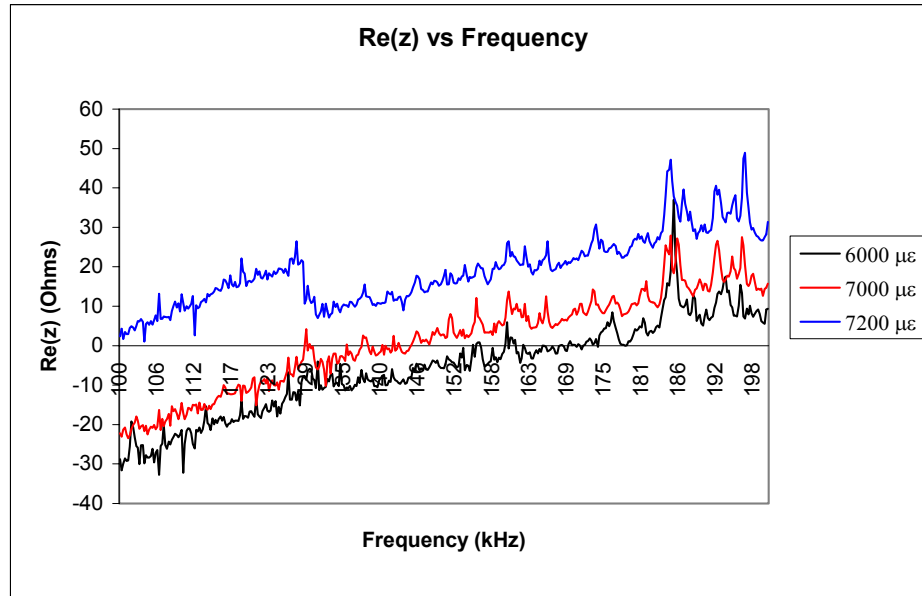


Figure 23 Impedance Signature Comparisons for PWAS 02 for 6000 $\mu\epsilon$ to 7200 $\mu\epsilon$

The specimen was unloaded after every 1000 $\mu\epsilon$ and a new unloaded impedance reading was recorded. The new unloaded impedance was compared to the initial baseline impedance to determine if any permanent changes had occurred. These comparisons can be seen in Figure 24 for strain loadings up to 4000 $\mu\epsilon$ and Figure 25 for strains up to the failure point.

Figure 26 shows a comparison of the imaginary part of the impedance from the original baseline up to 4000 $\mu\epsilon$. The plot continually flattens and converges to the smooth curve shown at 4000 $\mu\epsilon$. After that point, the entire curve drops in value which can be seen in Figure 27. Beyond the level of 5000 $\mu\epsilon$ the plot remains relatively unchanged.

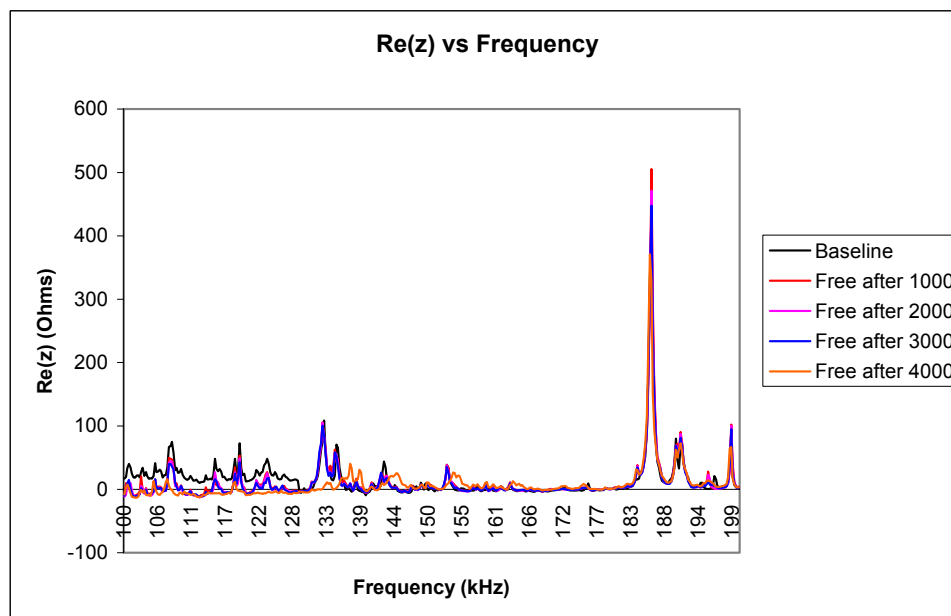


Figure 24 Comparison of Initial Baseline to Unloaded Impedance up to 4000 $\mu\epsilon$ for PWAS 02

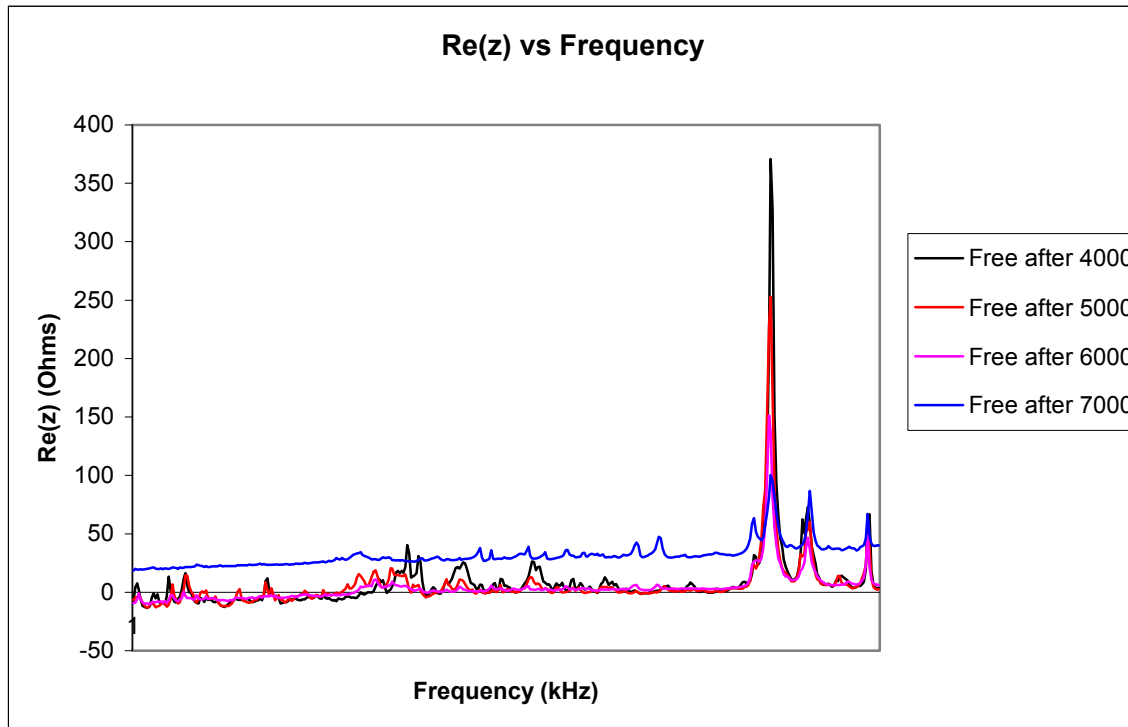


Figure 25 Comparison of Unloaded Impedance from 4000 up to 7000 μs for PWAS 02

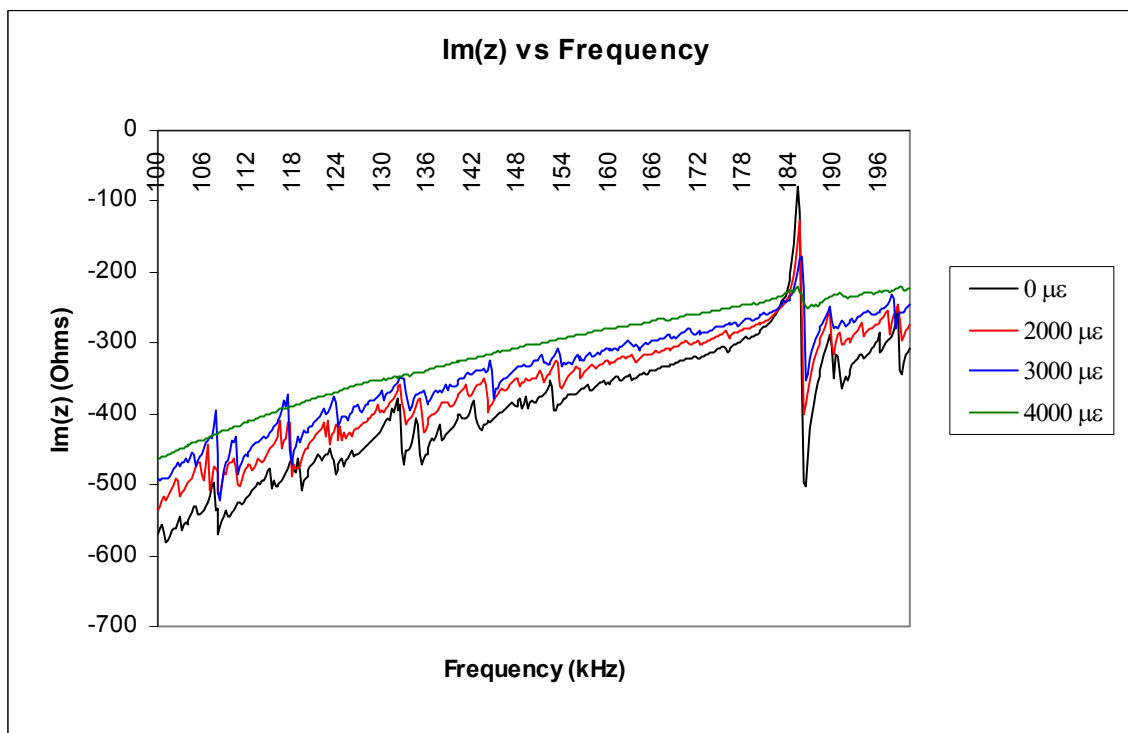


Figure 26 Imaginary Impedance Comparisons for PWAS 02 for 0 μs to 4000 μs

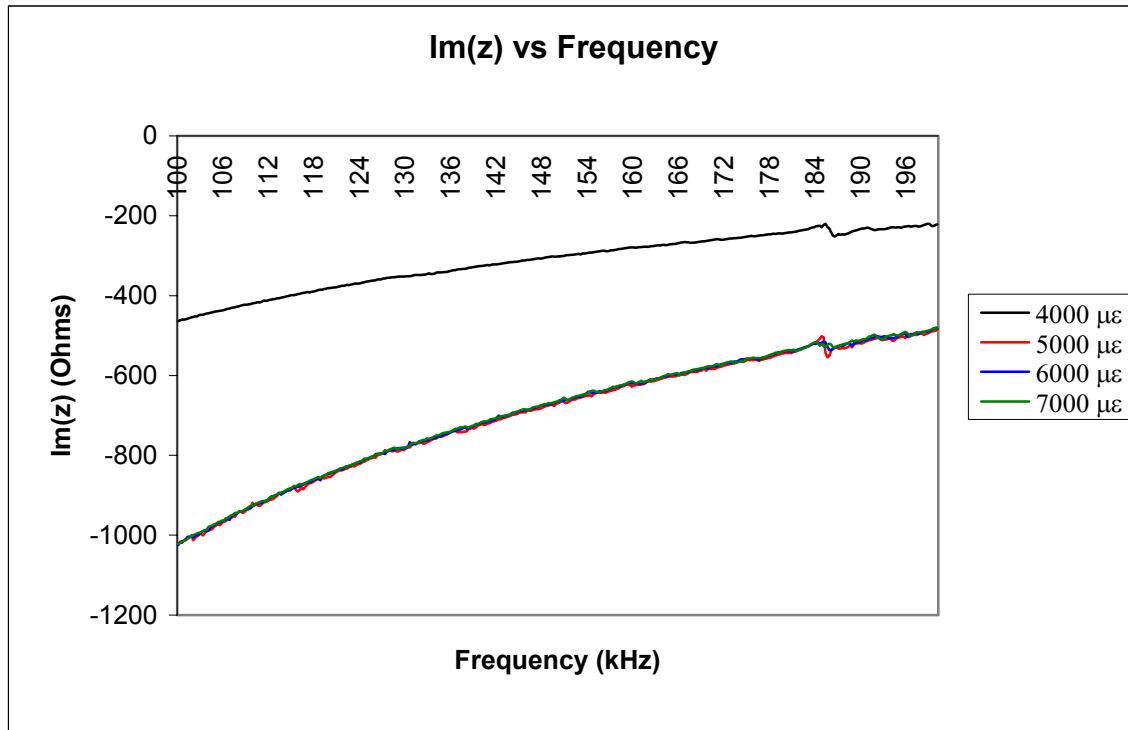


Figure 27 Imaginary Impedance Comparisons for PWAS 02 for 4000 $\mu\epsilon$ to 7000 $\mu\epsilon$

4.5. TASK 1 – CONCLUSIONS

The electromechanical (E/M) impedance spectra of free and bonded PWAS were compared after exposure to various environmental conditions, temperature cycles (oven tests), climatic factors (outdoors tests), operational fluids (immersion tests), and stresses were used. Various adhesives and protective coatings were used in the experiments.

The environment tests (Subtask 1.1 to 1.3) were started about six months ago and are still in progress; so far no significant change is recorded. This means the PWAS and bond between PWAS and aluminum substrate can withstand the temperature range and weather conditions associated with SHM usage. The test will continue for one year so that more data can be collected and analyzed. From the current results, PWAS and the adhesive bond is good for normal use. Future environmental condition tests such as freeze-thaw test and humidity test will be done in the future.

The physical properties test (Subtask 1.4) showed that increasing the strain on a structure with the PWAS attached can change the amplitude of the peaks. As the strain increased, the peak's amplitude decreased. Also it was discovered that strain alters the peaks permanently even after the strain has stopped being applied. Strain at high levels can also damage the PWAS and cause cracking. Future physical properties tests, like the shake test, will be planned for in the future.

5. TASK 2: OPTIMUM PWAS DESIGN

Lamb waves, which are also referred to as guided plate waves, are a type of ultrasonic waves that remain guided between two parallel free surfaces, such as the upper and lower surfaces of a plate or shell. An alternating voltage applied to the PWAS terminals produces an oscillatory expansion and contraction of the PWAS material. Vice-versa, an oscillatory expansion and contraction of the PWAS material produces an alternating voltage at the PWAS terminals. In Lamb-waves applications, PWAS couple their in-plane motion, excited through the piezoelectric effect, with the Lamb-waves particle motion on the material surface. Thus, PWAS can be both exciters and detectors of elastic Lamb waves traveling in the material.

Consider a uniform plate with a PWAS transducer bonded to its top surface. When the PWAS is excited by a harmonic electric voltage $V = V_0 e^{i\omega t}$, elastic Lamb waves are excited inside the structure (Figure 28). The interaction between the PWAS and the structure takes place through the interfacial shear stress $\tau = \tau_0(x) e^{i\omega t}$. The exact spatial distribution of $\tau_0(x)$ depends on the properties of the bonding layer between the PWAS and the structure.

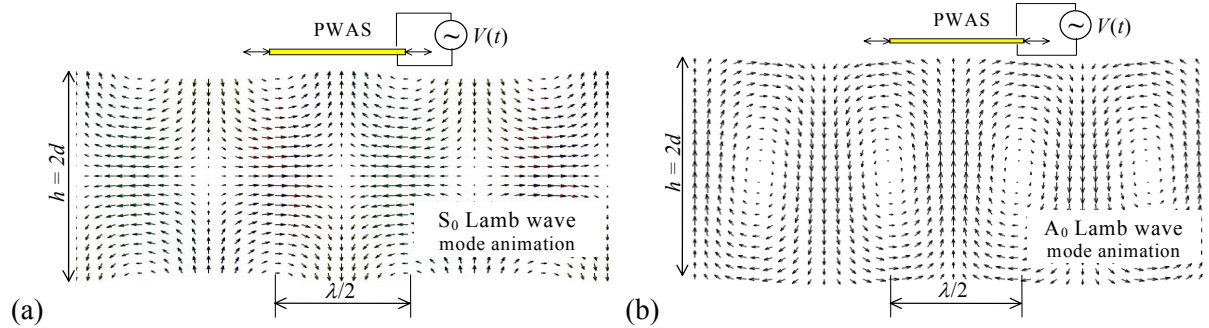


Figure 28 PWAS interaction with Lamb modes: (a) symmetric Lamb mode S_0 ; (b) anti-symmetric Lamb mode A_0

The purpose of Task 2 is to find the optimum design for the PWAS. PWAS can be used in many ways for structural health monitoring and non-destructive evaluation, but if the design of the PWAS is not optimized, the effectiveness and performance of the PWAS can be compromised. It is important to study the waveforms, surface displacement, material properties (thickness, size, etc), effect of frequency, effect the bond, and even the sensor shape to create the ideal monitoring design. Modeling using MATLAB and MathCAD was used to simulate the Lamb waves and predict their behavior. This modeling was used to find the optimum PWAS design for various applications. The design and test for the reciprocity of PWAS lamb wave transmission and reception will also be explored.

Task Overview

- Subtask 2.1 – Development of Software Packages for Lamb Wave Simulation in Various Material Systems
- Subtask 2.2 – Lamb-Wave Modes Tuning with PWAS Transducers
- Subtask 2.3 – Modeling and Design for Reciprocity of PWAS Lamb Wave Transmission-Reception
- Subtask 2.4 – Modeling and Simulation for Detection of Corrosion Using Lamb Waves

5.1. SUBTASK 2.1 –DEVELOPMENT OF SOFTWARE PACKAGES FOR LAMB WAVE SIMULATION IN VARIOUS MATERIAL SYSTEMS

5.1.1. Methods, Assumptions, and Procedures

Software packages were developed using MATLAB and MathCAD applications. The software packages were intended for the study of the Lamb waves behavior as function of material properties and structural geometry. The assumptions adopted in this work were consistent with the standard assumptions of the plain-strain solution to the wave equation in a plate that generate guided Lamb waves. A full description of the basic assumptions and methods underlying this approach is given in Bao (2003).

The procedure used in programming these software packages is consistent with the MATLAB 6.5 programming environment with graphical user interface (GUI) visual tools.

5.1.1.1. Lamb Wave Speed and Mode Shape Simulators

Theoretical modeling of the equations was done using MATLAB and MathCAD simulations. Figure 29 the simulation program for calculating the Lamb wave speed, mode shape, and stress distribution across the thickness and along a wave length. Figure 30 shows the simulation program for calculating the wave speed and group velocity for various material systems and plate thickness values. The GUI windows indicate the graphing and inputting variables for Lamb wave simulations. The material type; Lamb wave mode type; wall thickness; and wave speed and group velocity listed at selected frequencies can be selected in the windows.

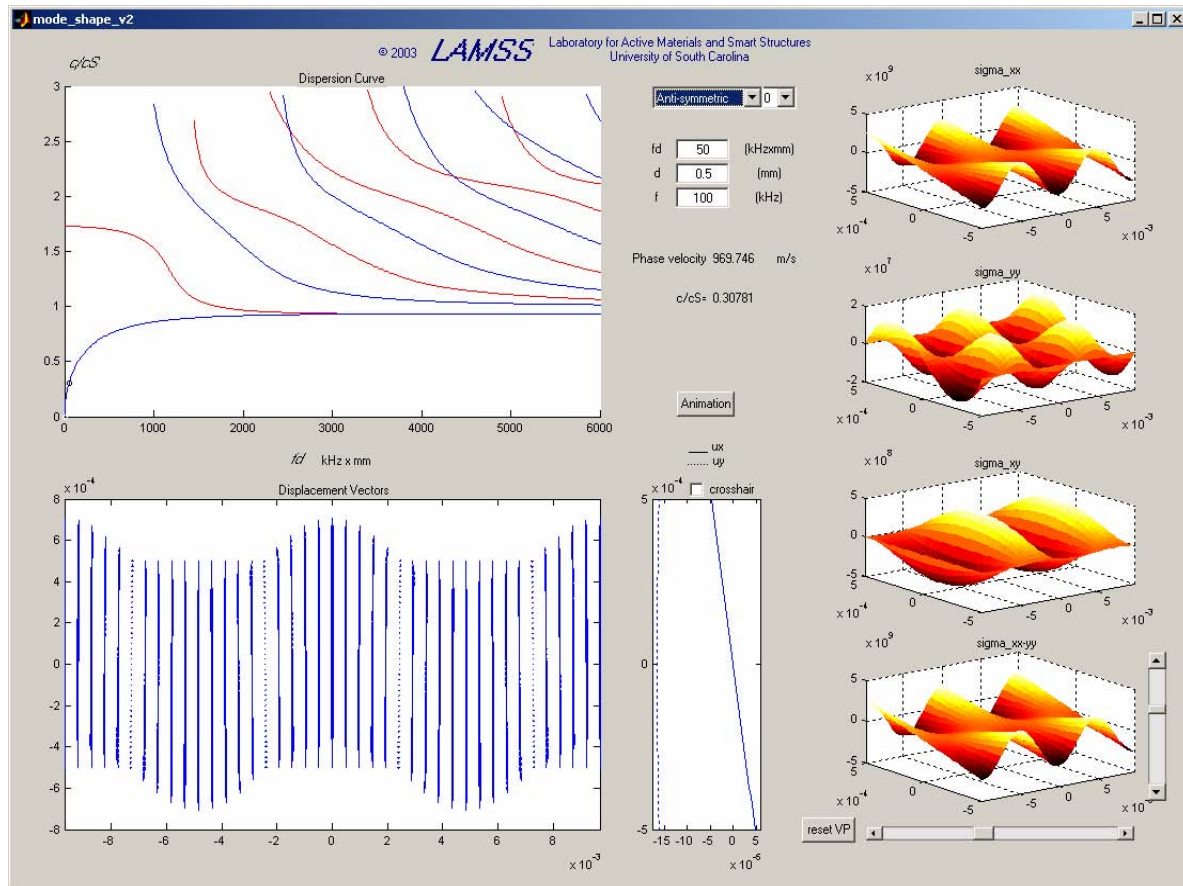


Figure 29 – Lamb mode wave speed, mode shape, and stress distribution simulation program (MODE_SHAPE_V2)

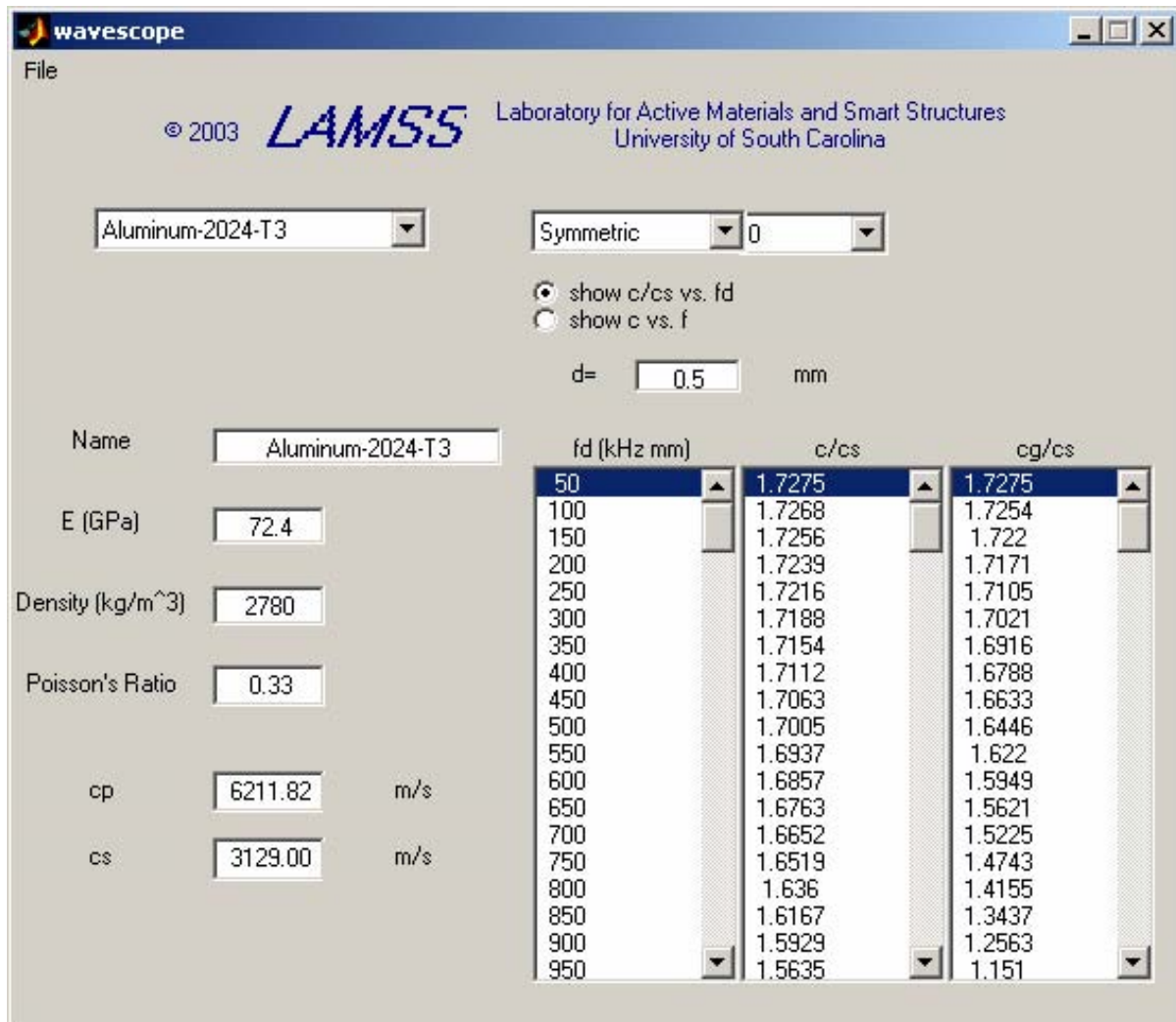


Figure 30 – (Lamb wave speed and group velocity simulation program (WAVESCOPE)).

5.1.1.2. Signal Analysis Software Programs

MATLAB was also used to create a program named “STFT” for performing signal processing with the Short Time Fourier Transform method (Figure 31) and another software program named “WAVELETS” for performing signal processing with the Continuous Wavelet Transform method (Figure 32).

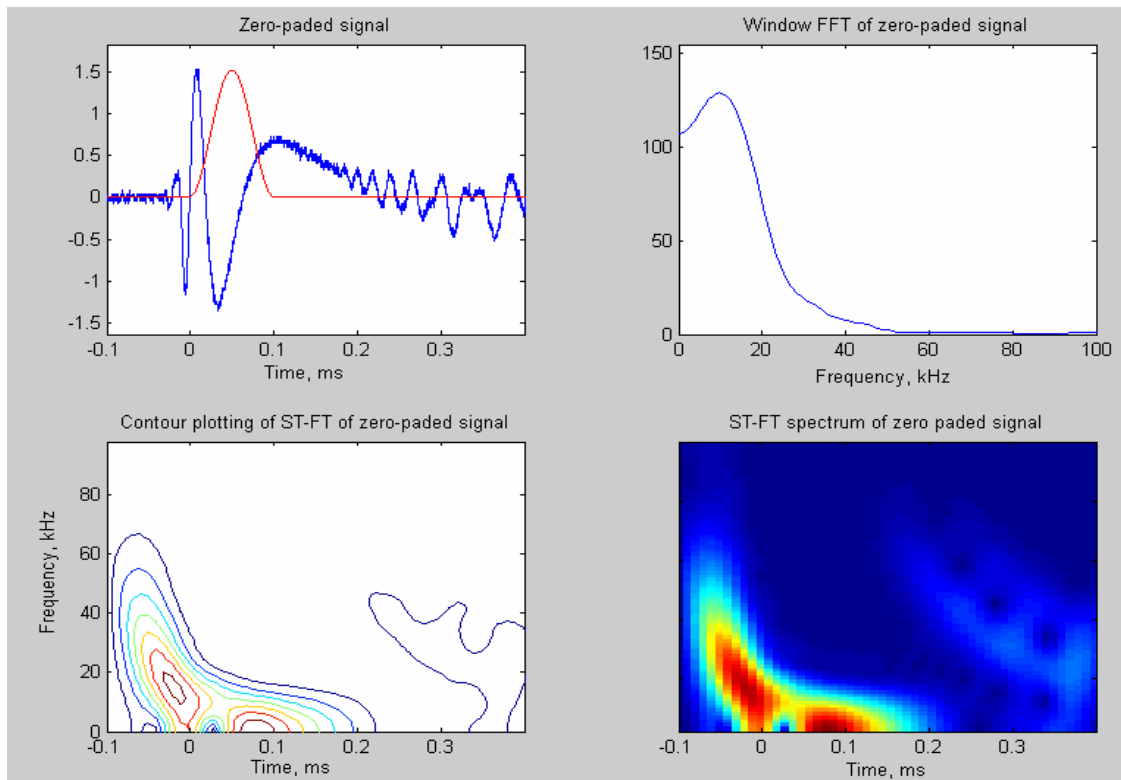


Figure 31 – Software simulation programs for signal analysis using short time Fourier transform (STFT)

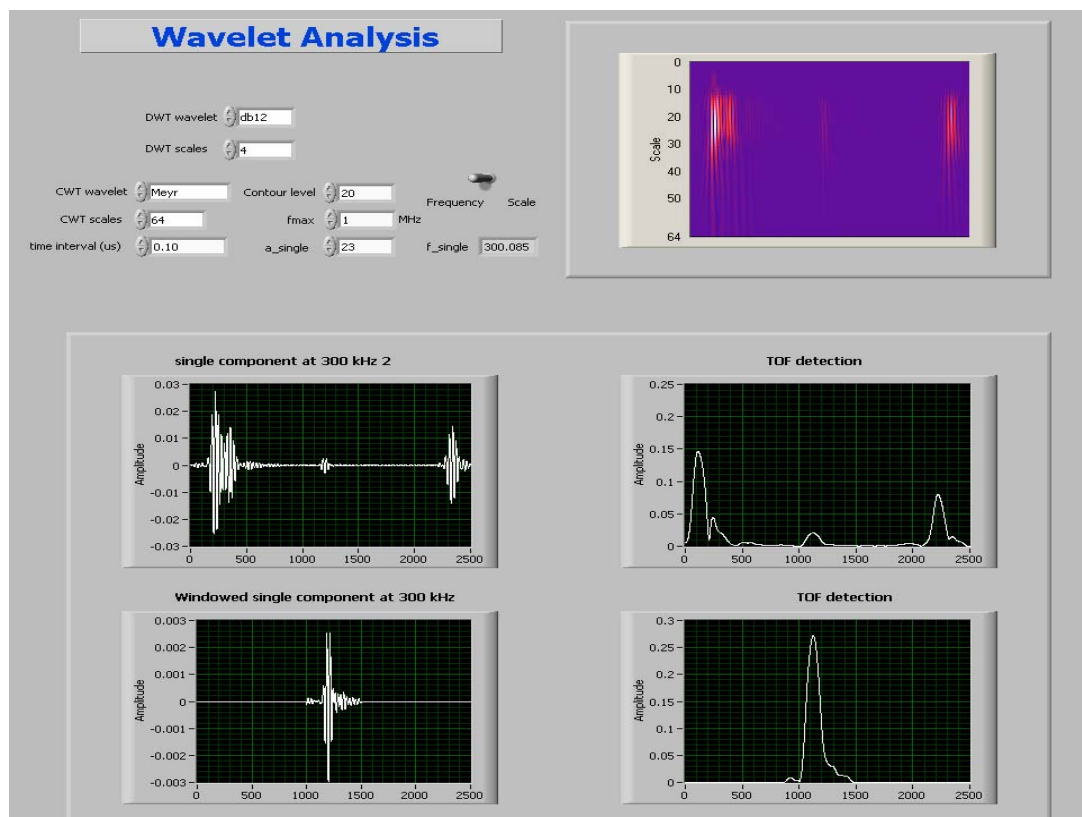


Figure 32 – Software simulation programs for signal analysis using wavelets (WAVELETS).

5.1.1.3. MathCAD Analysis Software Programs

A MathCAD program was developed to predict the propagation of waves of various Lamb modes in a plate. This program was based on the time-domain Fourier transform. It took the Fourier transform of the excitation signal and multiplied it with the Fourier transform of the wave propagation function at various x locations in the plate. The result of this multiplication was subjected to the inverse Fourier transform in order to obtain the wave response at various x locations in the plate.

5.1.2. Results and Discussions

The Lamb-wave simulation programs were very useful for predicting the behavior of Lamb waves for various material and geometric parameters. Various Lamb wave modes could be selected and visualized. The distribution of various stresses across the thickness and along a wavelength could be examined. The signal processing programs were found very useful in processing the experimental data and extracting the useful information from noise. The wave propagation MathCAD programs were found valuable in predicting the changes that appear in the wave signature as it propagates along the plate. These programs were used in the subsequent subtasks to verify the optimum sensor design parameters for various excitation frequencies and to understand the experimental data. All the above mentioned software simulation programs were transmitted to the AFRL personnel for further use in AFRL work.

5.2. SUBTASK 2.2 LAMB-WAVE MODES TUNING WITH PWAS TRANSDUCERS

In this section, we will analyze the case of a surface-mounted PWAS and its interaction with the structural substrate (Figure 33). Because the PWAS is mounted asymmetric with respect to the mid-thickness axis, both symmetric and antisymmetric Lamb-wave modes can be excited and detected. It will be shown that conditions can be found for which the PWAS will couple preferentially with only one of these Lamb-wave modes, i.e., the PWAS are tuned with that particular Lamb-wave mode. The modeling of this phenomenon is done as follows.

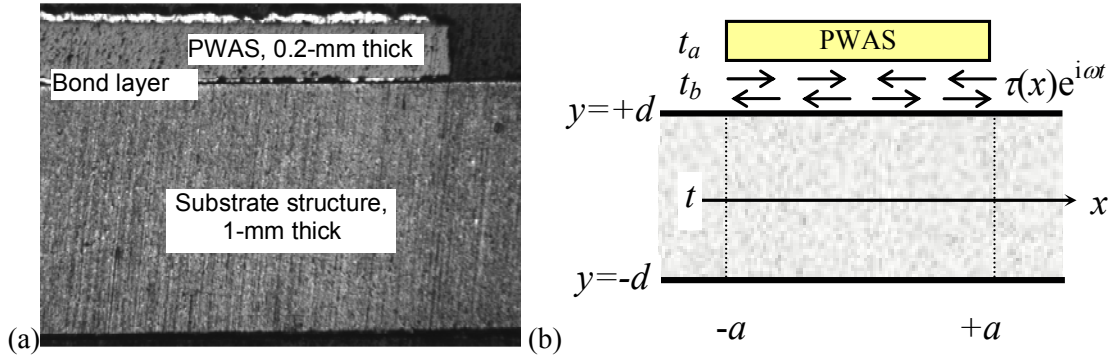


Figure 33 Shear layer interaction between the PWAS and the structure: (a) micrograph; (b) modeling

5.2.1. Methods, Assumptions, and Procedures

Consider the surface mounted PWAS shown in Figure 33b. The PWAS is excited electrically with a time-harmonic voltage $V e^{-i\omega t}$. As a result, the PWAS expands and contracts, and a time-harmonic interfacial shear stress, $\tau_\alpha(x) e^{-i\omega t}$, develops between the PWAS to the structure. This shear stress acts on the structure

over the interval $x \in (-a, +a)$. Thus, the τ_{yx} boundary condition on the structure upper surface ($y = h$) is given by:

$$\tau_{yx}|_{y=h} = \tau_a(x) = \tau_0(x)[H(x+a) - H(x-a)] \quad (1)$$

Where $H(x)$ is the Heaviside step function and the time-harmonic variation $e^{-i\omega t}$ is implied. From this point onwards, the analysis is performed in the wave number domain by applying the space-domain Fourier transform:

$$\tilde{f}(\xi) = \int_{-\infty}^{\infty} f(x)e^{-i\xi x} dx, \quad f(x) = \frac{1}{2\pi} \int_{-\infty}^{\infty} \tilde{f}(\xi)e^{i\xi x} d\xi \quad (2)$$

Where $\xi = \frac{\omega}{c}$ is the wave number; the space-domain Fourier transform of the excitation (1) is

$$\tilde{\tau}_a = \int_{-\infty}^{\infty} \tau_0(x)[H(x+a) - H(x-a)]e^{-i\xi x} dx \quad (3)$$

Applying the space-domain Fourier transform to the wave equations and the displacements, stresses and strains we obtain:

$$\begin{aligned} \frac{d^2 \tilde{\phi}}{dy^2} + p^2 \tilde{\phi} &= 0 \\ \frac{d^2 \tilde{\psi}}{dy^2} + q^2 \tilde{\psi} &= 0 \end{aligned} \quad (4)$$

$$\begin{aligned} \tilde{u}_x &= i\xi \tilde{\phi} + \frac{d\tilde{\psi}}{dy} & \tilde{\tau}_{yx} &= \mu \left(2i\xi \frac{d\tilde{\phi}}{dy} + \xi^2 \tilde{\psi} + \frac{\partial^2 \tilde{\psi}}{\partial y^2} \right) \\ \tilde{u}_y &= \frac{d\tilde{\phi}}{dy} - i\xi \tilde{\psi} & \tilde{\tau}_{yy} &= \lambda \left(-\xi^2 \tilde{\phi} + \frac{d^2 \tilde{\phi}}{dy^2} \right) + 2\mu \left(-\xi^2 \tilde{\phi} - i\xi \frac{d\tilde{\psi}}{dy} \right), & \tilde{\epsilon}_x &= i\xi u_x \end{aligned} \quad (5)$$

where p and q are: $p^2 = \frac{\omega^2}{c_L^2} - \xi^2$, $q^2 = \frac{\omega^2}{c_T^2} - \xi^2$, ϕ and ψ are two potential functions, $c_p^2 = (\lambda + 2\mu) / \rho$

and $c_s^2 = \mu / \rho$ are the pressure (longitudinal) and shear (transverse) wave speeds, λ and μ are the Lamé constants, ρ is the mass density. The time dependence is assumed harmonic in the form $e^{-i\omega t}$.

Equation (4) accepts the general solution

$$\begin{aligned} \tilde{\phi} &= A_1 \sin py + A_2 \cos py \\ \tilde{\psi} &= B_1 \sin qy + B_2 \cos qy \end{aligned} \quad (6)$$

As before, the constants A_2 and B_1 correspond to symmetric motion, while A_1 and B_2 correspond to antisymmetric motion. The excitation can be also split into symmetric and antisymmetric components (Figure 34), i.e.,

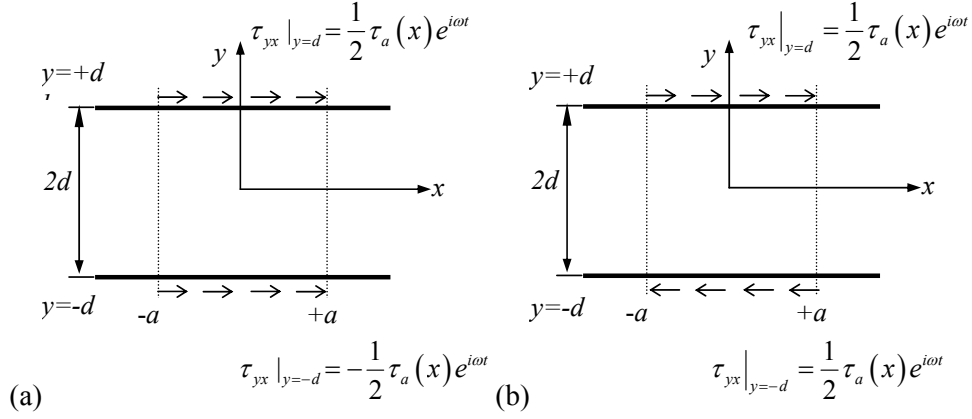


Figure 34 Symmetric and antisymmetric loading from a PWAS of width $2a$ mounted on the plate upper surface: (a) symmetric loading and (b) anti-symmetric loading

$$\begin{aligned}\tilde{\tau}|_{y=d} &= \frac{1}{2} \tilde{\tau}_a|_{y=d} + \frac{1}{2} \tilde{\tau}_a|_{y=d} = \tilde{\tau}_a \quad \text{upper surface} \\ \tilde{\tau}|_{y=-d} &= -\frac{1}{2} \tilde{\tau}_a|_{y=-d} + \frac{1}{2} \tilde{\tau}_a|_{y=-d} = 0 \quad \text{lower surface}\end{aligned}\tag{7}$$

Note that the negative sign on the symmetric part of $\tilde{\tau}|_{y=-d}$ is due to the sign convention defining the shear stresses on the upper and lower surfaces.

5.2.2. Results and Discussions

5.2.2.1. Symmetric Solution

The symmetric boundary conditions are:

$$\begin{aligned}\tilde{u}_x(\xi)|_{y=-d} &= \tilde{u}_x(\xi)|_{y=d} & \tilde{\tau}_{yx}(\xi)|_{y=-d} &= -\tilde{\tau}_{yx}(\xi)|_{y=d} = \frac{\tilde{\tau}_a}{2} \\ \tilde{u}_y(\xi)|_{y=-d} &= -\tilde{u}_y(\xi)|_{y=d} & \tilde{\tau}_{yy}(\xi)|_{y=-d} &= -\tilde{\tau}_{yy}(\xi)|_{y=d} = 0\end{aligned}\tag{8}$$

Because the motion is assumed symmetric, only the constants A_2 and B_1 are retained in Equation (6) and, upon substitution into (5), obtain

$$\begin{aligned}\tilde{u}_x &= i\xi A_2 \cos py + qB_1 \cos qy \\ \tilde{u}_y &= pA_2 \sin py - i\xi B_1 \sin qy\end{aligned}\tag{9}$$

$$\begin{aligned}\tilde{\tau}_{yx} &= \mu \left[-2i\xi pA_2 \sin py + (\xi^2 - q^2)B_1 \sin qy \right] \\ \tilde{\tau}_{yy} &= \mu \left[(\xi^2 - q^2)A_2 \cos py + 2i\xi qB_1 \cos qy \right]\end{aligned}\tag{10}$$

$$\tilde{\varepsilon}_x = -\xi^2 A_2 \cos py + i\xi qB_1 \cos qy\tag{11}$$

Substitution of Equations (9) and (10) into the boundary conditions (8) yields the linear system

$$\begin{aligned}
(-2i\xi p \sin pd) A_2 + [(\xi^2 - q^2) \sin qd] B_1 &= \frac{1}{2\mu} \tilde{\tau}_a \\
[(\xi^2 - q^2) \cos pd] A_2 + (2i\xi q \cos qd) B_1 &= 0
\end{aligned} \tag{12}$$

Solution of Equation (12) yields

$$\begin{aligned}
A_2 &= \frac{\tilde{\tau}}{2\mu} \frac{N_{A_2}}{D_S} & N_{A_2} &= 2i\xi q \cos qd, & N_{B_1} &= (\xi^2 - q^2) \cos pd \\
B_1 &= \frac{\tilde{\tau}}{2\mu} \frac{N_{B_1}}{D_S} & D_S &= (\xi^2 - q^2)^2 \cos pd \sin qd + 4\xi^2 pq \sin pd \cos qd
\end{aligned} \tag{13}$$

Note that the denominator D_S is the same as the left hand side of the characteristic equation for symmetric motion. This indicates that the poles of Equation (13) correspond to the symmetric Lamb-wave eigenvalues. Substitution of Equation (13) into Equation (11) yields the wave number-domain displacement and strain at the plate upper surface

$$\begin{aligned}
\tilde{u}_x^S \Big|_{y=d} &= -\frac{1}{\xi} \frac{\tilde{\tau}}{2\mu} \frac{N_S}{D_S} & \tilde{\varepsilon}_x^S \Big|_{y=d} &= -i \frac{\tilde{\tau}}{2\mu} \frac{N_S}{D_S}
\end{aligned} \tag{14}$$

Where:

$$N_S = \xi q (\xi^2 + q^2) \cos pd \cos qd \tag{15}$$

5.2.2.2. Antisymmetric Solution

The antisymmetric boundary conditions are

$$\begin{aligned}
\tilde{u}_x(\xi) \Big|_{y=-d} &= -\tilde{u}_x(\xi) \Big|_{y=-d} & \tilde{\tau}_{yx}(\xi) \Big|_{y=-d} &= \tilde{\tau}_{yx}(\xi) \Big|_{y=d} = \frac{\tilde{\tau}_a}{2} \\
\tilde{u}_y(\xi) \Big|_{y=-d} &= \tilde{u}_y(\xi) \Big|_{y=-d} & \tilde{\tau}_{yy}(\xi) \Big|_{y=-d} &= -\tilde{\tau}_{yy}(\xi) \Big|_{y=d} = 0
\end{aligned} \tag{16}$$

Because the motion is assumed antisymmetric, only the constants A_1 and B_2 are retained in Equation (6) and, upon substitution into (5), obtain

$$\begin{aligned}
\tilde{u}_x &= i\xi A_1 \sin py - qB_2 \sin qy \\
\tilde{u}_y &= pA_1 \cos py - i\xi B_2 \cos qy
\end{aligned} \tag{17}$$

$$\begin{aligned}
\tilde{\tau}_{yx} &= \mu [2i\xi p A_1 \cos py + (\xi^2 - q^2) B_2 \cos qy] \\
\tilde{\tau}_{yy} &= \mu [(\xi^2 - q^2) A_1 \sin py + 2i\xi q B_2 \sin qy]
\end{aligned} \tag{18}$$

$$\tilde{\varepsilon}_x = -\xi^2 A_1 \sin py - i\xi q B_2 \sin qy \tag{19}$$

Substitution of Equations (17) and (18) into the boundary conditions (16) yields the linear system

$$\begin{aligned}
(2i\xi p \sin pd) A_1 + [(\xi^2 - q^2) \cos qd] B_2 &= \frac{1}{2\mu} \tilde{\tau}_a \\
[(\xi^2 - q^2) \sin pd] A_1 + (2i\xi q \sin qd) B_2 &= 0
\end{aligned} \tag{20}$$

Solution of Equation (20) yields

$$\begin{aligned} A_1 &= \frac{\tilde{\tau}_a}{2\mu} \frac{N_{A_1}}{D_A} & N_{A_1} &= 2i\xi q \sin qd, & N_{B_2} &= -(\xi^2 - q^2) \sin pd \\ B_2 &= \frac{\tilde{\tau}_a}{2\mu} \frac{N_{B_2}}{D_A} & D_A &= (\xi^2 - q^2)^2 \sin pd \cos qd + 4\xi^2 pq \cos pd \sin qd \end{aligned} \quad (21)$$

Note that the denominator D_A is the same as the left hand side of the characteristic equation antisymmetric motion. This indicates that the poles of Equation (21) correspond to the antisymmetric Lamb-wave eigenvalues. Substitution of Equation (21) into Equation (19) yields the wave number-domain displacement and strain at the plate upper surface

$$\tilde{u}_x^A \Big|_{y=d} = -\frac{1}{\xi} \frac{\tilde{\tau}}{2\mu} \frac{N_A}{D_A} \quad \tilde{\varepsilon}_x^A \Big|_{y=d} = -i \frac{\tilde{\tau}}{2\mu} \frac{N_A}{D_A} \quad (22)$$

Where:

$$N_A = \xi q (\xi^2 + q^2) \sin pd \sin qd \quad (23)$$

5.2.2.3. Complete Response

The complete response to the PWAS excitation is obtained by combining the symmetric and antisymmetric responses, i.e.,

$$\tilde{\varepsilon}_x^A \Big|_{y=d} = -i \frac{\tilde{\tau}_a}{2\mu} \left(\frac{N_S}{D_S} + \frac{N_A}{D_A} \right) \quad (24)$$

$$\tilde{u}_x \Big|_{y=d} = -\frac{1}{\xi} \frac{\tilde{\tau}_a}{2\mu} \left(\frac{N_S}{D_S} + \frac{N_A}{D_A} \right) \quad (25)$$

We now return from the wave number domain into the space domain by applying the inverse Fourier transform, i.e.,

$$\begin{aligned} \varepsilon_x(x, t) \Big|_{y=d} &= \frac{1}{2\pi} \frac{-i}{2\mu} \int_{-\infty}^{\infty} \left(\tilde{\tau}_a(\xi) \frac{N_S(\xi)}{D_S(\xi)} + \tilde{\tau}_a(\xi) \frac{N_A(\xi)}{D_A(\xi)} \right) e^{i(\xi x - \omega t)} d\xi \\ u_x(x, t) \Big|_{y=d} &= \frac{1}{2\pi} \frac{-1}{2\mu} \int_{-\infty}^{\infty} \frac{1}{\xi} \left(\tilde{\tau}_a(\xi) \frac{N_S(\xi)}{D_S(\xi)} + \tilde{\tau}_a(\xi) \frac{N_A(\xi)}{D_A(\xi)} \right) e^{i(\xi x - \omega t)} d\xi \end{aligned} \quad (26)$$

Though not explicitly shown, the functions N_S , D_S , N_A , D_A , also depend on ω . The integral in Equation (26) is singular at the roots of D_S and D_A , which are the symmetric and anti-symmetric eigenvalues of the Rayleigh-Lamb equation, i.e., $\xi_0^S, \xi_1^S, \xi_2^S, \dots$ and $\xi_0^A, \xi_1^A, \xi_2^A, \dots$. Since the functions D_S and D_A depend on ω , the number of eigenvalues that exist for a given ω will also vary. At low frequencies, i.e., $\omega \rightarrow 0$, only two eigenvalues exist, ξ_0^S and ξ_0^A . At higher frequencies, several eigenvalues will exist. The evaluation of the integral in Equation (26) is done by the residue theorem, using a contour consisting of a semicircle in the upper half of the complex ξ plane and the real axis. Hence:

$$\begin{aligned}
\varepsilon_x(x,t)|_{y=d} &= \frac{1}{2\mu} \left(\sum_{\xi^S} \text{Res @ } \xi^S + \sum_{\xi^A} \text{Res @ } \xi^A \right) e^{i(\xi x - \omega t)} \\
&= \frac{1}{2\mu} \left[\sum_{\xi^S} \tilde{\tau}_a(\xi^S) \frac{N_S(\xi^S)}{D'_S(\xi^S)} + \sum_{\xi^A} \tilde{\tau}_a(\xi^A) \frac{N_A(\xi^A)}{D'_A(\xi^A)} \right] e^{i(\xi x - \omega t)}
\end{aligned} \tag{27}$$

The summations are taken over all the symmetric and antisymmetric eigenvalues that exist at the particular frequency at which the analysis is conducted. Similarly,

$$u_x(x,t)|_{y=d} = \frac{-i}{2\mu} \left[\sum_{\xi^S} \frac{\tilde{\tau}(\xi^S)}{\xi^S} \frac{N_S(\xi^S)}{D'_S(\xi^S)} + \sum_{\xi^A} \frac{\tilde{\tau}(\xi^A)}{\xi^A} \frac{N_A(\xi^A)}{D'_A(\xi^A)} \right] e^{i(\xi x - \omega t)} \tag{28}$$

5.2.2.4. Closed-form Solution for Ideal Bonding

For thin and stiff bonding layers ideal bonding between the PWAS and the structure may be asymptotically achieved. For ideal bonding conditions, the shear stress in the bonding layer takes the simple form of $\tau_a(x) = a\tau_0 [\delta(x-a) - \delta(x+a)]$, which admits a closed-form Fourier transform, i.e.,

$$\tau(x)|_{y=d} = a\tau_0 [\delta(x-a) - \delta(x+a)], \quad \tilde{\tau} = a\tau_0 [-2i \sin \xi a] \tag{29}$$

Hence, the strain-wave solution becomes:

$$\varepsilon_x(x,t)|_{y=d} = -i \frac{a\tau_0}{\mu} \sum_{\xi^S} (\sin \xi^S a) \frac{N_S(\xi^S)}{D'_S(\xi^S)} e^{i(\xi^S x - \omega t)} - i \frac{a\tau_0}{\mu} \sum_{\xi^A} (\sin \xi^A a) \frac{N_A(\xi^A)}{D'_A(\xi^A)} e^{i(\xi^A x - \omega t)} \tag{30}$$

Similarly, the displacement-wave solution becomes:

$$u_x(x,t)|_{y=d} = -\frac{a\tau_0}{\mu} \sum_{\xi^S} \frac{\sin \xi^S a}{\xi^S} \frac{N_S(\xi^S)}{D'_S(\xi^S)} e^{i(\xi^S x - \omega t)} - \frac{a\tau_0}{\mu} \sum_{\xi^A} \frac{\sin \xi^A a}{\xi^A} \frac{N_A(\xi^A)}{D'_A(\xi^A)} e^{i(\xi^A x - \omega t)} \tag{31}$$

These expressions for Lamb wave response under PWAS excitation have been first published by Giurgiutiu, V.; Bao, J.; Zhao, W. (2003). Equations (30) and (31) contain the $\sin \xi a$ function. Thus, mode tuning is possible through the maxima and minima of the $\sin \xi a$ function. Maxima of $\sin \xi a$ occur when $\xi a = (2n-1)\frac{\pi}{2}$. Since $\xi = \frac{2\pi}{\lambda}$, maxima will occur when the PWAS length $l_a = 2a$ equals on odd

multiple of the half wavelength $\frac{\lambda}{2}$. This is **wavelength tuning**. In the same time, minima of $\sin \xi a$ will

occur when $\xi a = n\pi$, i.e., when the PWAS wavelength is a multiple of the wavelength. Since each Lamb-wave mode has a different wavespeed and wavelength, such matching between the PWAS length and the wavelength multiples and submultiples will happen at different frequencies for different Lamb modes. An extensive discussion of this effect in terms of wave number spectra was given by Sonti (1995). Another factor that must be considered in Lamb wave tuning under PWAS excitation is the **mode amplitude tuning**, i.e., the matching of the PWAS location across the structural thickness with the modal displacement at that location. This factor is contained in the values taken by the function N/D' . For example, if the PWAS is surface mounted, it is conceivable that, at a given frequency, some modes may have less surface amplitudes, while other may have larger surface amplitudes. Thus, two important factors for the design of PWAS-based Lamb-wave structural health monitoring systems has been identified:

- The variation of $|\sin \xi a|$ with frequency for each Lamb wave mode
- The variation of the surface strain with frequency for each Lamb wave mode

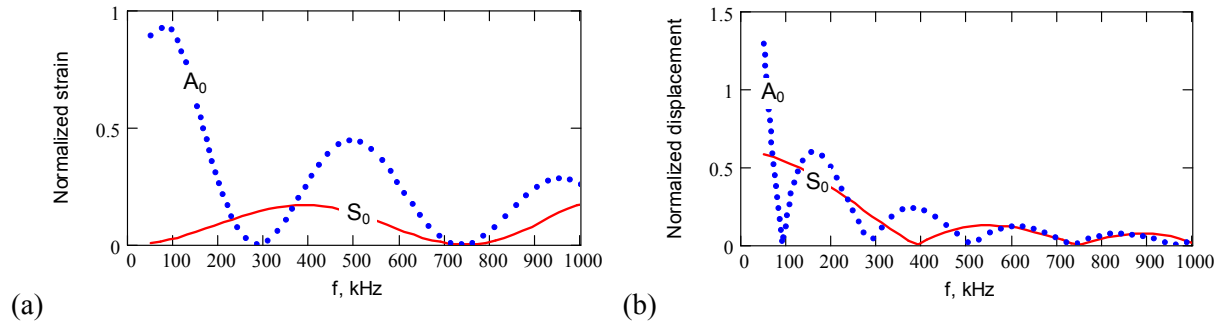


Figure 35 – (a) Predicted Lamb-wave response a 1-mm aluminum plate under a 7-mm PWAS excitation: (a) strain response; (b) displacement response

A plot of Equations (30) and (31) in the frequency range up to 1000 kHz is presented in Figure 35. (The S_0 mode response is drawn with continuous line, while the A_0 mode response is drawn with dotted line.) It is apparent that the strain response is stronger at higher frequencies than the displacement response. This observation is consistent with the fact that the strain varies like $\sin \alpha$, while the displacement varies like $\text{sinc} \alpha = \frac{\sin \alpha}{\alpha}$. This indicates that the PWAS transducers, which are strain coupled, may have a better

high frequencies response than displacement and velocity transducers.

The Lamb-wave mode tuning principles derived here for an exciter PWAS apply equally well for a receiver PWAS. In this case, the receiver PWAS would be able to selectively detect certain Lamb-wave modes from a multimodal Lamb wave reception. An extension of this approach to circular crested Lamb waves was recently presented by Raghavan and Cesnik (2004)¹⁰

A MathCAD program for calculating various axial and flexural wave parameters was also created. (Flexural waves are the low frequency asymptote of A_0 Lamb waves.) The program calculates the S_0 and A_0 mode tuning frequency as function of plate thickness and PWAS radius. It also calculates wave speed and wave length as function of frequency and plate thickness.

5.3. SUBTASK 2.3 –MODELING AND DESIGN FOR RECIPROCITY OF PWAS LAMB WAVE TRANSMISSION-RECEPTION

5.3.1. Methods, Assumptions, and Procedures

The objective of Subtask 2.3 is to explore the reciprocity (relation of mutual dependence, action, interchange, or influence) and design for embedding piezoelectric wafer active sensors (PWAS) to excite and detect tuned Lamb waves for structural health monitoring. If PWAS can effectively generate and detect structural waves, PWAS layouts can be designed in arrays to detect damage by sensing a change in the wave from one sensor to the other. The two Lamb wave modes that were used were symmetric mode (S_0) and antisymmetric mode (A_0). Before going into the procedure section, a brief review of Lamb-waves modes with PWAS theory will be presented.

5.3.1.1. Prediction of Reciprocity

Theoretical modeling was performed and then verified with experimental tests. A 1-D Lamb wave propagation was created using modeling and experimental testing. The specimen was a 2024 T3

aluminum plate with the thickness of 1.6 mm, PWAS separation of 250 mm, and the excitation of 3-count sine tone burst at a frequency of 78 kHz. Figure 36 shows a good comparison between the modeling and experiment.

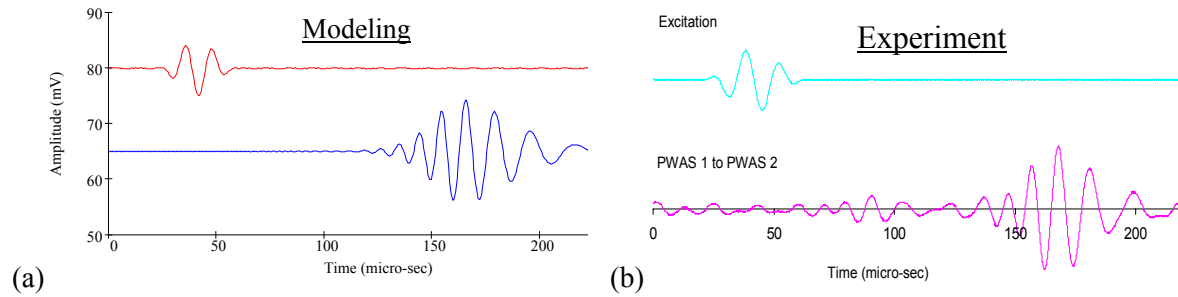


Figure 36 – Plots to the modeling (a) and experiment (b).

5.3.1.2. Test of Reciprocity

A 1.6mm thick, 2024 aluminum alloy plate instrumented with an array of 7 mm x 7 mm PWAS sensors (Figure 37) was used. An HP33120A arbitrary signal generator was used to generate excitation signals. A Tektronix TDS210 two-channel digital oscilloscope was used to collect the response signals from the PWAS wafer active sensors. The instrumentation setup is presented in Figure 37. The PWAS locations on the plate are given in Table 3.

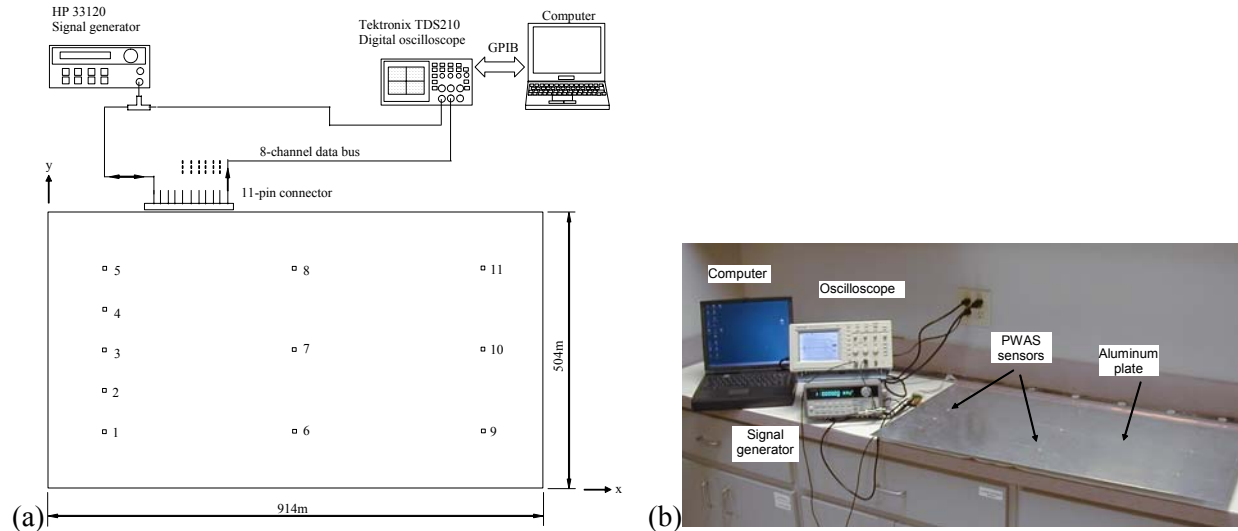


Figure 37 The instrumentation setup: (a) schematic of the location of the PWAS sensors on the Aluminum plate as well as the equipment necessary to generate and capture the signals; (b) picture of the actual equipment and location of sensors

Table 3 Location of PWAS sensors on the Aluminum plate

| Sensor# | X (mm) | Y (mm) |
|---------|--------|--------|
| 1 | 100 | 100 |
| 2 | 100 | 175 |
| 3 | 100 | 250 |
| 4 | 100 | 325 |
| 5 | 100 | 400 |
| 6 | 450 | 100 |
| 7 | 450 | 250 |
| 8 | 450 | 400 |
| 9 | 800 | 100 |
| 10 | 800 | 250 |
| 11 | 800 | 400 |

The excitation signal was a 3-count sine burst wave with Hanning window. The Hanning windowed signal is defined as: $y_i = 0.5x_i[1 - \cos(\omega)]$, where $\omega = \frac{2\pi i}{n}$, and n is the number of counts (Figure 38). The generated signal has a frequency of 300 kHz (100 kHz x 3 counts) for the S_0 mode and 120 kHz (40 kHz x 3 counts) for the A_0 mode.

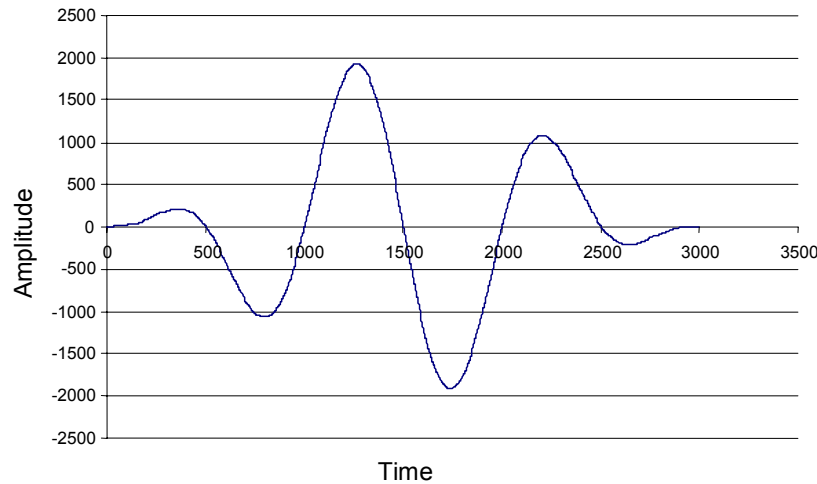


Figure 38 Excitation signal

5.3.2. Results and Discussions

The results are presented in Figure 39 through Figure 44, which show the transmitted and received signals using pair of PWAS sensors in a reciprocal way (#1 = T, #7 = R; #7 = T, #1 = R); (#8 = T, #11 = R; #11 = T, #8 = R); (#1 = T, #11 = R, #11 = T, #1 = R). First, the S_0 mode results are presented (Figure 39 through Figure 41). Then, the A_0 mode results are presented (Figure 42 through Figure 44). Examining the paired signals presented in Figure 39 through Figure 44, it can be concluded that reciprocity is

verified, since the a) and b) signals in every figure always seem identical. There are no apparent differences in the time of arrival or in the amplitude of the received signal when one sensor was used as transmitter or as receiver. This proves the reciprocity relation for this PWAS installation for both S_0 and A_0 modes of the Lamb wave.

5.3.2.1. Results for the S_0 mode

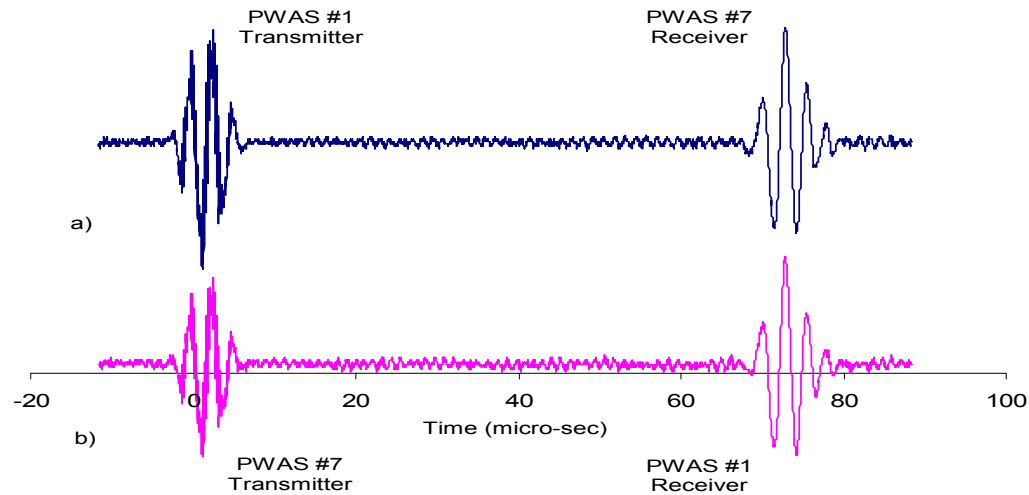


Figure 39 Transmitted and received S_0 mode Lamb wave: (a) PWAS #1 was used as a transmitter and PWAS #7 was the receiver; (b) PWAS #7 was used as a transmitter and PWAS #1 was the receiver

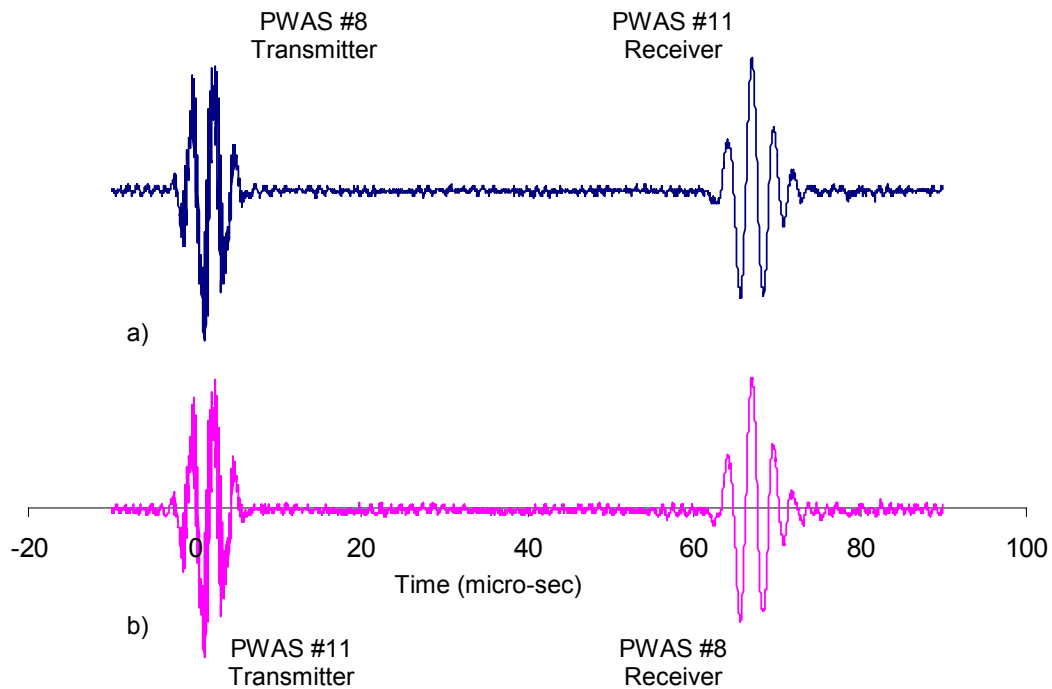


Figure 40 Transmitted and received S_0 mode Lamb wave: (a) PWAS #8 was used as a transmitter and PWAS #11 was the receiver; (b) PWAS #11 was used as a transmitter and PWAS #8 was the receiver

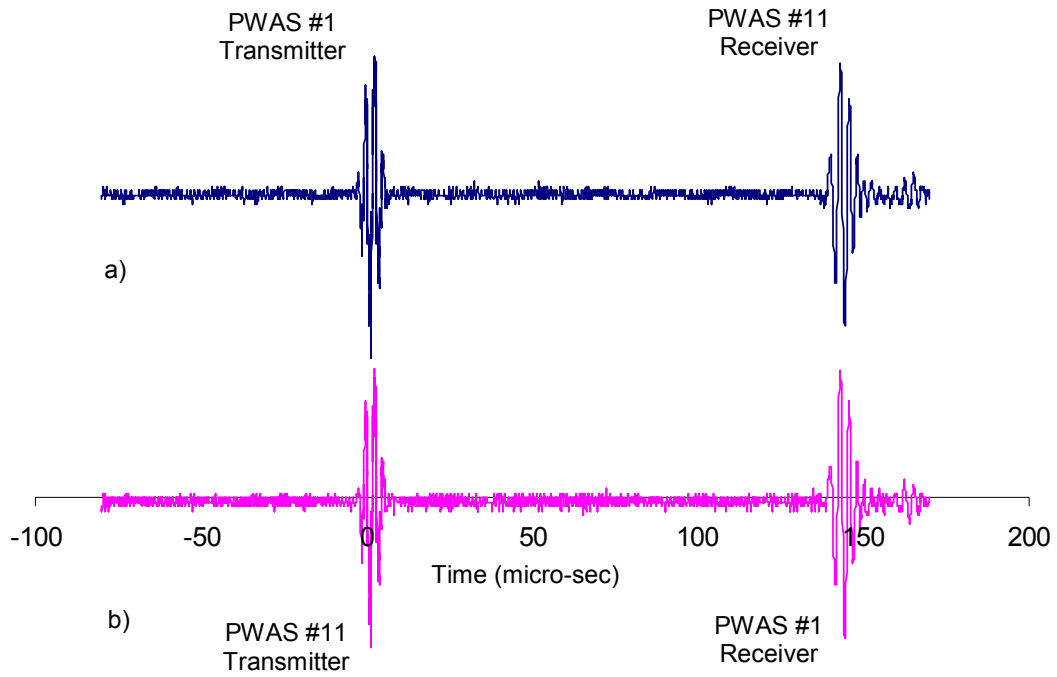


Figure 41 Transmitted and received S_0 mode Lamb wave: (a) PWAS #1 was used as a transmitter and PWAS #11 was the receiver; (b) PWAS #11 was used as a transmitter and PWAS #1 was the receiver

5.3.2.2. Results for the A_0 mode

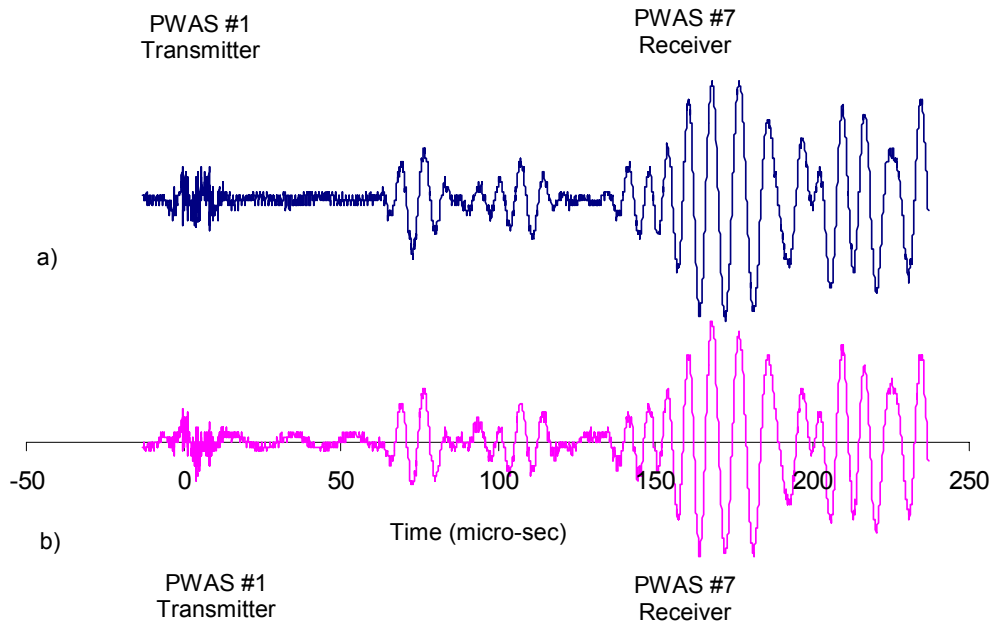


Figure 42 Transmitted and received A_0 mode Lamb wave: (a) PWAS #1 was used as a transmitter and PWAS #7 was the receiver; (b) PWAS #7 was used as a transmitter and PWAS #1 was the receiver

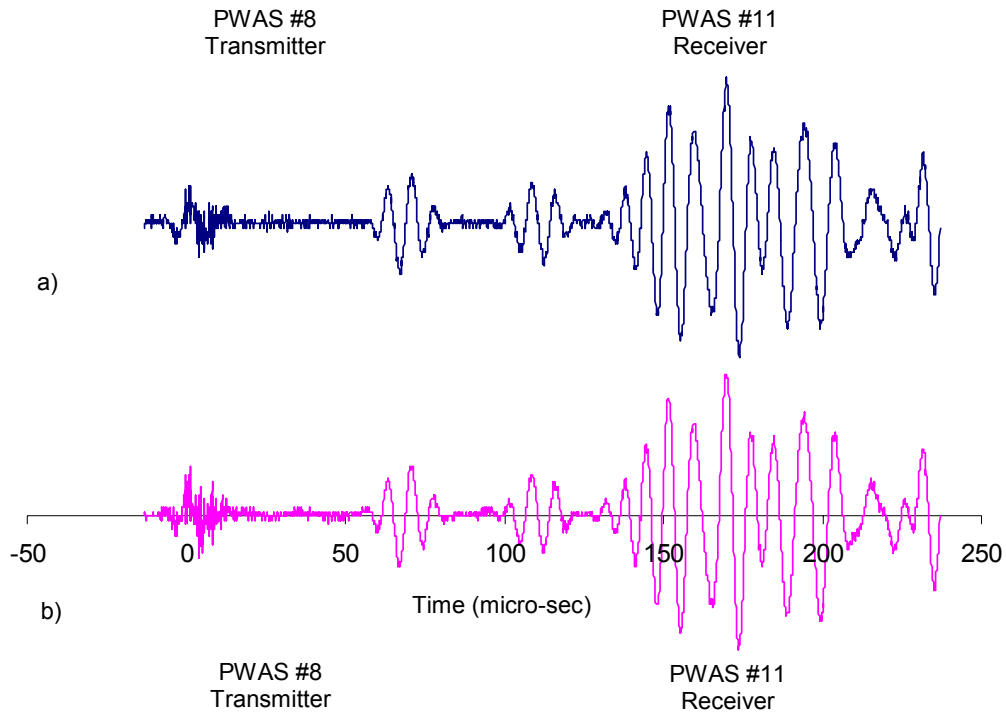


Figure 43 Transmitted and received A_0 mode Lamb wave: (a) PWAS #8 was used as a transmitter and PWAS #11 was the receiver; (b) PWAS #11 was used as a transmitter and PWAS #8 was the receiver

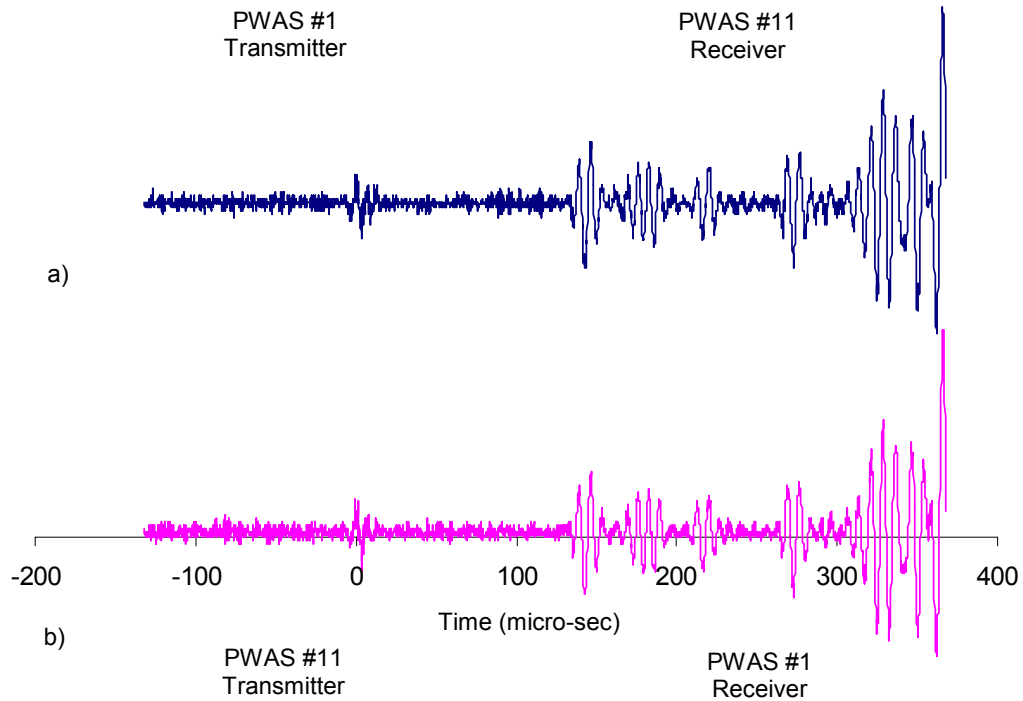


Figure 44 Transmitted and received A_0 mode Lamb wave: (a) PWAS #1 was used as a transmitter and PWAS #11 was the receiver; (b) PWAS #11 was used as a transmitter and PWAS #1 was the receiver

5.4. SUBTASK 2.4 – MODELING AND SIMULATION FOR DETECTION OF CORROSION USING LAMB WAVES

5.4.1. Methods, Assumptions, and Procedures

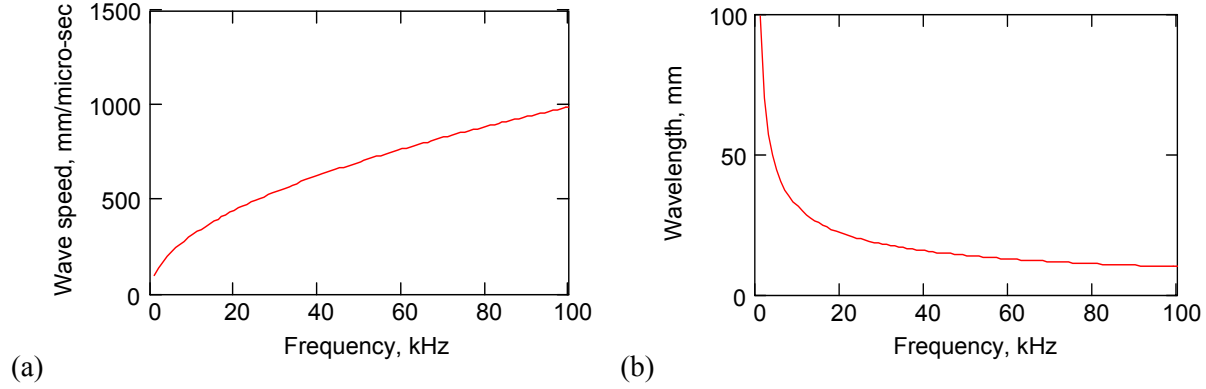


Figure 45 Dispersion characteristics of A_0 Lamb wave mode in 1-mm 2024-T3 aluminum plate: (a) A_0 wave speed vs. frequency; (b) A_0 wavelength vs. frequency

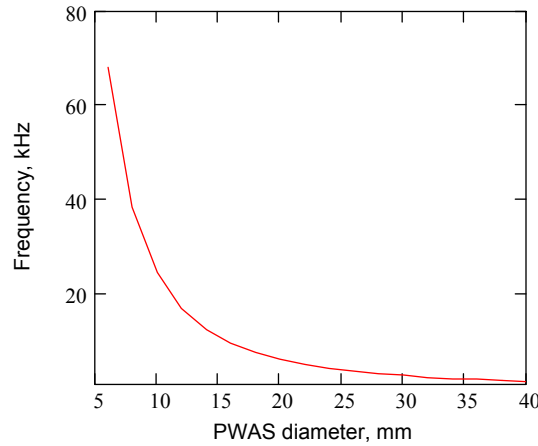


Figure 46 Variation of tuned excitation frequency with PWAS diameter for A_0 Lamb wave mode

In the analysis, the excitation of the A_0 Lamb wave mode which, at low frequencies, resembles flexural plate waves. The highly dispersive characteristic of A_0 flexural waves makes them very sensitive to small changes in plate thickness, as expected during the corrosion process. Figure 45 shows the calculated dispersion characteristics of the A_0 Lamb mode in a 1-mm 2024-T3 aluminum plate in the 1 to 100 kHz band. It is noticed that the wave speed and wavelength vary rapidly with frequency in this low frequency band. For tuned excitation with a 10-mm PWAS, we are looking for wavelength of the order of 20 mm. Figure 45b indicates that a 20-mm wavelength of the A_0 mode would be encountered in the 20–40 kHz range. A more precise determination of the PWAS tuning frequency is given in Figure 46, which shows that the 10-mm diameter PWAS would have an A_0 Lamb-mode optimal tuning frequency of around 30 kHz. Fine tuning experiments described in a later section of this paper have found the exact tuning frequency of 31.5 KHz. The difference between the theoretical prediction and experimental results is attributable to the 2-D effects, which were not captured in this 1-D analysis.

The dispersive propagation of the A_0 Lamb-wave mode was analyzed using the Fourier transform method. The excitation consisted of a 3.5-count Hanning windowed smoothed tone burst of frequency $f_0 = 31.5$ kHz starting at time t_0 and lasting for the duration T :

$$p(t) = \begin{cases} e^{i\omega_0 t} \cos^2\left(\pi \frac{t-t_m}{T}\right), & \text{if } t_0 \leq t \leq t_0 + T \\ 0 & \text{otherwise} \end{cases} \quad (32)$$

where $\omega_0 = 2\pi f_0$. The tone burst duration was calculated in terms of the number of counts, $N_{counts} = 3.5$ using the expression:

$$T = \frac{N_{counts}}{f_0} \quad (33)$$

The excitation was transformed to the frequency domain using the Fourier transform:

$$\tilde{p}(f) = \int_{-\infty}^{+\infty} p(t) e^{-i\omega t} dt \quad (34)$$

In the frequency domain, the excitation was multiplied with the wave transfer function (Doyle, 1997):

$$G(k(\omega), x) = e^{-ik(\omega) \cdot x} \quad (35)$$

to generate the frequency domain response:

$$\tilde{u}(\omega, x) = p(\omega) \cdot G(\omega, x) \quad (36)$$

The frequency-dependent wave number $k(\omega)$ of Equation (35) was calculated using the low-frequency approximation of the A_0 wave speed, i.e.,

$$k(\omega) = \left[\frac{3\rho(1-\nu^2)}{d^2 E} \right]^{1/4} \cdot \omega^{1/2} \quad (37)$$

Applying the inverse Fourier transform to Equation (36), we obtained the A_0 mode Lamb wave response as a function of time, t , and location in the plate, x , i.e.,

$$u(t, x) = \frac{1}{2\pi} \int_{-\infty}^{+\infty} \tilde{u}(\omega, x) e^{i\omega t} d\omega \quad (38)$$

5.4.2. Results and Discussions

Figure 47 presents the simulation of the A_0 mode Lamb wave response at the PWAS source, $x = 0$, and at distances $x = 250\sqrt{2}$ and $x = 500\sqrt{2}$ mm from the PWAS source. It is apparent that, as the distance from

the source increases, the dispersion of the A_0 mode Lamb wave packet increases. Figure 48 presents the effect of plate thickness variation on the wave packet dispersion. Under consideration is a wave packet starting at $r_0 = 0$ and arriving at location $r_1 = 250\sqrt{2}$ (Figure 48a) while traveling through pristine plate, or at $r_{1-\text{cor}} = 250\sqrt{2}$ (Figure 48b) while traveling through corroded plate that has experienced, on average, a thickness reduction of 25%. Comparison of Figure 48a with Figure 48b reveals that the effect of corrosion slows the wave packet down and to increase its dispersion. We notice that the packet traveling through the pristine region seems to reach its peak amplitude at around 280 micro-sec, while the packet traveling through the region with 25% average corrosion seems to reach its peak amplitude at around 320 micro-sec. This 40 micro-sec delay represents an average increase of 13% in travel time. Results similar to these predictions are to be found in the experimental section of this paper.

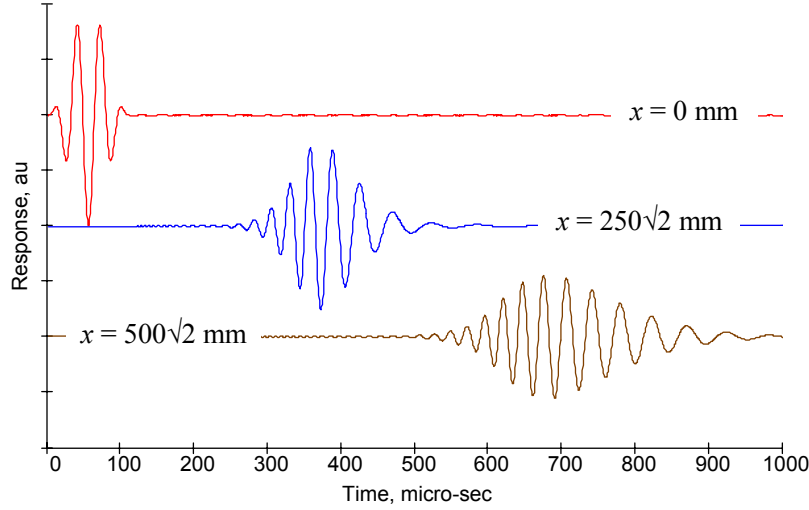


Figure 47 Simulation of A_0 mode Lamb wave response at $x = 250\sqrt{2}$ and $500\sqrt{2}$ mm from the PWAS source placed at $x = 0$ mm (3.5-count smoothed tone burst of 31.5 kHz, plate thickness $h = 1$ mm)

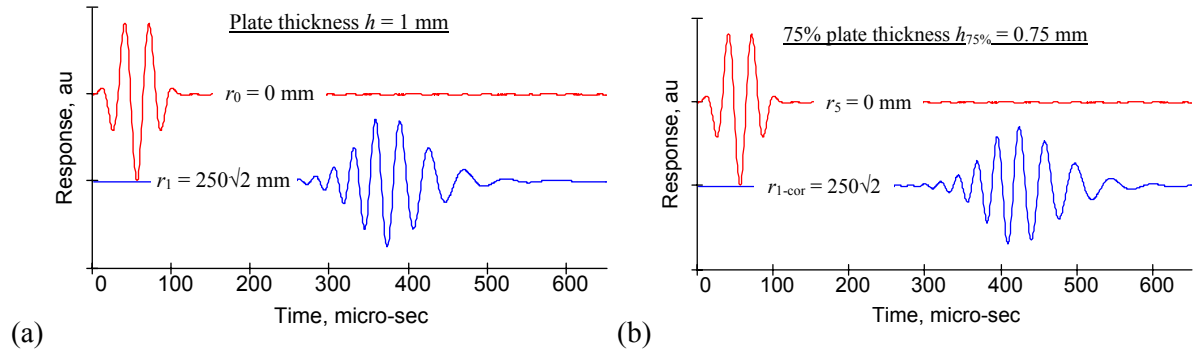


Figure 48 Simulation of A_0 Lamb wave mode response at $250\sqrt{2}$ mm from the PWAS source for two plate thickness values: (a) $h = 1$ mm; (b) $h_{75\%} = 0.75$ mm (3.5-count smoothed tone burst of 31.5 kHz)

Figure 49 presents signal cross plots between the signal simulated for a pristine plate (“pristine signal”) and the signal simulated for a corroded plate (“corroded signal”). These plots are very sensitive to small shifts in signal phase. Two charts are presented, one for 0.5% total material loss (Figure 49a) and one for 1.0% total material loss (Figure 49b). In each chart, two plots are made: first, a plot of the pristine signal on itself, which results in a straight 45° line; second, a plot of the corroded signal against the pristine signal. This second plot results in an ellipse. By comparing Figure 49a with Figure 49b we observe that

the width of the ellipse correlates with the simulated corrosion intensity. For mild corrosion (0.5% total material loss), the ellipse is relatively slim (Figure 49a). For more intense corrosion, (1.0% total material loss) the ellipse is much wider. These results indicate that the signal cross plots can be effectively used to identify the signal phase shifts and dispersions due to the presence of corrosion.

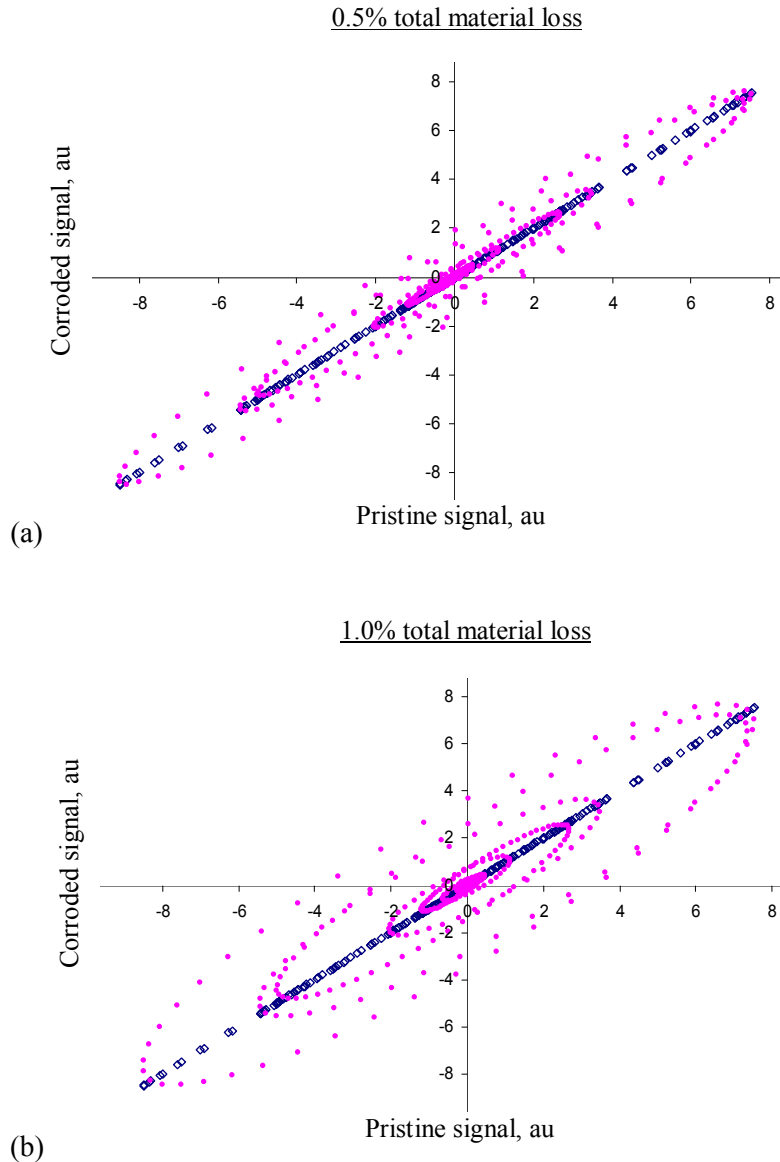


Figure 49 Cross plot between the pristine and corroded signals: (a) 0.5% total material loss; (b) 1% total material loss

5.5. TASK 2 - CONCLUSIONS

The purpose of Task 2 was to find the optimum design for the PWAS. PWAS can be used in many ways for structural health monitoring and non-destructive evaluation, but if the design of the PWAS is not optimized, the effectiveness and performance of the PWAS can be compromised.

In this task we started with the study of the Lamb waveforms and surface displacements for various material properties and geometries (thickness, size, etc). Theoretical predictions of the PWAS' interaction with Lamb waves were used as a starting base for optimizing the design and performance of future health monitoring systems. We identified the effect of frequency and sensor size/shape on the sensor effectiveness. These are important parameters that contribute to the design of a good health monitoring system.

Mode tuning software simulation was developed to be able to selectively tune into specific Lamb modes. It has been observed in separate studies that the detection of through-the-thickness cracks with the pulse-echo method is much better with the S_0 mode than with the A_0 mode. On the other hand, the A_0 mode seems to be better suited for the detection of delaminations, disbonds, and corrosion with the pitch-catch acousto-ultrasonics techniques. The mode-tuning software developed in this task facilitates the optimum design of PWAS transducers to achieve the desired damage detection results.

Modeling using MATLAB and MathCAD was used to simulate the Lamb waves and predict their behavior. This modeling was used to find the optimum PWAS design for various applications. The sensor design criteria were tested experimentally. In our experiments we verified the reciprocity of PWAS Lamb wave transmission and reception and determined that optimum tuning into A_0 and S_0 Lamb wave modes can be achieved. The signals predicted by the theoretical modeling behaved similar to the signals measured in the actual test. This can be used to optimize the sensor design by understanding how the waves behave during their travel in the plate material. Comparative presentation of predicted and measured signals indicated that a reliable prediction method has been obtained that can be used for optimum sensor design.

6. TASK 3: STEERING-BEAM LARGE AREA COVERAGE

This task will extend the preliminary work done on embedded ultrasonic structural radar (EUSR). To date, the EUSR concept has been used to demonstrate the use of the scanning beam to detect:

- 20 mm horizontal crack at 90° (broadside location, i.e. vertical above the array)
- 20 mm horizontal crack at 135° (offside location, i.e. to the left of the array)

Both cracks were positioned at a radial distance of 300 mm from the array. Thin-plate specimens 1220-mm sq., 1-mm thick 2024 T3 were used. In the new tests, we plan to achieve the following: examine multiple cracks; the effect of crack orientation; the effects of crack size and imaging large cracks; and the effects of curvature – theoretically, guided waves are able to propagate in a plate with small curvature and verify this for various curvatures and identify the severe cases.

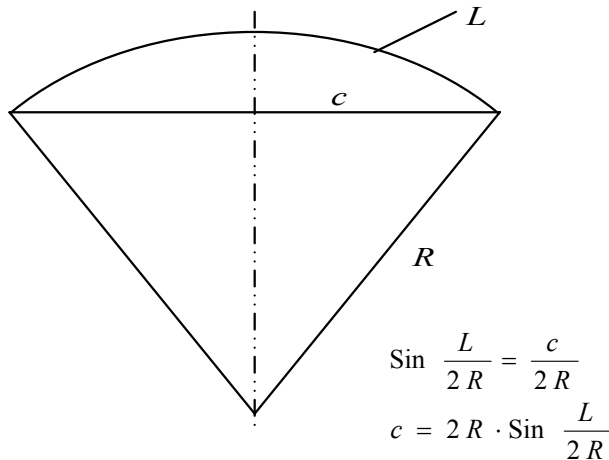
Task Overview

- Subtask 3.1 – EUSR With Curvature
- Subtask 3.2 – The Effects of Crack Orientation and Multiple Targets on EUSR
- Subtask 3.3 – Automatic Signal Acquisition

6.1. SUBTASK 3.1 – EUSR WITH CURVATURE

6.1.1. Methods, Assumptions, and Procedures

Experiments were done on specimens with three different extents curvature. To facilitate the experiments, the extent of curvature was defined by L , the difference between the original length L and the chord c , see Figure 50 below. We went through 5mm, 10mm, 15mm and 20mm to cover the three extents.



| R | c | $dL=L-c$ |
|-----------|---------|----------|
| 100.00E+3 | 1219.99 | |
| 50.00E+3 | 1219.97 | |
| 20.00E+3 | 1219.81 | |
| 10.00E+3 | 1219.24 | |
| 8.80E+3 | 1219.02 | 1 |
| 5.00E+3 | 1216.98 | |
| 3.90E+3 | 1215.03 | 5 |
| 2.75E+3 | 1210.02 | 10 |
| 2.24E+3 | 1204.98 | 15 |
| 2.00E+3 | 1201.17 | |
| 1.95E+3 | 1200.20 | 20 |
| 1.00E+3 | 1145.73 | |

$L = 1220$, all dim. mm

Figure 50 – Curvature of the specimen

During the process to set up the curvature, it was discovered that there could be two types of curvature on the square plate. One is parallel to the PWAS array; the other is perpendicular to the PWAS array. The

parallel PWAS array will be called ‘direction 1’ and the perpendicular PWAS array will be called ‘direction 2’ (Figure 51).

6.1.2. Results and Discussions

In the experiments, both directions were tested to verify that guided waves are able to be used as the propagating wave since its propagation is confined within the structure or material. Therefore the curvature should not affect the detectability of embedded ultrasonic structural radar (EUSR).

According to the experimental results, it was concluded that generally the curvature will not affect the efficiency of EUSR detectability.



Figure 51 – Two types of curvature: a) direction 1, parallel to the PWAS array; b) direction 2, perpendicular to the PWAS array.

6.1.2.1. Experiment with 0 curvature

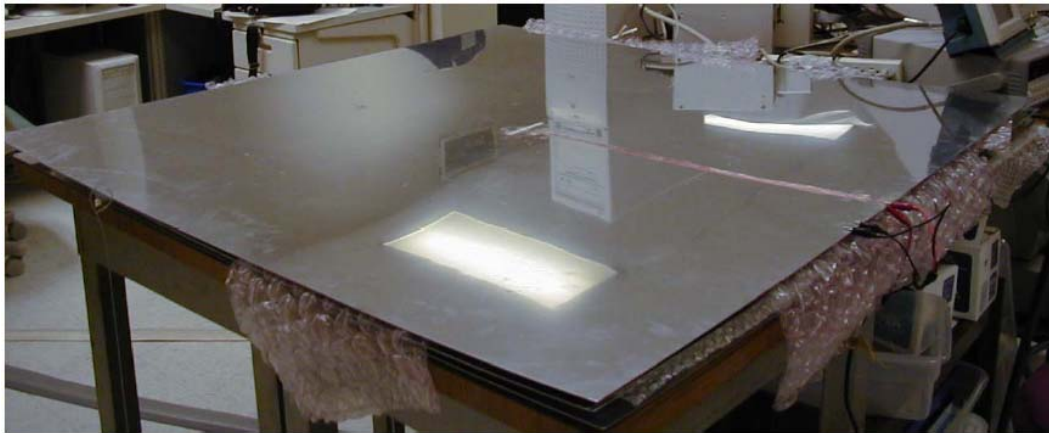


Figure 52 – Experiment with 0 curvature

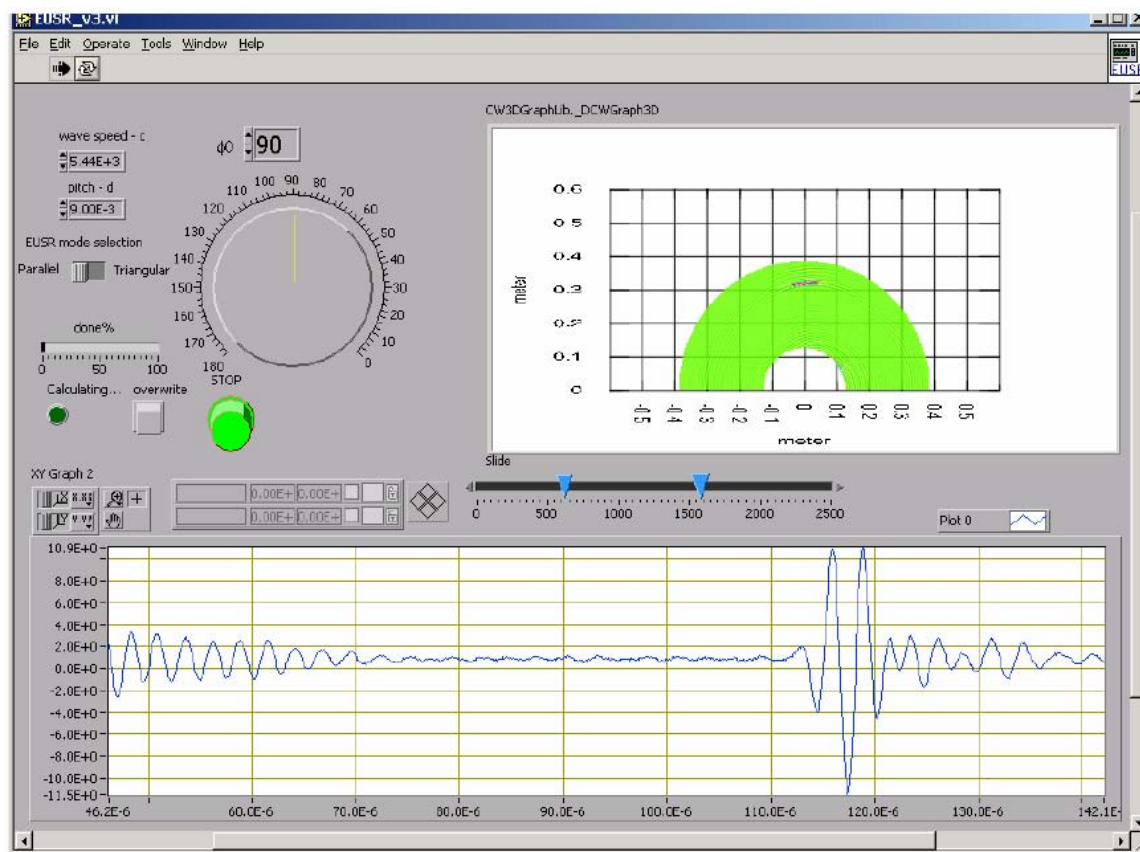


Figure 53 – EUSR analysis for 0 curvature

6.1.2.2. Experiment with 5mm shortening (Curvature radius $R = 3900$ mm) in direction 1

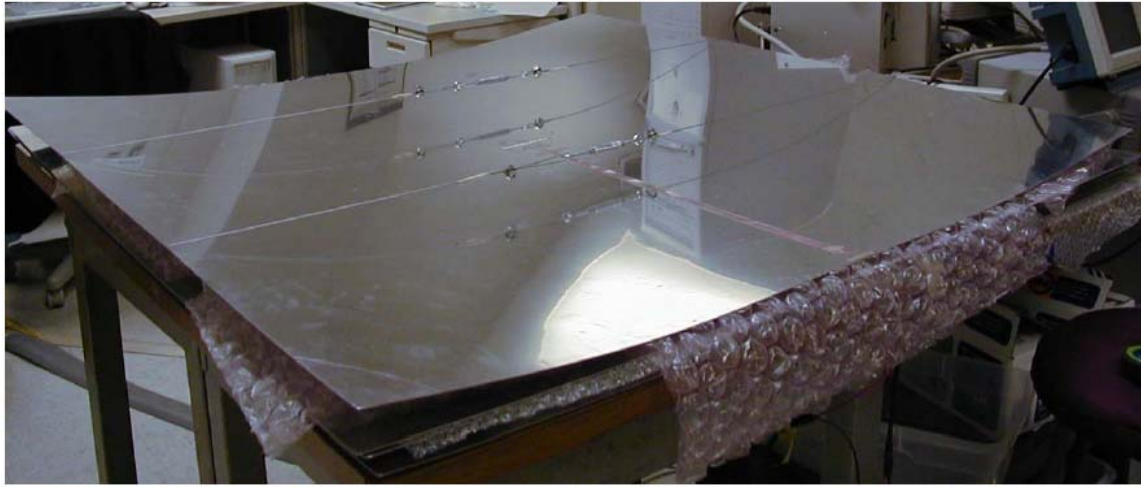


Figure 54 – Experiment with 5mm curvature at direction 1

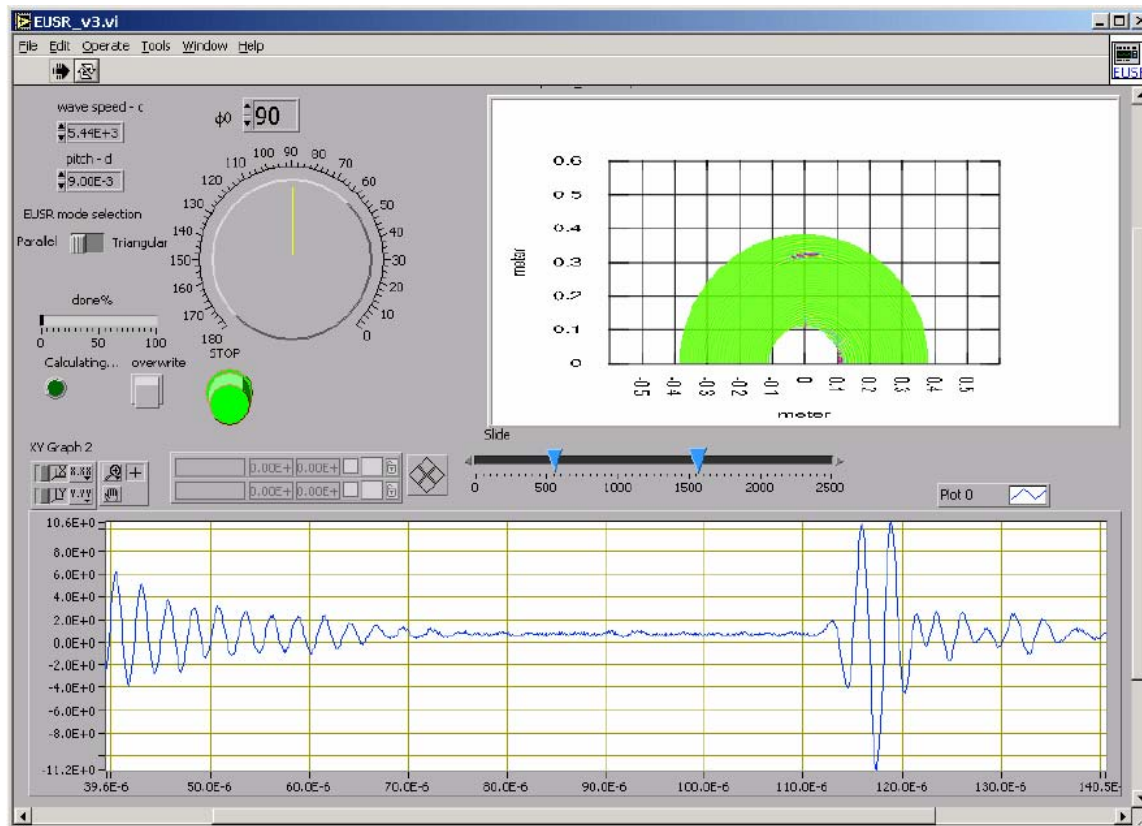


Figure 55 – EUSR analysis for 5mm curvature at direction 1

6.1.2.3. Experiment with 10mm shortening (curvature radius $R = 2750$ mm) in direction 1



Figure 56 – Experiment with 10mm curvature at direction 1

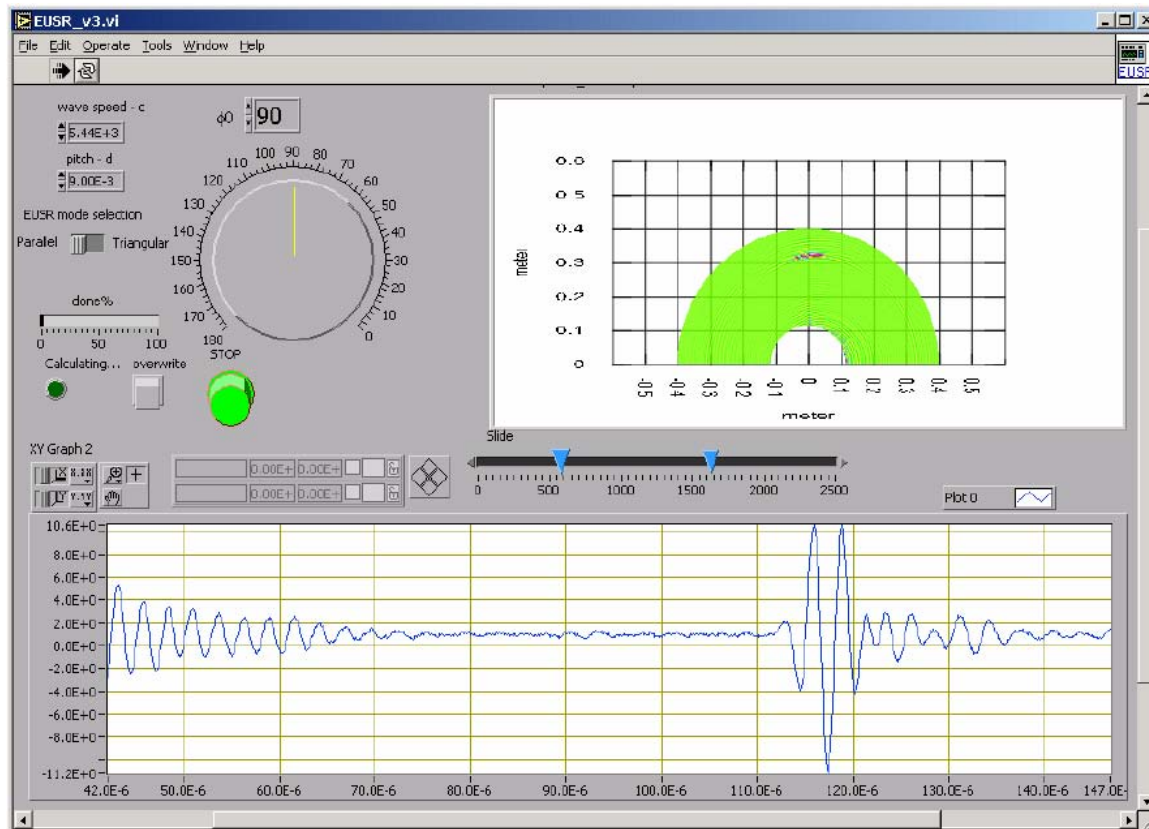


Figure 57 – EUSR analysis for 10mm curvature at direction 1

6.1.2.4. Experiment with 15mm shortening (curvature radius $R = 2240$ mm) in direction 1



Figure 58 – Experiment with 15mm curvature at direction 1

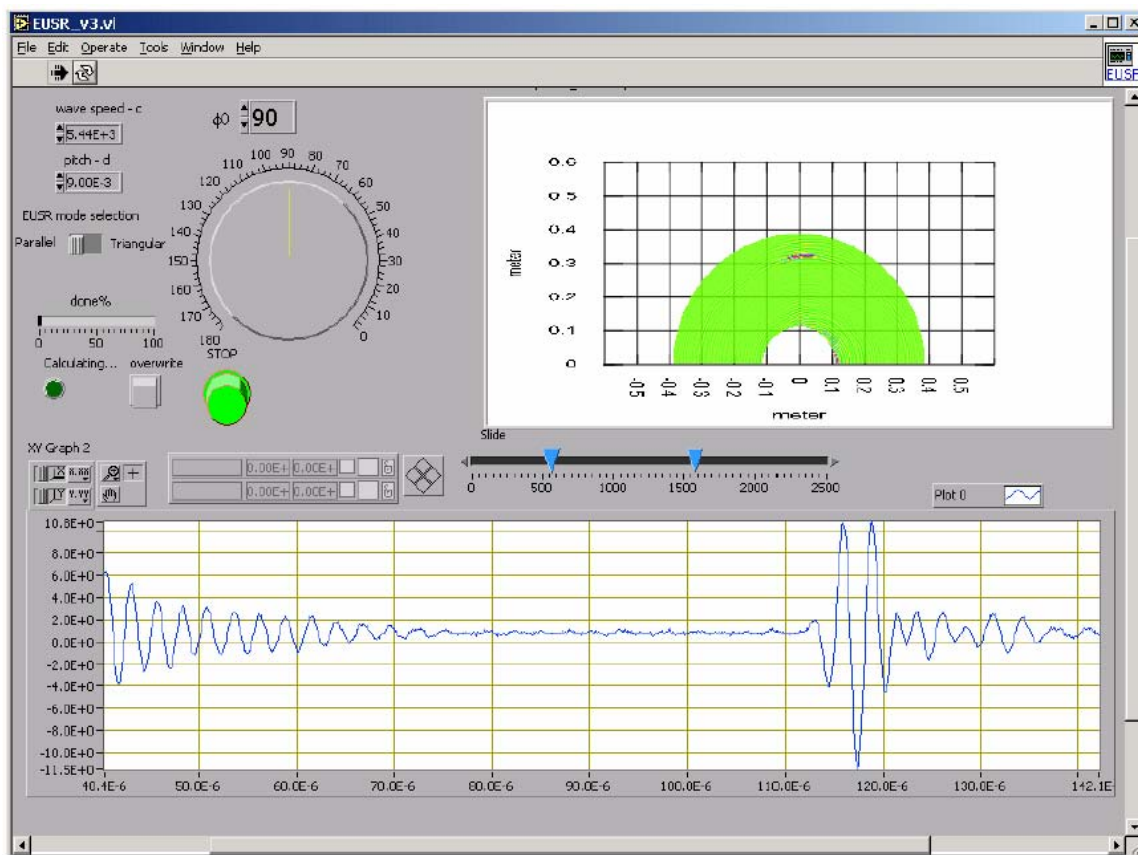


Figure 59 – EUSR analysis for 15mm curvature at direction 1

6.1.2.5. Experiment with 20mm shortening (curvature radius $R = 1950$ mm) in direction 1



Figure 60 – Experiment with 20mm curvature at direction 1

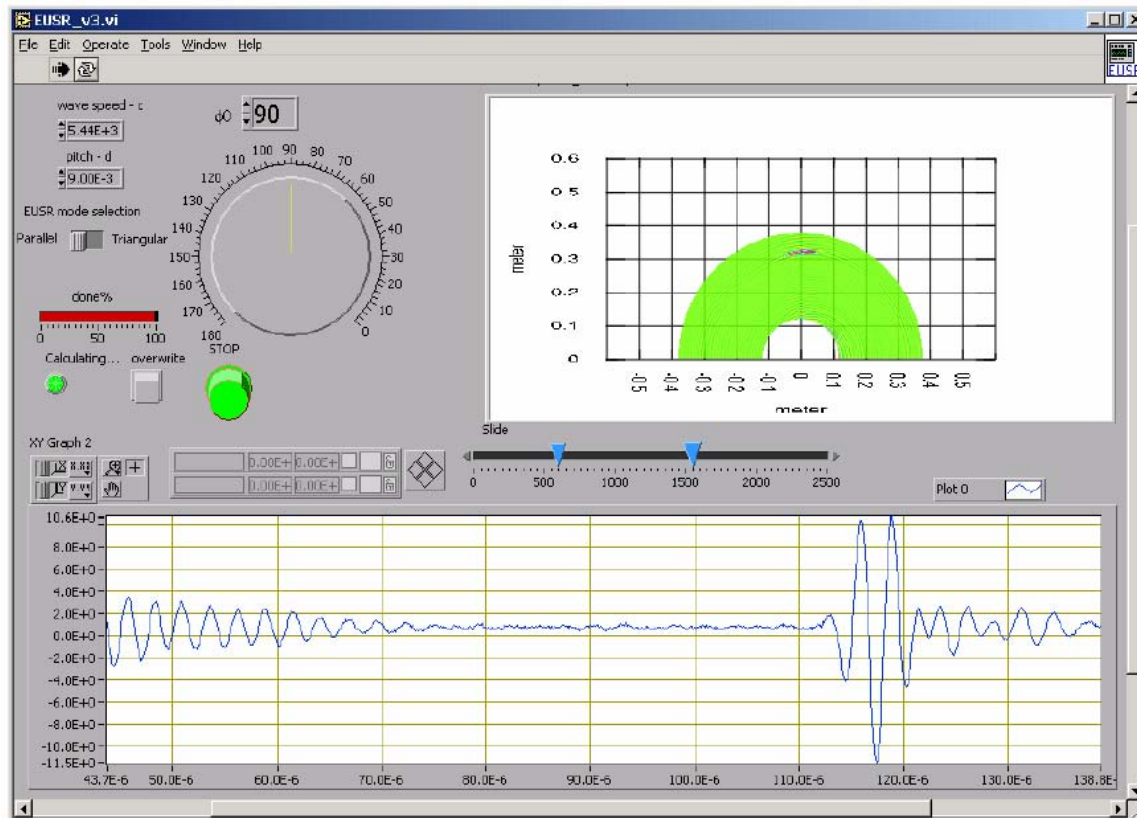


Figure 61 – EUSR analysis for 20mm curvature at direction 1

6.1.2.6. Experiment with 5mm shortening (curvature radius $R = 3900$ mm) in direction 2

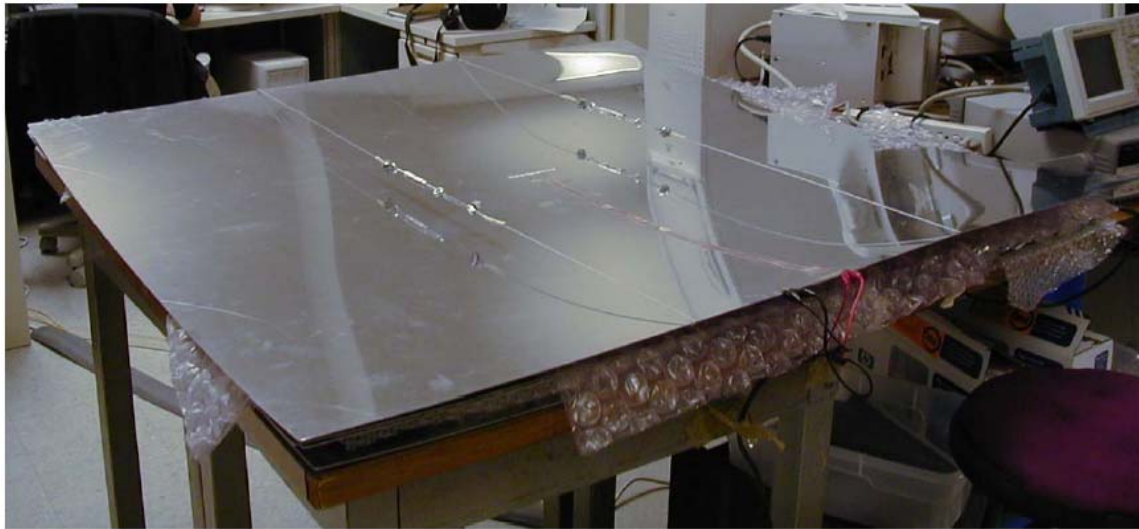


Figure 62 – Experiment with 5mm curvature at direction 2

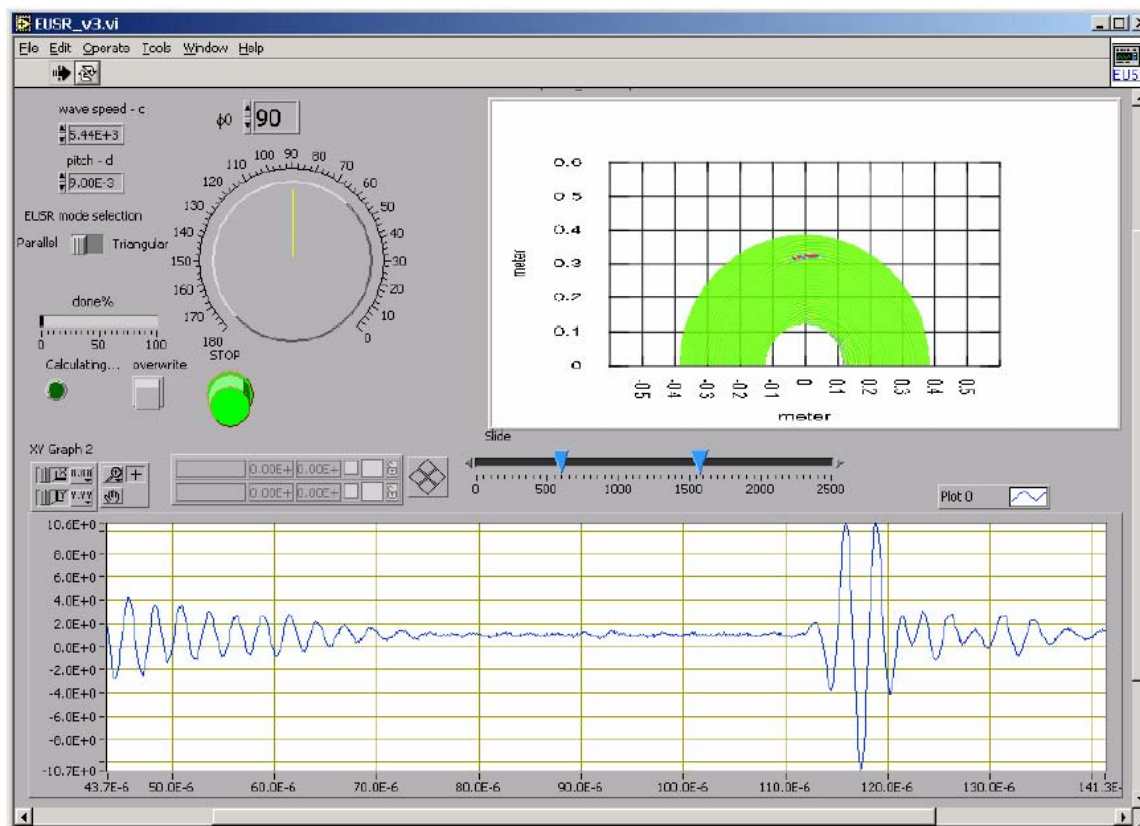


Figure 63 – EUSR analysis for 5mm curvature at direction 2

6.1.2.7. Experiment with 10mm shortening (curvature radius $R = 2750$ mm) in direction 2



Figure 64 – Experiment with 10mm curvature at direction 2

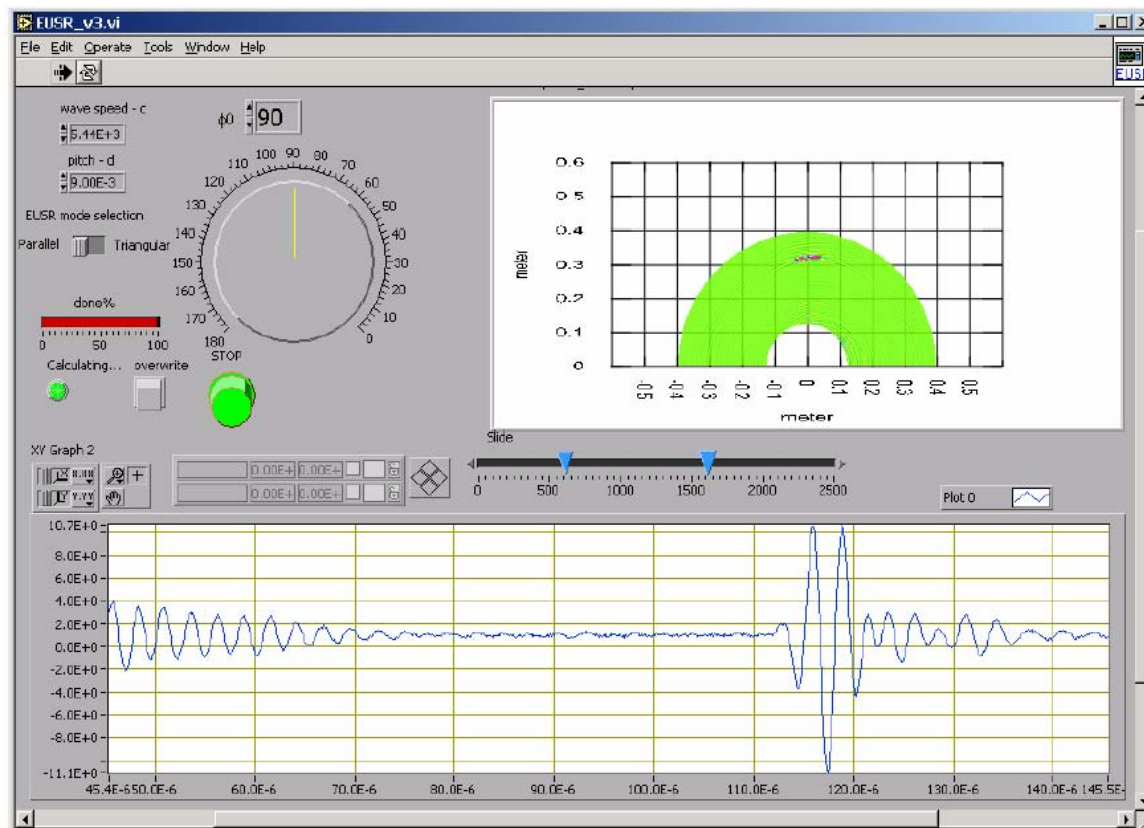


Figure 65 – EUSR analysis for 10mm curvature at direction 2

6.1.2.8. Experiment with 15mm shortening (curvature radius $R = 2240$ mm) in direction 2



Figure 66 – Experiment with 15mm curvature at direction 2

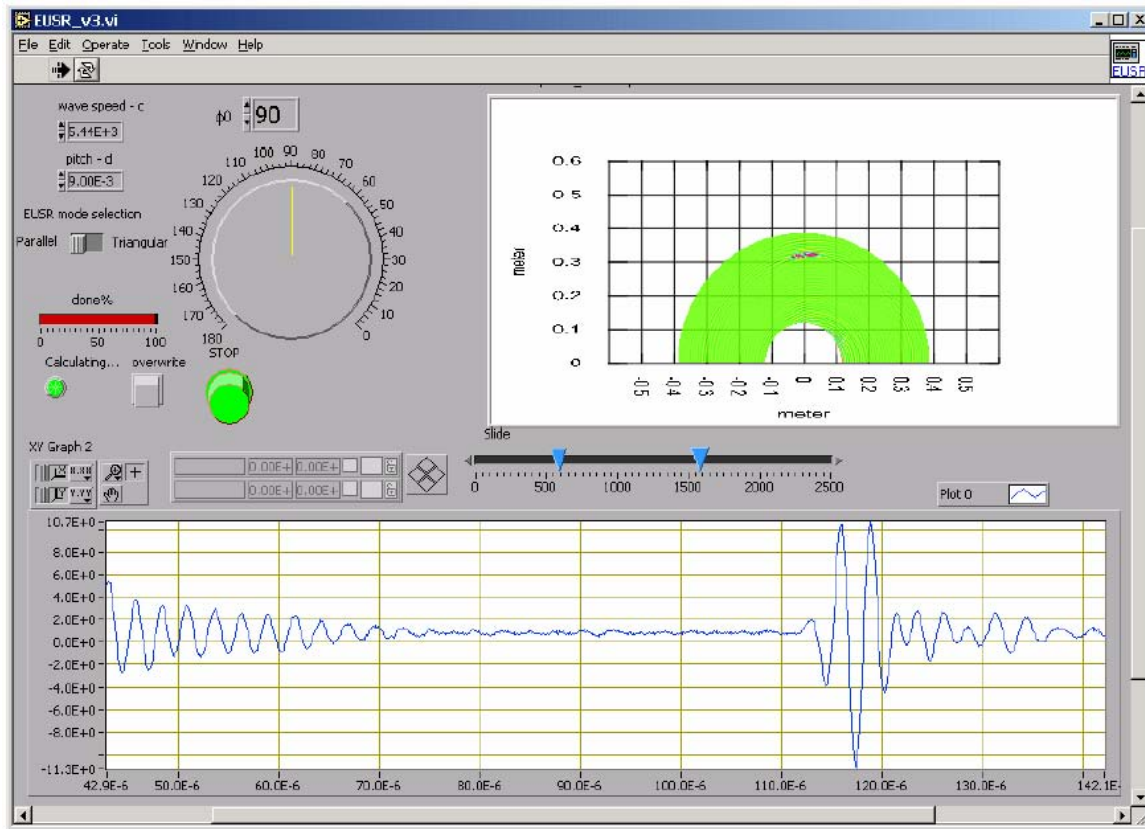


Figure 67 – EUSR analysis for 15mm curvature at direction 2

6.1.2.9. Experiment with 20mm shortening (curvature radius $R = 1950\text{mm}$) in direction 2



Figure 68 – Experiment with 20mm curvature at direction 2

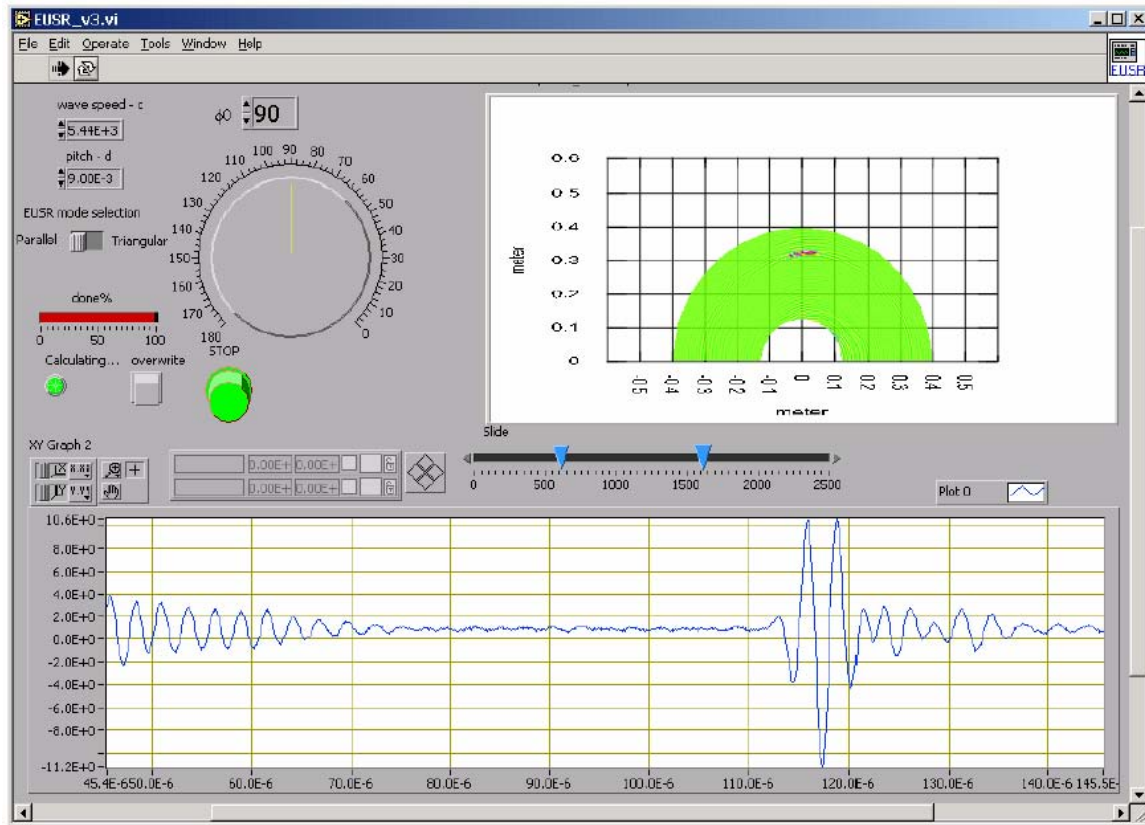


Figure 69 – EUSR analysis for 20mm curvature at direction 2

6.2. SUBTASK 3.2 – THE EFFECTS OF CRACK ORIENTATION AND MULTIPLE TARGETS ON EUSR

6.2.1. Methods, Assumptions, and Procedures

6.2.1.1. The Embedded Ultrasonic Structural Radar (EUSR) Algorithm and Previous Work

The principle of operation of the embedded ultrasonic structural radar (EUSR) is derived from two general principles: (1) The principle of guided Lamb wave generation with piezoelectric wafer active sensors (PWAS); (2) The principles of conventional phased-array radar.

The guided Lamb waves generated by PWAS have the important property that they stay confined inside the walls of a thin-wall structure, and hence can travel over large distances. In addition, the guided wave can also travel inside curved walls, which makes them ideal for applications in the ultrasonic inspection of aircraft, missiles, pressure vessel, oil tanks, pipelines, etc. This was proved by curvature experiment. Lamb waves can exist in a number of dispersive modes. However, through smoothed tone-burst excitation and frequency tuning, it is possible to confine the excitation to a particular Lamb wave mode, of carrier frequency f_c , wave speed c , and wave length $\lambda = c/f_c$. Hence, the smoothed tone-burst signal generated by one PWAS is of the form:

$$s_T(t) = s_0(t) \cos 2\pi f_c t \quad (39)$$

where $s_0(t)$ is a short-duration smoothing window that is applied to the carrier signal of frequency f_c between 0 and t_p .

The principles of conventional phased-array radar are applied to the PWAS-generated guided waves, assuming a uniform linear array of M sensors (PWAS), with each PWAS acting as a point wise omni-directional transmitter and receiver. The PWAS in the array are spaced at the distance d , which is assumed much smaller than the distance r to a generic, far-distance point, P . Since $d \ll r$, the rays joining the sensors with the point P can be assimilated with a parallel fascicle, of angle ϕ . Therefore, for the m^{th} PWAS, the distance will be shorted by $m(d \cos \phi)$. If all the PWAS are fired simultaneously, the signal from the m^{th} PWAS will arrive at P quicker by $\Delta_m(\phi) = m(d \cos \phi)/c$. Yet, if the PWAS are not fired simultaneously, but with some individual delays, δ_m , $m = 0, 1, \dots, M-1$, then the total signal received at point P will be:

$$s_P(t) = \frac{1}{\sqrt{r}} \sum_{m=0}^{M-1} s_T \left(t - \frac{r}{c} + \Delta_m(\phi) - \delta_m \right) \quad (40)$$

$1/r$ represents the decrease in the wave amplitude due to the omni-directional 2-D radiation, and r/c is the delay due to the travel distance between the reference PWAS ($m = 0$) and the point P . (Here wave-energy conservation, i.e., no dissipation, is assumed.)

Transmitter beam forming: if we have $\delta_m = m\Delta(\phi)$, then Equation (40) becomes:

$$s_P(t) = M \cdot \frac{1}{\sqrt{r}} s_T \left(t - \frac{r}{c} \right) \quad (41)$$

That's to say, there is an M times increase in the signal strength with respect to a simple sensor. This leads directly to the beam forming principle that if $\delta_m = md \cos(\phi_0)/c$, and since $\Delta_m = md \cos(\phi)/c$, then constructive interference (beam forming) takes place when $\cos(\phi) = \cos(\phi_0)$, i.e. at angles $\phi = \phi_0$

and $\phi = -\phi_0$. Thus, the forming of a beam at angles ϕ_0 and $-\phi_0$ is achieved through delays in the firing of the sensors in the array.

Receiver beam forming: if the point P is an omni-directional source at azimuth ϕ_0 , then the signals received at the m^{th} sensor will arrive quicker by $m\Delta_0\phi = md \cos(\phi_0)/c$. Hence, we can synchronize the signals received at all the sensors by delaying them by:

$$\delta_m(\phi_0) = m \frac{d}{c} \cos(\phi_0) \quad (42)$$

Pulse-echo method: Assume that a target exists at azimuth ϕ_0 and distance R . The transmitter beam former is sweeping the range in increasing angles ϕ and receives an echo when $\phi = \phi_0$. The echo will be received on all sensors, but the signals will not be synchronized. To synchronize the sensors signals, the delays $\delta_m(\phi_0) = md \cos(\phi_0)/c$ need to be applied.

The original signal is:

$$s_P(t) = \frac{M}{\sqrt{R}} s_T \left(t - \frac{2R}{c} \right) \quad (43)$$

At the target, the signal is backscattered with a backscatter coefficient, A . Hence, the signal received at each sensor will be:

$$\frac{A \cdot M}{R} s_T \left(t - \frac{2R}{c} + \Delta_m(\phi) \right) \quad (44)$$

The receiver beam former assembles the signals from all the sensors with the appropriate time delays:

$$s_R(t) = \frac{A \cdot M}{R} \sum_{m=0}^{M-1} s_T \left(t - \frac{2R}{c} + \Delta_m(\phi) - \delta_m \right) \quad (45)$$

Constructive interference between the received signals is achieved when $\delta_m = md \cos(\phi_0)/c$. Thus, the assembled receive signal will be again boosted M times, with respect to the individual sensors:

$$s_R(t) = \frac{A \cdot M^2}{R} \sum_{m=0}^{M-1} s_T \left(t - \frac{2R}{c} \right) \quad (46)$$

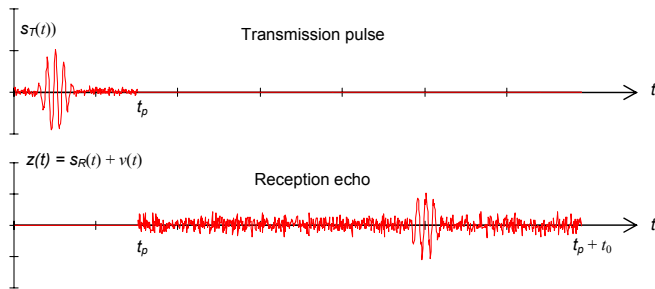


Figure 70 the transmitted signal and the received signal

In general, a target crack is unknown, i.e. the target location is unknown. Since we use the polar coordinates in the radar system, the location of an unknown target is defined by the angle ϕ_0 . The coarse estimation of ϕ_0 is implemented by using the ϕ_0 sweeping method. EUSR will scan through 0° to 180° by incrementing ϕ_0 by 1° each time, until the maximum received energy is obtained. $\max E_R(\phi_0)$ is the maximum received energy by the definition:

$$E_R(\phi_0) = \int_{t_p}^{t_p+t_0} |s_R(t, \phi_0)|^2 dt \quad (47)$$

Figure 70 is an example of the transmitted signal and received signal pair captured in our experiment. The specimens we used in the lab are 4-feet long, 1-mm thick square aluminum plates with an 8-element PWAS array at the center. The layout is shown in Figure 71 (a). Figure 71 (b) is the experiment setup.

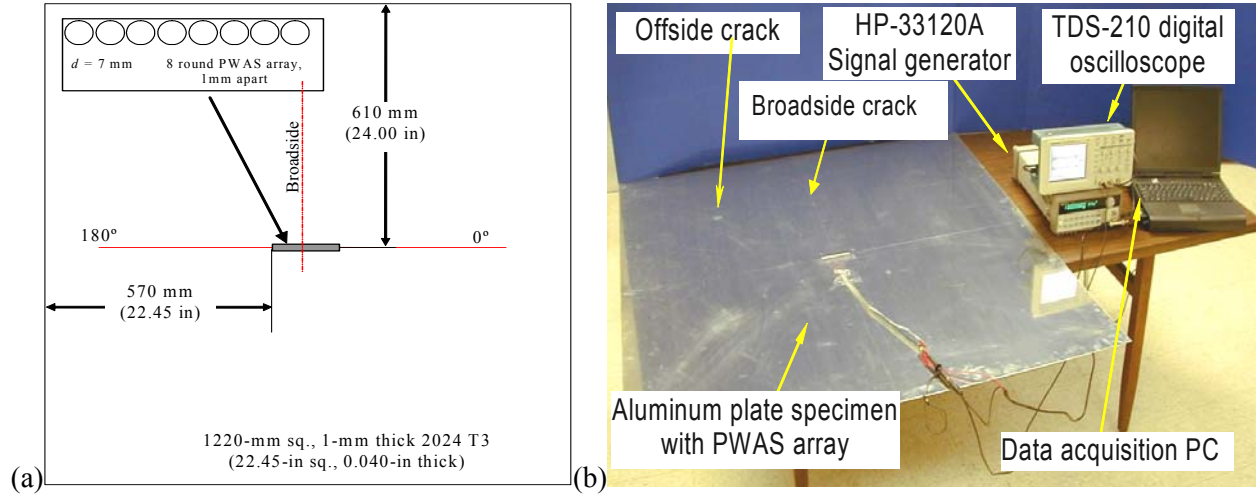


Figure 71 EUSR experiment with the 8 element PWAS array: (a) specimen layout; (b) experiment setup

In the experiment, broadside position is defined to be perpendicular to the PWAS array and offside position is anywhere between the 0° and 180° but the broadside position. The cracks are simulated by through-plate cracks 14mm long and 0.5mm wide.

Previous proof-of-concept work has been done by using EUSR to verify its ability for detecting a single crack at either broadside or offside position on a thin-plate specimen. Figure 72 (b) and Figure 73 (b) are the 2D display of single crack inspection by using our previous EUSR. The offside position is angle 137° .

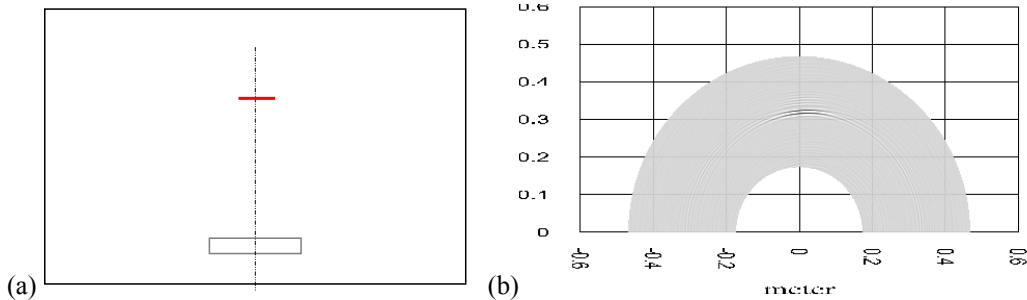


Figure 72 single broadside crack detection with previous EUSR: (a) schematic; (b) EUSR GUI mapped image

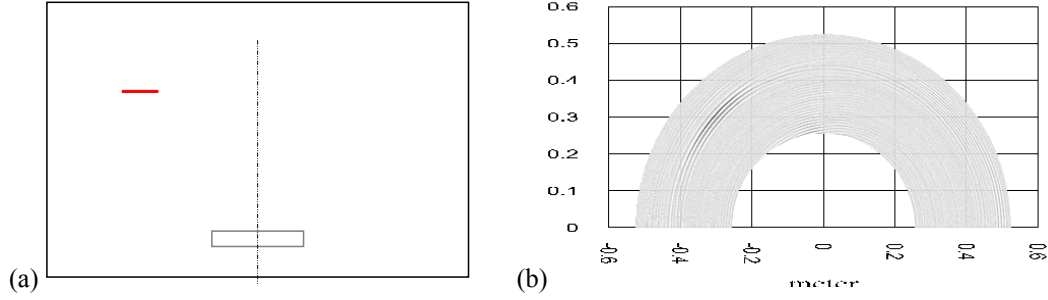


Figure 73 single offside crack detection with previous EUSR: (a) schematic; (b) EUSR GUI mapped image

6.2.1.2. An Improved EUSR by using the Hilbert Transform

From the specimen inspection plots, it was determined that they can generally locate the damage; they are far than close to the real cracks. A solution to improve the image quality and precision was needed to be developed. It was noticed that echoes from the damage do not have single peaks due to the dispersion property or some reasons. Something had to be done to get the echoes close to the theoretical ones, having single peaks. The method that was explored was the Hilbert transform, which is able to extract the envelope of a curve.

The envelope is a curve or surface that is tangent to every one of a family of curves or surfaces. Envelope extracts the amplitude of a periodic signal. It can be used to simplify the process of detecting the time of arrival for the wave packets in our EUSR system. In the EUSR, the envelope of the signal is extracted by applying Hilbert transform to the cross correlation signal.

The Hilbert transform is defined as:

$$H(x(t)) = -\frac{1}{\pi} \int_{-\infty}^{+\infty} \frac{x(\tau)}{t - \tau} d\tau \quad (48)$$

Hilbert transform can also be used to construct a complex signal:

$$\tilde{x}(t) = \tilde{x}_{\text{Re}}(t) + i \cdot \tilde{x}_{\text{Im}}(t) \quad (49)$$

Where

$$\begin{aligned} \tilde{x}_{\text{Re}}(t) &= x(t) \\ \tilde{x}_{\text{Im}}(t) &= H(x(t)) \end{aligned} \quad (50)$$

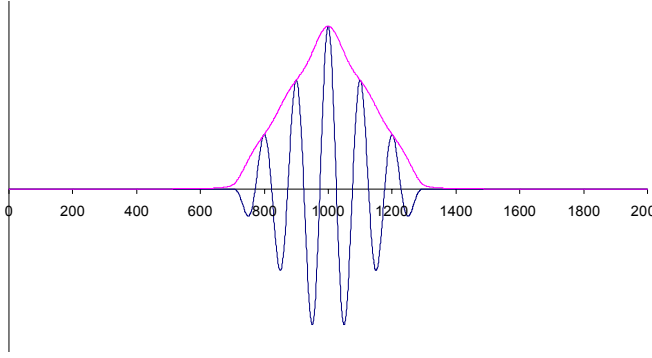


Figure 74 a tone-burst signal and its envelope extracted by using Hilbert transform

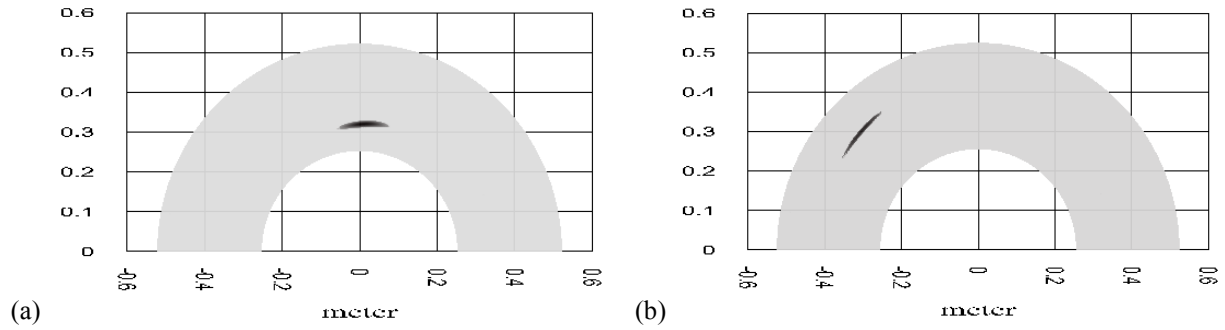


Figure 75 – single crack detection with the improved EUSR: (a) broadside crack detection; (b) offside crack detection

The real part of the constructed signal, $\tilde{x}_{\text{Re}}(t)$, is the original data $x(t)$, while the imaginary part $\tilde{x}_{\text{Im}}(t)$ is the Hilbert transform of $x(t)$. Actually, the imaginary part is a version of the original real sequence after a 90° phase shift. Thus, the Hilbert transformed signal has the same amplitude and frequency content as the original real signal and includes phase information that depends on the phase of the original signal. The magnitude of each complex value has same the amplitude as the origin signal. Therefore, the magnitude of the analytical signal is the envelope of the original signal. Just by observing the envelope signal, the wave packages can be easily recognized. Figure 74 is an example showing the envelope extracted after applying the Hilbert transform.

The processing results show that this process can result in a more distinct representation of echoes from the crack and therefore a more clear indication of the crack. Compared with Figure 73, Figure 75 shows results of the inspection of the crack detection with better resolution and more close to the crack real size. Meanwhile, the new cracks inspection has fewer disturbances from the side-lobe effects.

Therefore, the Hilbert transform will be apply after the EUSR algorithm in order to extract the envelopes of the reconstructed EUSR signals such that an echo can be created with a single peak. Figure 76 shows the data flow of the EUSR.

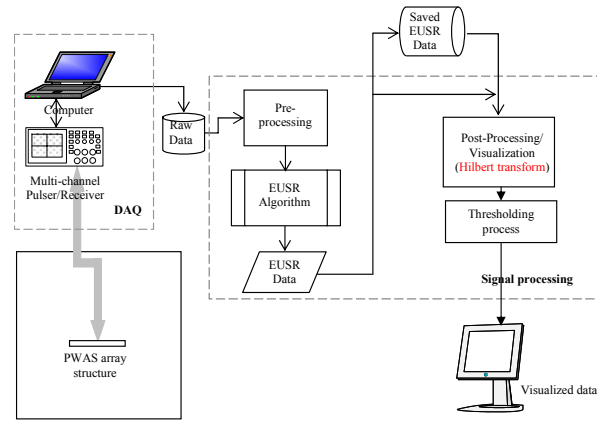


Figure 76 – data flow of the damage detection by using the improved EUSR algorithm

6.2.1.3. EUSR multi-crack detection experiments

The previous work has proved EUSR's ability to detect a single through plate crack in a thin plate. The new experiments are designed to verify EUSR is also able to detect multiple cracks. The following experiments were performed:

- Broadside crack with certain slope
- Two aligned offside cracks
- Three aligned cracks, two offside cracks and one horizontal broadside crack
- Three aligned cracks, two offside cracks and one perpendicular broadside crack

6.2.2. Results and Discussions

6.2.2.1. Broadside Crack with Certain Slope

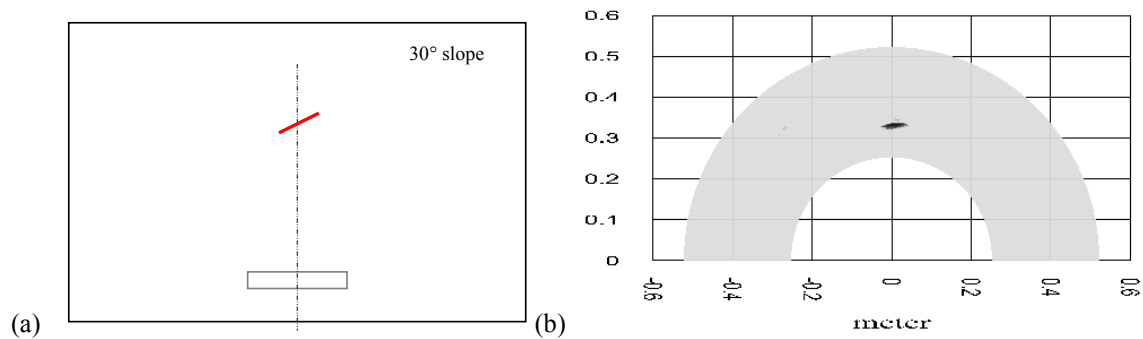


Figure 77 – the broadside crack having 30° slope: (a) schematic; (b) EUSR 'GUI mapped image

The specimen #7 has a broadside crack with the 20-mm crack dimension, but 30° to the horizontal. The experiment result in Figure 77 shows that EUSR is able to indicate the slope. The plot is different from the horizontal crack showing in Figure 75 a). In the future, further experimentation will be done to find out the minimum slope that EUSR is sensitive and able to indicate, and compare the results of different slopes.

6.2.2.2. Two aligned offside cracks

The specimen #6 has two symmetrical offside cracks at 63° and 117° positions, respectively. Figure 78 shows the EUSR inspection result.

One thing has to be mentioned is, for some reason, the two cracks are actually not exactly symmetrical to each other as the original design. They are 3 mm from each vertically. However, the 2D inspection plot picked out such a difference, and it is shown that the two cracks are in different circles (having different vertical distance to the PWAS array). It can be concluded that the EUSR is able to even pick up that small difference (Figure 78).

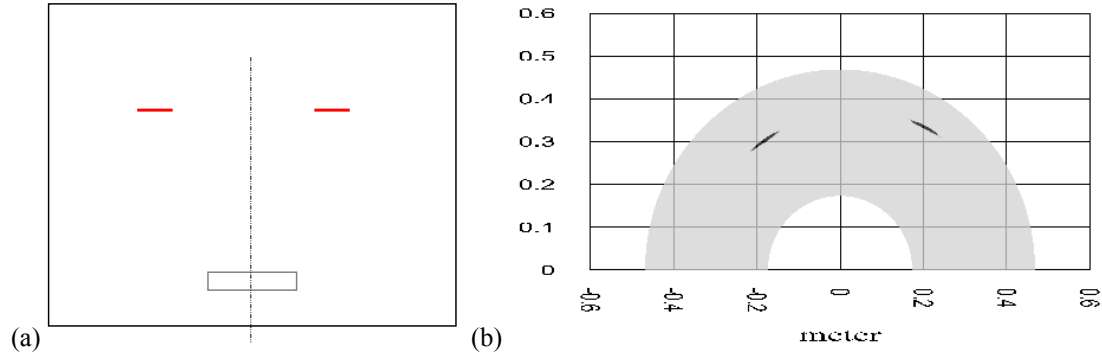


Figure 78 – the two symmetrical offside cracks at 63° and 137° , respectively: (a) schematic; (b) EUSR GUI mapped image

6.2.2.3. Next Step: Three Aligned Cracks

In the three aligned cracks experiments, two designs were created. Both designs have two offside horizontal cracks at 63° and 137° positions. Design 1 has a broadside crack parallel to the PWAS array while design 2 has a broadside crack perpendicular to the PWAS array (Design 1: the horizontal broadside crack and Design 2: the vertical broadside crack).

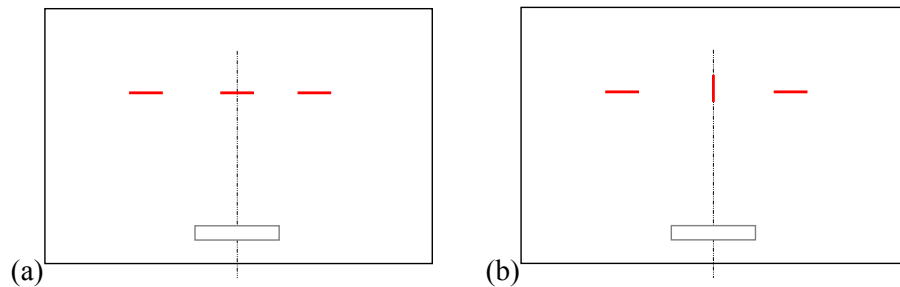


Figure 79 – three aligned cracks: (a) schematic of the horizontal broadside crack; (b) schematic of the vertical broadside crack

To this moment, EUSR algorithm is able to detect the presence of the three cracks in the A-scan signal, but not in the mapped EUSR image for the three cracks experiments. The reason for this may be that the broadside crack reflects more energy than the offside cracks and therefore the energy reflected from the perpendicular crack dominates the EUSR image. For the design 2, recalling the result attained from the pin-hole experiments (Task 4), the minimum hole size that can be detected by EUSR is 1.57 mm. Therefore the crack in the design 2 may be too tiny to be detected.

In the next stage, the signal processing techniques will be applied and signal analysis methods will be used to improve the results. The vertical crack will gradually be enlarged to find out the smallest dimension detected and further verify EUSR.

6.3. SUBTASK 3.3 – AUTOMATIC SIGNAL ACQUISITION

6.3.1. Methods, Assumptions, and Procedures

An automatic signal switch is necessary to send the excitation signals to PWAS and acquire the response signal from another PWAS. Such a program-controlled switch can quickly and precisely execute the data collection in a way which is more efficient and reliable than the manual switching operations. The automation of data collection consists of two parts: the hardware part of auto signal switch box and the corresponding software part of PC control program. In this method, digit control signals are generated by the PC software and sent to the switch box through the parallel port. According to the control signals from the parallel port, the switch box will connect the function generator and oscilloscope each to one sensor (these two sensor can be the same) of the PWAS array respectively. Thus, one signal measurement route is constructed, the excitation signal is transmitted to the PWAS array and echo signals are received by the oscilloscope. With this method, the measurement loops are performed automatically under the control of the PC software.

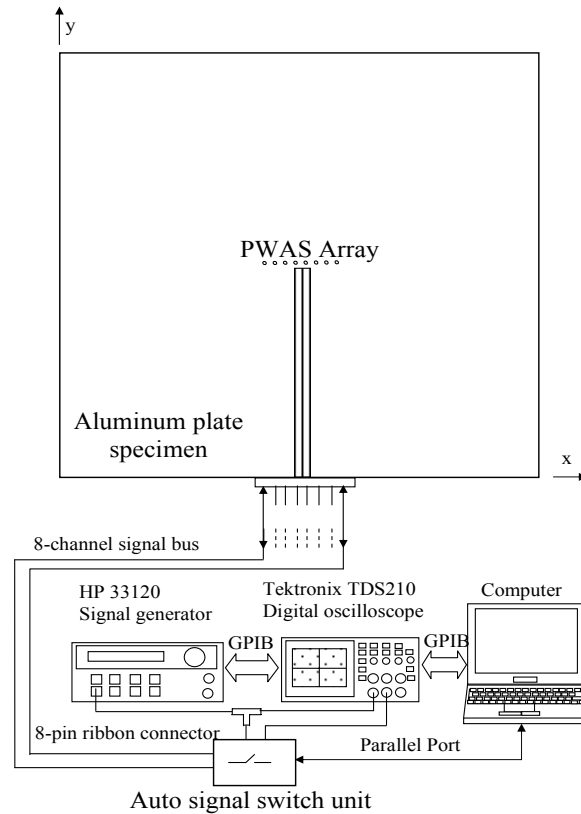


Figure 80 Experimental setup

Figure 80 shows the whole measurement equipments setup. The PWAS array is connected to the switch box with an 8-pin ribbon bus; the function generator and oscilloscope are connected to the switch box with coaxial cables. The switch box is connected to the parallel port of the control PC to receive digit control signals.

The software part, developed in LabVIEW, controls the hardware part. The “out port” function in LabVIEW is used to send digit signals through PC parallel port. This software provides a graphic user interface (GUI) to facilitate the data collection of PWAS array (Figure 81). With the GUI, user can configure the switch unit work in an auto signal acquiring mode in which signal transmitted to and received from assigned sensors can be completed automatically without changing the hardware connection by hand. When the auto switch is in the automatic mode, user will input 2 numbers and the path name. the auto switch will perform the measurement loops that start from the first number until the second number and the data from these measurement loops will be saved in that path; when in manual mode, the auto switch will allow the user to collect data with the transmitting and receiving sensors specified by the two number inputs. After these parameters defined, the control software will send out 8-bit digit signals through parallel port and these signals will then be decoded to control the read-relays.

Two rows of indicating LEDs will be lit in green colors to show which sensor is transmitting excitation signals and which one is used to receive echo signals. During the data collection process, the wave form will also be displayed on this GUI.

The control program is easy to implement and can be integrated into an upper level program that executes the whole task of signal acquisition and analysis. Because of the concise design of the hardware, the concept of the auto signal switch can be extended to other application cases such as the electromechanical (E/M) impedance measurement for SHM.

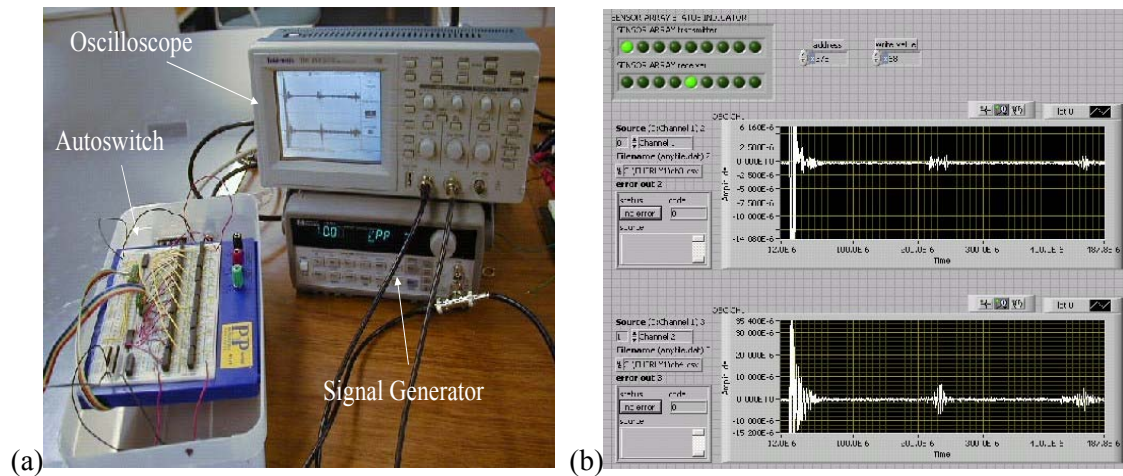


Figure 81 Autoswitch device for automated signal acquisition in the steering beam experiments: (a) experimental setup; (b) graphical user interface of the controlling LabVIEW program

6.4. TASK 3 – CONCLUSIONS

In Subtask 3.1, according to the experimental results, it was concluded that generally the curvature will not affect the efficiency of EUSR detectability. Subtask 3.2 has presented the applications of signal processing techniques to the existing embedded ultrasonic structural radar (EUSR) algorithm using piezoelectric wafer active sensors. After presenting the general principles of the EUSR algorithm and the previous work, a better method was presented (the Hilbert transform) to extract the signal envelopes to improve the efficiency and reliability of existing EUSR. A series of experiments are conducted to verify the EUSR's ability to detect multi-cracks, including: (a) broadside crack with certain slope; (b) two horizontal aligned cracks. The inspection plots of the cracks from the specimens were achieved under monitoring. For the three horizontal aligned cracks with two types of middle crack cases, it is envisioned to apply signal processing techniques and enlarge the vertical crack dimension in our next step coming soon. In Subtask 3.3, the automatic signal switch provided fast data acquisition from arrays and a simple solution for sensor array connection and data collection.

7. TASK 4: PROBABILITY OF DETECTION (POD) WITH PWAS PROBES (AN INITIAL ANALYSIS)

The aging process of commercial and military fleet has generated an increasing attention to nondestructive testing (NDT) methods. Because problems in aging aircrafts are growing faster than the rate at which aircraft age, it is important to transfer these NDT techniques from the laboratory to the aircraft as soon as possible. Part of this transfer is the probability of detection (POD) of anomalies. Before implementing NDT methods on the aircraft it is important to know if the methods can detect anomalies and what would be the efficiency of detection.

One definition of the POD as a function of the damage size is the fraction of damages of a nominal size that are expected to be detected. This can be expressed as a ratio of the probability of detecting damage with a certain confidence interval (usually 90%, 95%). The information obtained in this way is usually presented in a graphical form, where the probability of detection is plotted as a function of the damage size for a fixed confidence interval as presented in Figure 82 (Grills, 2001).

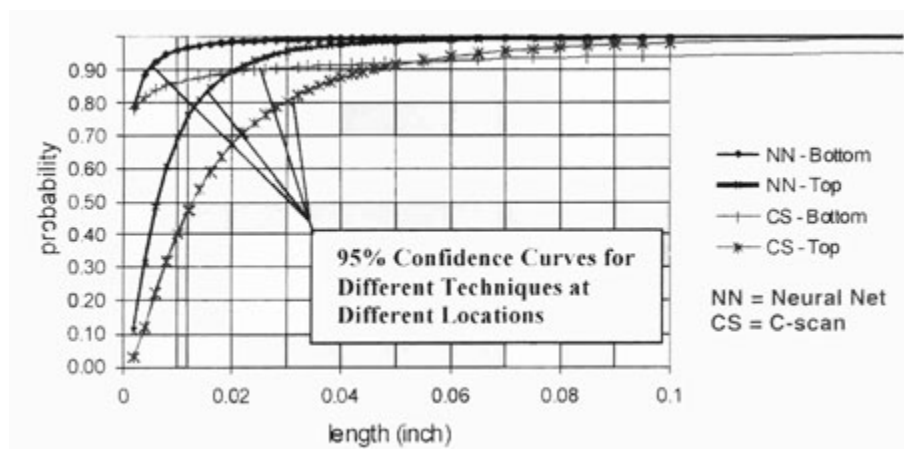


Figure 82 Typical POD Curves (Grills, 2001)

It is also important to keep the probability of false alarm (POFM) below a certain level. A false alarm occurs when an anomaly is detected when in fact there is no anomaly. In real applications it is desired not to miss any damages so, most detection algorithms are set to insure that damage is not missed while keeping the false rate below 1%.

7.1. METHODS, ASSUMPTIONS, AND PROCEDURES

7.1.1. Planning the POD Experiment

The purpose of this work is to identify damage in simulated aircraft panels using piezoelectric wafer active sensors (PWAS). The method under investigation uses ultrasonic principles where PWAS sensors are used to introduce Lamb waves in the structure and also to receive the reflected/transmitted signals. In this way the sensors are used both as a transmitter and a receiver. An array of PWAS sensors will be used to generate an ultrasonic “beam” that will scan the area under investigation. The collected data will then be transferred and stored into a PC where signal processing techniques developed at USC will be used to identify and localize the damage. The key steps when planning the POD experiment are discussed in the next sections.

7.1.1.1. Establish the Type and Size of the Damage to be Detected

The specimen under investigation is a 1220x1220 mm aluminum plate with a thickness of 1 mm. The damage will be simulated by pin-holes of different diameter. The holes will be generated using a hand-

held power drill. We will consider pin-holes with diameters ranging from 0.5mm, 1mm, 1.57mm and 2mm.

7.1.1.2.

7.1.1.3. *Establish the Confidence Interval (CI)*

The probability of detection of a required damage size is correlated to a certain confidence interval, usually 90/95 %. We will consider in our experiment a 95% confidence interval. In this way we want to be sure that we have a high detection probability and also a low false alarm rate.

7.1.1.4. *Orientation of the damage*

This experiment will focus on two locations for the damage. These locations are presented in Figure 83.

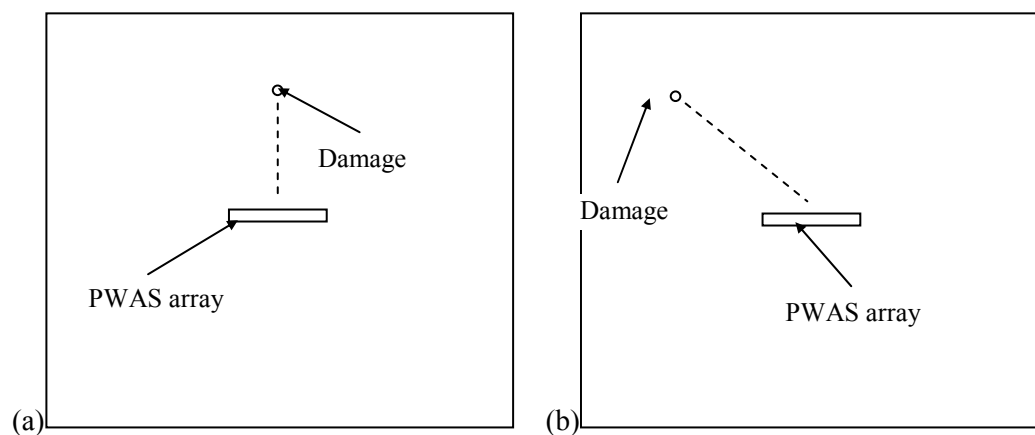


Figure 83 Damage location;(a) Phase one, damage is located perpendicular to the PWAS array; (b) Phase two, damage is located at an angle

7.1.1.5. *Manufacturing the Specimens with and without Damages*

Specimens must contain a distribution of damages, as well as large areas without any damages. Because the real damaged aircraft specimens are expensive to duplicate, artificial methods can be used to create damage such as electrical discharge, machined notches, etc. To manufacture the damaged specimen we will use a hand-held power drill. The specimen without the damage (pristine) consists of an aluminum plate having the same dimensions as the damaged one, but without any holes.

7.1.1.6. *Hardware and Software Testing*

Before starting the actual test, it is important to completely test the hardware and its associated software to insure proper operation. A schematic of the hardware is presented in Figure 84.

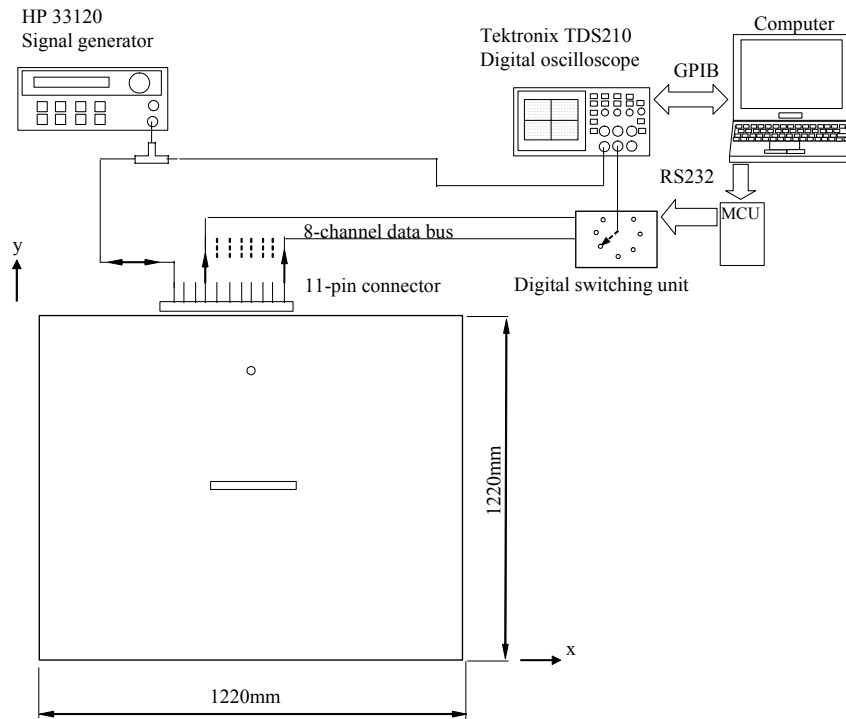


Figure 84 Experimental setup for the POD experiment

7.1.1.7. Documentation of the Experiment

This step refers to keeping track of all the methods applied during the test. It is important to keep track and document all the methods used during the test. This step has a particular importance because for an implementation of the method on an aircraft the approving authority has to approve any procedure that will be used during the test.

7.1.1.8. Environmental Conditions

The POD experiment must be conducted in environmental and physical conditions that are as close as possible to the real conditions. In our initial analysis, we will use standard lab conditions.

7.1.1.9. Calibration Standards

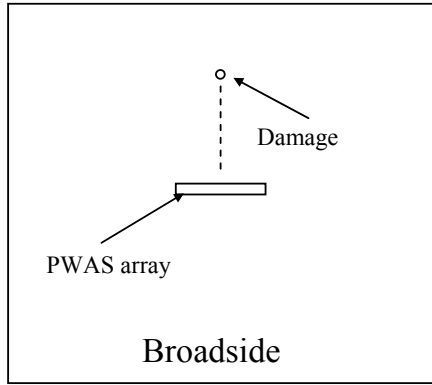
The need for uniform calibration standards is important. By using the same calibration standards the variables introduced by multiple calibration standards are eliminated and increases the level of consistency with the results. Not conducting a POD involves great risks that can not be afforded. Such risks include not finding a critical damage, high rate of falls alarms, or using a wrong technique for damage detection.

7.1.2. PWAS POD Experimental Planning

Detection: PWAS phased array using the EUSR algorithm

Pin-Hole Damage: Induced using small drill bits of increasing size: 0.5 mm, 1 mm, 1.57 mm and 2 mm

Procedure: Start with the smallest drill bit and increase until detection is obtained in broadside location. Repeat for offside location.



(a)



(b)

Figure 85 Tools for the PWAS POD experiment: (a) aluminum plate with a PWAS array and a pin-hole damage of increasing size; (b) set of small drill bits in the size range 0.5mm, 1mm, 1.57mm and 2mm

7.2. RESULTS AND DISCUSSIONS

The ability to detect pin-hole damage using PWAS phased arrays and the EUSR algorithm was tested during this procedure. The purpose was to identify the minimum pin-hole that can be detected. The experiment used pin-hole diameters in the range 0.5 mm, 1 mm, 1.57 mm, and 2 mm.

The experiment showed that the present method cannot detect pin-holes with 0.5 mm and 1 mm, but it can detect the pin hole with 1.57mm diameter. See Figure 86 (a). The tiny dot at the broadside position is the simulation of the pin hole in the 2D plot. The Figure 86 (c) shows the result of the pin-hole with 2mm diameter, which is much clearer than the (b).

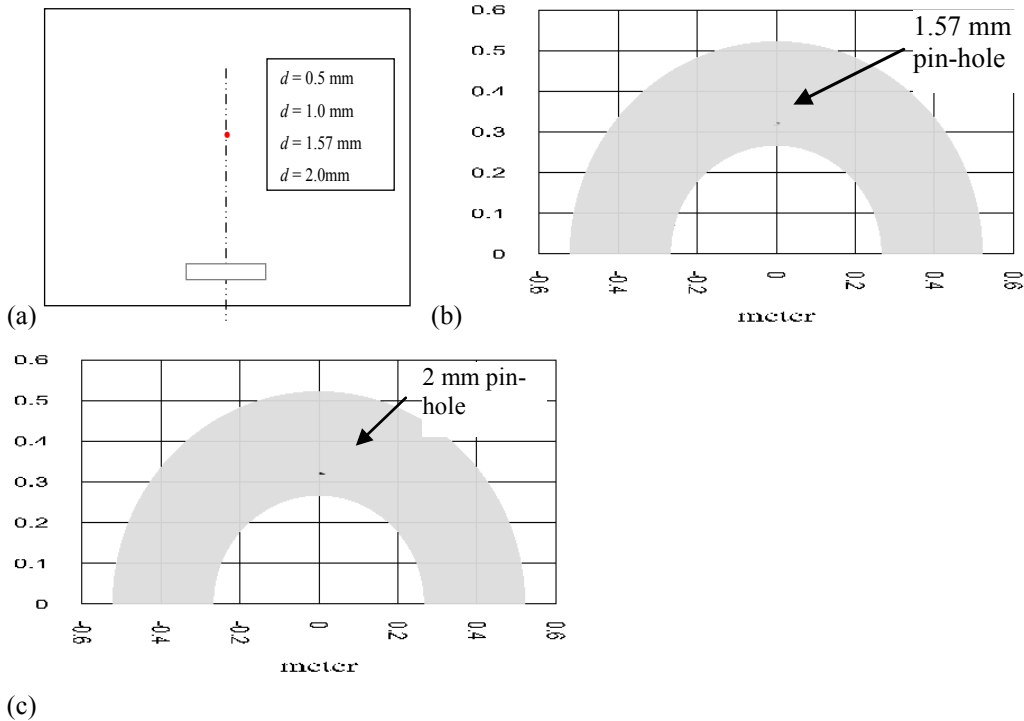


Figure 86 – pin-holes: (a) schematic; (b) EUSR GUI mapped image of the minimum detectable pin-hole with 1.57mm diameter; (c) EUSR GUI mapped image of pin-hole with 2mm diameter

7.3. *TASK 4 – CONCLUSIONS*

In this task we performed an initial POD analysis of the detection of damage using the PWAS technology. A procedure for performing the POD experiments was established. It was also shown that PWAS phased-arrays in conjunction with the EUSR algorithm can detect small pin-hole damage as small as 1.57 mm in a simple plate structure. In the future, this initial analysis can be extended in the following directions:

- (a) refinement of the signal processing algorithm to bring down the detection limit to 1 mm and even 0.5 mm
- (b) extension of the experiment to complicated aerospace structures with multiple constructive features
- (c) comparison of the detection threshold obtained with the present method versus the detection threshold obtained with conventional ultrasonic NDE methods. The comparison should include both detection threshold, on one hand, and duration of test and manpower requirements, on the other hand.

8. REFERENCES

1. Doyle, J. F. (1997) *Wave Propagation in Structures*, Springer Verlag, 1997
2. Giurgiutiu, V. 2003a "Lamb Wave Generation with Piezoelectric Wafer Active Sensors for Structural Health Monitoring", *SPIE's 10th International Symposium on Smart Structures and Materials and 8th Annual International Symposium on NDE for Health Monitoring and Diagnostics*, 2-6 March 2003, San Diego, CA, paper # 5056-17
3. Giurgiutiu, V., 2003b, "Embedded NDE with Piezoelectric Wafer Active Sensors in Aerospace Applications,": *Journal of Materials Special Issue on NDE* , Vol. 55, No. 1
4. Giurgiutiu, V.; Bao, J.; Zhao, W. (2003) "Piezoelectric-Wafer Active-Sensor Embedded Ultrasonics in Beams and Plates", *Experimental Mechanics*, Sage Pub. December 2003, pp. 428-449
5. Giurgiutiu, V.; Lyshevski, S. E. (2004) *Micro Mechatronics: Modeling, Analysis, and Design with MATLAB*, CRC Press, ISBN 084931593X, 2004
6. Giurgiutiu, V.; Zagrai, A. N.; Bao, J. (2002) "Piezoelectric Wafer Embedded Active Sensors for Aging Aircraft Structural Health Monitoring", *Structural Health Monitoring – An International Journal*, Sage Pub., Vol. 1, No. 1, July 2002, pp. 41-61
7. Giurgiutiu, V; Zagrai, A.N. "Embedded Self-Sensing Piezoelectric Active Sensors for On-Line Structural Identification", Accepted to: *Transactions of ASME, Journal of Vibration and Acoustics*, 2001
8. Grills, R. (2001) "Probability of Detection – An NDT Solution", *The American Society for Nondestructive Testing*, 2001
9. Park, G., etc. "Overview of Piezoelectric Impedance-Based Health Monitoring and Path Forward", *The Shock and Vibration Digest*, Vol. 35, No. 6, November 2003 451-463
10. Raghavan, A.; Cesnik, C. E. S. (2004) "Modeling of Piezoelectric-based Lamb-wave Generation and Sensing for Structural Health Monitoring", SPIE Vol. 5391 (in press)
11. Sonti, V.R., Kim, S.J., and Jones, J.D. (1995) Equivalent forces and wavenumber spectra of shaped piezoelectric actuators. *Journal of Sound and Vibration*, vol. 187, no. 1, pp. 111-131
12. Tseng, K. K, Tinker, M.L., Lassiter, J.O., Peairs, D.M. (2003) "Temperature Dependency of Impedance-Based *Nondestructive Testing*", *Experimental Techniques*, September 33-36, 2003
13. Zagrai, A.; Giurgiutiu, V. (2001) "Electro-Mechanical Impedance Method for Crack Detection in Thin Plates", *Journal of Intelligent Material Systems and Structures*, Vol. 12, No. 10, October 2001, pp. 709-718

9. LIST OF SYMBOLS, ABBREVIATIONS, AND ACRONYMS

1. PWAS – Piezoelectric Wafer Active Sensor
2. EUSR – Embedded Ultrasonic Structural Radar
3. SHM – Structural Health Monitoring
4. NDE – Nondestructive Evaluation
5. POD – Probability of Detection
6. E/M – Electromechanical
7. S_0 – Symmetric Mode
8. A_0 – Antisymmetric Mode
9. NDT – Nondestructive Testing
10. POFM – Probability of false alarm
11. CI – Confidence Interval
12. GUI – graphic user interface

Symbols

$()_{\text{Im}}$ = imaginary part of ()

$()_{\text{Re}}$ = real part of ()

(\sim) = Fourier Transfer of ()

$a = l_a/2$ = half-length of the PWAS

A_1 and B_2 = Arbitrary antisymmetric motion constants

A_2 and B_1 = Arbitrary symmetric motion constants

$a \tau_0$ = the total force transmitted by the PWAS to the structure.

c = chord

c = Wave Speed

$c_p^2 = (\lambda + 2\mu) / \rho$ = pressure (longitudinal)

$c_s^2 = \mu / \rho$ = shear (transverse) wave speeds

d = half thickness

d = Spacing of PWAS Phased Array

D_A = Denominator/Discriminate for Antisymmetric Motion

D_s = Denominator/Discriminate for Symmetric Motion

E = Young's Modulus

$e^{-i\omega t}$ = time-harmonic variation

E_R = signal Energy

f_c = carrier signal of frequency

$G(k(\omega), x) = e^{-ik(\omega) \cdot x}$ = wave transfer function

$H(x)$ = Heaviside step function

$H(x(t)) = -\frac{1}{\pi} \int_{-\infty}^{+\infty} \frac{x(\tau)}{t - \tau} d\tau$ = Hilbert transform

kHz = Kilohertz

$k(\omega)$ = frequency-dependent wave number

L = Arc Length

M = Number of PWAS in a phased array

$N_{A_1}; N_{B_2}; N_A$ = Numerators for Antisymmetric Motion

$N_{A_2}; N_{B_1}; N_S$ = Numerators for Symmetric Motion

$$p^2 = \frac{\omega^2}{c_L^2} - \xi^2$$

$$q^2 = \frac{\omega^2}{c_T^2} - \xi^2 \quad R = \text{radius of curvature}$$

Res @ ξ = Residue at $Z = \xi$

$s_0(t)$ = a short-duration smoothing window applied to f_c between 0 and tp .

s_P = Signal at Point P

s_R = Received Signal

s_T = Transmitted Signal

$s_r(t) = s_0(t) \cos 2\pi f_c t$ = the smoothed tone-burst signal generated by one PWAS $\text{sinc} \alpha = \frac{\sin \alpha}{\alpha}$ = the

Sinc Function

$T = \frac{N_{\text{counts}}}{f_0}$ = tone burst duration $V = V_0 e^{i\omega t}$ = harmonic electric voltage

$\tilde{u}(\omega, x) = p(\omega) \cdot G(\omega, x)$ = frequency domain response

$V e^{-i\omega t}$ = time-harmonic voltage

Y = Yield stress

$y_i = 0.5x_i[1 - \cos(\omega)]$ = Hanning windowed signal

$\Delta_m(\phi)$ = Time of travel difference for m^{th} PWAS Signal

δ_m = time delay of m^{th} PWAS Signal

$\delta(x)$ = Dirac/Delta Function

ϕ = phase array ray angle

ϕ_0 = phase array beam angle

λ = wave length

$\mu\epsilon$ = Microstrain (10^{-6} mm/mm or in/in)

ξ = the wave number

ρ = mass density

σ_u = Ultimate tensile stress

$\tau = \tau_0(x)e^{i\omega t}$ = interfacial shear stress

τ_a = interfacial shear stress between PWAS and structure

$\tau_a(x)e^{-i\omega t}$ = time-harmonic interfacial shear stress

τ_{yx} = Shear Stress in the y and x direction

ω = Angular Frequency